CRISPR/Cas9 Inducible Gene Knockout in Brown Adipose Tissue

by

Steven M. Romanelli

A dissertation submitted in partial fulfillment
of the requirements for the degree of
Doctor of Philosophy
(Molecular and Integrative Physiology)
in the University of Michigan
2021

Doctoral Committee:

Professor Ormond A. MacDougald, Chair
Associate Professor Alan P. Boyle
Professor Charles F. Burant
Associate Professor David P. Olson
Professor Yatrik M. Shah

Steven M. Romanelli

smroma@umich.edu

ORCID iD: 0000-0001-8230-6326

DEDICATION

For my grandfather, Saverio Romanelli, who told me to stay in school.

ACKNOWLEDGMENTS

The pursuit of a Ph.D. cannot be accomplished alone. I am eternally grateful to everyone who has been a part of this long and at times arduous journey. I could not have done it without you.

To Mr. James Markham and Mrs. Linda Charpentier of Xavier High School in Middletown, Connecticut: thank you for making biology engaging. This journey started with you.

To Dr. Ipsita Banerjee of Fordham University: thank you for opening my eyes to the world of research. I would not be here without your mentorship, training, and patience.

To my committee members Dr. Alan Boyle, Dr. Charles Burant, Dr. David Olson, and Dr. Yatrik Shah: thank you for your guidance, time, and insights. It was an honor to learn from each of you.

To Dr. Christopher Church, Dr. Denis Feliers, Dr. Graeme Davies, Dr. Lili Cui, Dr. Arpan Desai, Dr. Simone Romoli, Ms. Kathleen Davy, and the rest of the Cardiovascular, Renal & Metabolism team at AstraZeneca UK: thank you for your endless help and for one of the best summers of my life.

To the Department of Molecular & Integrative Physiology: thank you for embracing me as a student and giving me an opportunity to grow as a scientist. A sincere thank you to Mrs. Michele Boggs for all your hard work behind the scenes.

To my funding support: the Cellular Biotechnology Training Program (T32GM835326), the Ruth L. Kirschenstein National Research Service Award Individual Predoctoral

Fellowship (F31DK122723), the University of Michigan Medical School Endowment for Basic Sciences, and the Rackham Graduate School Student Research Grant(s), for without whom this work would not have been possible.

To The Spicy Boys: thank you for giving me a much-needed outlet from science. I will miss 4th period beers with the boys. Cube Champs forever.

To the MacLab: thank you for your friendship over these last five years. You made lab feel less like work and more like family. While I will miss our GeoGuessr games, I will miss your company most.

To my friends: thank you for your never-ending support. You have been there for me through thick and thin and I am forever grateful to have all of you in my life.

To Dr. Ormond MacDougald: thank you for teaching me what it means to be a scientist, to be critical of your work, to be a leader, and to pursue truth above all else. Your lessons will stick with me forever.

To my brother, Nicholas: thank you for being my best friend. Your passion, wisdom, and determination inspire me every day.

To my parents, Robert, and Lisa: thank you for your unyielding encouragement and for always supporting Nick and me. You have always put our interests above your own and have given us the freedom to chase our dreams.

Lastly, to my grandparents, Saverio, and Santina Romanelli: thank you for sacrificing everything to give your children and grandchildren the opportunities we have today. This degree is a testament to your hard work, resilience, and pursuit of the American Dream.

TABLE OF CONTENTS

DEDICATION ..... **ii**
ACKNOWLEDGMENTS ..... **iii**
LIST OF TABLES ..... **vii**
LIST OF FIGURES ..... **ix**
LIST OF ABBREVIATIONS ..... **xvi**
ABSTRACT ..... **xviii**

CHAPTER I: Introduction **1**

ABSTRACT 1
I. VIRAL AND NONVIRAL GENE TRANSFER TO ADIPOSE TISSUE 1
Introduction to Gene Transfer 1
Targeting Adipose Tissue: Challenges and Limitations 2
Step 1: Selection of an Appropriate Vector 3
Step 2: Optimizing the Route of Administration 7
The “Gold Standard” Approach for Adipose Tissue Gene Transfer 10
II. CRISPR/CAS9: THE FUTURE OF ADIPOSE TISSUE GENE TRANSFER 11
CRISPR/Cas9 Gene Transfer in Adipose Tissue 11
The Future of Adipose Tissue Genome Editing 12
FIGURES AND LEGENDS 14
REFERENCES 18

CHAPTER II: Targeting Adipose Tissue Using Lipid Nanoparticles and Adeno-Associated Viruses **23**

ABSTRACT 23
INTRODUCTION 24
RESULTS 27
DISCUSSION 33
MATERIALS AND METHODS 37
FIGURES AND LEGENDS 40
REFERENCES 49

CHAPTER III: BAd-CRISPR: Inducible Gene Knockout in Brown Adipose Tissue of Adult Mice 54

ABSTRACT 54
INTRODUCTION 55
RESULTS 58
DISCUSSION 67
MATERIALS AND METHODS 71
FIGURES AND LEGENDS 77
REFERENCES 100

CHAPTER IV: Discussion and Future Perspectives 107

What is the mechanism by which BAd-CRISPR Ucp1 inducible knockout mice defend core body temperature? 108
Can BAd-CRISPR be modified to target white and bone marrow adipose tissues? 109
What is the mechanism by which BAd-CRISPR suppresses gene expression? 110
Can BAd-CRISPR be used for more advanced CRISPR applications, such as base editing, CRISPRa, or CRISPRi? 113
Concluding Remarks 115
REFERENCES 116

LIST OF TABLES

CHAPTER I: Introduction

Table 1.1 Viral and nonviral vector properties and affinity for adipose tissue 14

Viral vectors including lentivirus, adenovirus, and AAV can transduce adipose tissues as well as cultured preadipocytes and adipocytes. Of the classes of viruses, AAV has been the most widely used owing to its tropism, expression profile, and low immune response. Nonviral vectors including organic and inorganic nanoparticles have been shown to transfect adipose tissue vasculature and macrophages in addition to cultured preadipocytes. Further research is required to confirm nonviral transfection of adipocytes *in vivo*. dsDNA, double-stranded DNA; ssRNA, single-stranded RNA.

CHAPTER II: Targeting adipose tissue using lipid nanoparticles and adeno-associated viruses

Table 2.1 Physical properties of LNPs 40

A library of LNPs was generated using two microfluidics devices: the NanoAssemblr Benchtop and the Hamilton MicroLab Star. By altering the lipid molarity, PEG molarity, N/P ratio, and mixing rate, we were able to formulate LNPs with different sizes and physical characteristics. * indicates the lead formulation for each microfluidics device.

CHAPTER III: BAd-CRISPR: inducible gene knockout in brown adipose tissue of adult mice

Table 3.1 Sequencing & Genotyping Primers.....77

Table 3.2 qPCR Primers.....79

Table 3.3 Antibodies.....80

LIST OF FIGURES

CHAPTER I: Introduction

Figure 1.1 Viral and nonviral vectors have been used to target adipose tissue 15

Adipose tissue is very heterogeneous, and adipocytes represent a minority of cells in adipose tissue. Thus, a vector must successfully navigate through a variety of cell types to home to the target cell. Viral vectors have been used to transduce adipocytes. Nonviral vectors have been used to transfect adipose tissue vasculature and resident macrophages to elicit physiological changes to the tissue.

Figure 1.2 Adipocyte transduction efficiency is highly dependent upon route of administration.....16

Gene transfer to adipose tissue has proceeded through both systemic and local delivery of viral and nonviral vectors. Systemic delivery via intravenous injection, intraperitoneal injection, or oral gavage accumulates largely in liver and reticuloendothelial organs even when vectors are outfitted with transcriptional control features. By contrast, local delivery via intra-WAT or intra-BAT injection retains the vector at the site of the injection with minimal leak to liver. Arrow size indicates degree of vector distribution.

Figure 1.3 The "gold standard" approach for validation of adipose tissue gene transfer 17

For maximal transduction efficiency and minimal accumulation in off-target tissues, vectors (preferably AAV) should be administered locally through intradepot injection. The most commonly targeted adipose depots are the interscapular BAT, the posterior subcutaneous WAT, and the gonadal WAT. For validation of successful gene transfer, AAV vectors should be outfitted with a reporter such as a fluorescent protein and/or Cre recombinase. Dissected tissues should be imaged or fixed to confirm adipocyte transduction. In this example, mT/mG mice were administered AAV8-Cre via local injection into the posterior subcutaneous WAT. GFP expression is indicative of successful gene transfer and expression of Cre within the adipocytes. Adipose tissue should then be

digest and fractionated to separate adipocytes from stromal vascular cells. The isolated adipocytes and stromal vascular cells can then be analyzed for specificity of transgene expression or cultured for further analyses.

CHAPTER II: Targeting Adipose Tissue Using Lipid Nanoparticles and Adeno-Associated Viruses

Figure 2.1 Microfluidic mixing formulates LNPs with different physical properties 41

(***a***) LNPs were formulated by the rapid mixing of aqueous and lipid phases to create a monodisperse suspension of LNPs encapsulating pDNA. (***b-c***) LNPs diameter and polydispersity index were determined using dynamic light scattering. In total, four formulations were generated using the NanoAssemblr Benchtop (N1, N2, N3, N4) and Hamilton MicroLab Star (H1, H2, H3, H4). Error bars represent standard deviation of diameter and polydispersity index as measured from three technical replicates. Figure is adapted from Cullis et al. (32).

Figure 2.2 LNPs transfect cells *in vitro* and are non-cytotoxic.....42

(***a***) LNP cellular transfection proceeds by endosomal-mediated uptake, destabilization of the endosomal membrane, and release of pDNA. (***b***) Percent encapsulated pDNA in N2-LNPs and H2-LNPs. (***c***) Percent mCherry^{+} B16-F10 cells over 84 hours. (***d***) mCherry count (red calibrated unit [RCU]) after 84 hours for N2-LNPs and H2-LNPs at increasing doses. (***e***) Percent confluence of B16-F10 cells after 84 hours of treatment with LNPs or Lipofectamine 3000; data is normalized to the control. Error bars represent standard deviation, and all experiments were run in triplicate.

Figure 2.3 Systemic delivery of mRNA-LNPs primarily transfects liver but not adipose tissues 44

(***a***) Representative IVIS images of mice 6 hours post injection with PBS, N2-LNPs, or H2-LNPs (0.25 mg/kg) loaded with luciferase mRNA (n = 3). Average radiance taken at 6 hours post injection. Diameter of LNPs as measured by dynamic light scattering. (***b***) Average radiance in BAT, psWAT, eWAT, liver, spleen, kidney, lung, and heart 24 hours after injection. All data are from male mice. Error bars represent standard deviation.

Figure 2.4 pDNA-LNPs localize to adipose tissues and reticuloendothelial organs following systemic delivery.....46

(***a***) IVIS images of mice 48 hours post injection with LNPs (0.25 mg/kg) loaded with luciferase pDNA (n = 3). Average radiance at 48 hours post injection. LNP diameter was determined by dynamic light scattering. (***b***) Average radiance of various tissues taken at 48 hours after injection. All data are from male mice. Error bars represent standard deviation.

Figure 2.5 Route of administration strongly influences AAV8 transduction efficiency of adipose tissues 47

(***a***) Mice administered 100 µL 10^{12} vg/mL AAV8-mCherry by intravenous injection via the tail vein (n = 3). Relative *mCherry* mRNA expression; mRNA normalized to *Ppia*. (***b***) Mice 100 µL 10^{12} vg/mL AAV8-mCherry by intra-BAT injection (n = 3). Relative *mCherry* mRNA expression; mRNA normalized to *Ppia*. (***c***) Mice 100 µL 10^{12} vg/mL AAV8-mCherry by intra-WAT injection (n = 3). Relative *mCherry* mRNA expression; mRNA normalized to *Ppia*. (***d***) Confocal microscopy of freshly dissected BAT, psWAT, eWAT, and liver from mice 14 days post injection; 200x magnification, scale bar, 100 µm (n = 3). Data shown are from male mice. Error bars represent standard deviation.

CHAPTER III: BAd-CRISPR: Inducible Gene Knockout in Brown Adipose Tissue of Adult Mice

Supplement 3.1 sgRNA cloning sequences.....81

(***a***) U6 promoter-driven sgRNA gBlocks template. The template contains the U6 promoter (green), a 20-bp sgRNA without the PAM (red), the sgRNA scaffold (blue), and a termination sequence (orange). The restriction sites for PmlI and KpnI flank the template and are bolded. The entire sequence (414-bp) is used to create a gBlocks Gene Fragment, digested using PmlI and KpnI, and ligated into the AAV expression vector. (***b***) sgRNA sequences, PAM sites, and CFD scores as calculated by the Synthego sgRNA Design Tool.

Figure 3.1 Transfection of adipocyte precursors with sgRNAs predominantly causes frameshift mutations in the target gene.....82

(***a***) U6 promoter-driven sgRNAs were cloned into an AAV expression vector using PmlI and KpnI. The expression vector also contained CMV promoter-driven mCherry and 5’ and 3’ ITRs to facilitate packaging of the cassette into AAV8. (***b-d***) Sanger sequencing traces from Cas9-expressing adipocyte precursors

transfected with AAV8-sgRNAs targeted to *Adipoq*, *Atgl*, and *Plin1*. For each target, primers (purple arrows) were designed upstream and downstream of the sgRNA cut site (yellow arrow). Chromatograms of the reverse strand are shown, and the cut site (black dotted line) and PAM (red underline) are displayed for each sgRNA. The highest frequency indels for each sgRNA and percent contribution as determined by TIDE and the Synthego ICE Analysis tool are shown. Frameshift mutations were calculated by dividing the number of frameshifts over the total number of mutations as estimated by the Synthego ICE Analysis tool.

Supplement 3.2 BAd-CRISPR mice express Cas9 exclusively in BAT 84

(***a***) BAd-CRISPR mice were generated by breeding *Ucp1* promoter-Cre recombinase and Cre-dependent Cas9-GFP mice (Rosa26-LSL-Cas9). (***b***) Immunoblot analyses showing Cas9, UCP1, ADIPOQ, and ERK2 expression with or without Ucp1-Cre. (***c***) Confocal microscopy of freshly dissected BAT, psWAT, pmWAT, and liver from Ucp1-Cre^{-} or Ucp1-Cre^{+} mice; 200x magnification, scale bar, 100 μm (n = 3). Data shown are from female mice.

Supplement 3.3 AAV8 direct injection robustly transduces interscapular BAT 85

(***a***) Confocal micrographs of freshly dissected tissue from Rosa26-Cas9 knockin mice administered 100 μL 10^{12} vg/mL AAV8-mCherry; 200x magnification; scale bar, 100 μm (n = 4). (***b***) *mCherry* mRNA expression; mRNA normalized to PPIA. Data shown are from female mice. Brown adipose tissue (BAT), posterior subcutaneous white adipose tissue (psWAT), parametrial WAT (pmWAT) (n = 4).

Figure 3.2 BAd-CRISPR induces knockout of Adipoq, ATGL, FASN, PLIN1, and SCD1 in brown adipocytes of adult mice 87

(***a-e***) BAT mRNA and protein expression of BAd-CRISPR mice administered 100 μL 10^{12} vg/mL AAV8-sgRNA to *Adipoq*, *Atgl*, *Fasn*, *Plin1*, *Scd1*, or Control; mRNA expression was normalized to *Ppia* (n = 3-4). (***f***) Immunofluorescence analysis of paraffin-sectioned BAT from BAd-CRISPR Atgl mice stained for DAPI and immunolabeled against ATGL; 600x magnification, scale bar, 50 μm. White arrows indicate brown adipocytes that were not mutated. Data shown are from male (*Adipoq*, *Atgl*, *Fasn*, *Plin1*, and Control) and female (*Scd1* and Control) mice. Data are presented as mean ± SD. * indicates significance at $p < 0.05$.

Figure 3.3 BAd-CRISPR Atgl, BAd-CRISPR Plin1, and BAd-CRISPR Fasn inducible knockouts recapitulate previously described BAT phenotypes.....89

(***a***) BAT weight (mg) of BAd-CRISPR mice administered 100 µL 10^{12} vg/mL AAV8-sgRNAs for Control, *Atgl*, *Plin1*, or *Fasn* (n = 3-4). (***b***) H&E staining of BAT; 200x magnification, scale bar, 50 µm. Data shown are from male mice and are presented as mean ± SD. * indicates significance at $p < 0.05$.

Figure 3.4 BAd-CRISPR enables simultaneous knockout of ATGL and PLIN1 in brown adipocytes.....90

(***a***) Freshly dissected BAT from Rosa26-LSL-Cas9 + AAV8-ATGL sgRNA and AAV8-PLIN1 sgRNA (BAd-CRISPR Control), BAd-CRISPR Atgl, BAd-CRISPR Plin1, and BAd-CRISPR Atlg + Plin1 mice administered 100 µL 10^{10} vg/mL of the designated AAV8 (n = 2). (***b***) BAT weight (mg) of Control, BAd-CRISPR Atgl, BAd-CRISPR Plin1, and BAd-CRISPR Atgl + Plin1 mice. (***c***) H&E staining of BAT; 200x magnification, scale bar, 50 µm. Data shown are from male mice. Data are presented as mean ± SD.

Figure 3.5 BAd-CRISPR ablates UCP1 expression in brown adipose tissue 91

(***a***) Confocal micrographs of freshly dissected tissues from BAd-CRISPR Ucp1 mice 14 days after 100 µL 10^{12} vg/mL AAV8-UCP1 sgRNA injection; 200x magnification; scale bar, 50 µm (n = 3). (***b***) *mCherry* mRNA expression at each timepoint, RNA expression normalized to *Ppia* (n = 3 mice per timepoint). (***c***) Genomic Cleavage assay of cDNA isolated from BAT. Red arrows indicate aberrant mutant PCR products. WT band = 320 bp. + or – indicates addition of the T7 endonuclease. (***d***) Sanger sequencing traces of cDNA from 0 or 14 days post injection. The expected cut site is indicated with a dashed line and the PAM is underlined in red. Below, the sgRNA sequence is shown and the PAM is underlined and bolded. The purple arrow indicates the forward primer and sequencing direction. (***e***) mRNA expression of *Ucp1* at each time point, RNA expression normalized to *Ppia* (n = 3 mice per timepoint). (***f***) UCP1 and adiponectin protein expression at 0, 2, 7, or 14 days post AAV8-UCP1 sgRNA injection. Data shown are from female mice and are presented as mean ± SD. * indicates significance at $p < 0.05$.

Supplement 3.4 BAd-CRISPR Ucp1 ablates *Ucp1* expression in adult mice.....93

(***a***) H&E staining of BAT from 0, 2, 7, and 14-days post injection with AAV8-UCP1 sgRNA injection (100 µL 10^{12} vg/mL); 200x magnification; scale bar 50 µm (n = 3 mice per timepoint). (***b-c***) UCP1 expression in Rosa26-LSL-Cas9 or BAd-CRISPR Ucp1 mice administered AAV8-UCP1 sgRNA. (***d-e***) UCP1 expression in BAd-CRISPR Control or BAd-CRISPR Ucp1 mice, mRNA normalized to PPIA. (***f***) Immunofluorescence of BAT from BAd-CRISPR Control or BAd-CRISPR Ucp1 mice immunolabeled against UCP1 and endomucin, nuclei stained with DAPI; 600x magnification, scale bar 100 µm. White arrows indicate brown adipocytes that were not mutated. Data shown are from female mice. Data are presented as mean ± SD. * indicates significance at $p < 0.05$.

Figure 3.6 BAd-CRISPR Ucp1 inducible knockout mice defend core body temperature and have elevated FGF21 95

(***a***) 8-10 week old Rosa26-Cas9 knockin mice were implanted with a telemeter 7-days before injection with 100 µL 10^{12} vg/mL AAV8-Control sgRNA or AAV8-UCP1 sgRNA and single housed at 20-21ºC with no enrichment for 14 days after injection. Mice were cold stressed at 5ºC for 24 hours and then sacrificed. (***b***) *Ucp1* mRNA expression, mRNA normalized to *Ppia* (n = 4 or 5 mice). (***c***) Immunoblot showing UCP1 and Cas9 expression. (***d-e***) Body temperature at 20-21ºC and 5ºC. (***f***) Relative expression of thermogenic markers in BAT, mRNA normalized to *Ppia*. (***g***) Serum FGF21 concentrations in Rosa26-LSL-Cas9 (Control), Ucp1-/-, or BAd-CRISPR Ucp1 mice (n = 3, 4, or 5 mice). Data shown are from female mice. Data are presented as mean ± SD. * indicates significance at $p < 0.05$.

Supplement 3.5 Body temperature, body weight, BAT weight, and food intake are not altered in BAd-CRISPR Ucp1 mice after 24 hour cold stress.....96

(***a***) Body temperature after 24-hours at 5ºC. (***b***) Body weight (g) during 14 day recovery from AAV8 injection to the interscapular BAT. (***c***) Dissected BAT weight (mg). (***d***) Average daily food intake of normal chow diet (g). (***c***) psWAT immunoblot of UCP1 (n = 4-5). Data shown are from female mice.

Figure 3.7 Gene profiling of BAT from BAd-CRISPR Ucp1 mice suggests peroxisomal lipid oxidation and increased protein synthesis/turnover as a compensatory thermogenic process 97

(***a***) Violin plot of *Ucp1* normalized transcript counts per million (CPM) (n = 4 or 5 mice). (***b***) Gene set enrichment analysis (GSEA) of the most up- and down-regulated pathways. (***c***) Heatmap showing the top coordinate regulated expression of genes whose proteins are associated with the peroxisome, lipid metabolism, mitochondrial metabolism, protein translation, and the proteasome. (***d***) Venn diagram depicting overlap of significant differential gene expression of Ucp1-/- and BAd-CRISPR Ucp1 mice taken from GEO entry GSE127251.

Figure 3.8 CRISPR/Cas9 does not lead to observable off-target mutations in BAT of BAd-CRISPR Ucp1 mice 98

(***a***) Off-target sequence mismatches for UCP1 sgRNA predicted by CRISPOR and the Synthego sgRNA Design tool. The UCP1 sgRNA sequence is highlighted in yellow and base mismatches are colored red. Percent mutations were calculated using whole genome sequencing data visualized by the Integrative Genome Viewer (IGV) and CRISPResso2. (***b***) Indel characterization at the intergenic off-target determined by CRISPResso2. (***c***) Genomic cleavage assay at the intergenic off-target. WT band = 140 bp. (***d***) Heatmap of BAT gene expression for each off-target gene locus represented in the RNAseq dataset for BAd-CRISPR Ucp1 mice.

LIST OF ABBREVIATIONS

AAV: adeno-associated virus

ADIPOQ: adiponectin

ATGL: adipose triglyceride lipase

BAd-CRISPR: brown adipocyte-specific CRISPR/Cas9

BAT: brown adipose tissue

Cas9: CRISPR associated protein 9

CFD: cutting frequency determination score

Chol: cholesterol

CRISPR: clustered regularly interspaced short palindromic repeats

CRISPRa: CRISPR activation

CRISPRi: CRISPR inactivation

dCas9: catalytically inactive Cas9

$Đ_M$: polydispersity index

DSPC: distearoylphosphatidylcholine

eWAT: epididymal white adipose tissue

FASN: fatty acid synthase

FGF21: fibroblast growth factor 21

HDR: homology directed repair

LNP: lipid nanoparticle

MC3: DLin-MC3-DMA

NHEJ: non-homologous end joining

pDNA: plasmid DNA

PEG: polyethyleneglycol

PLIN1: perilipin 1

pWAT: parametrial white adipose tissue

psWAT: posterior subcutaneous white adipose tissue

SCD1: stearoyl-CoA desaturase 1

sgRNA: single-guide RNA

UCP1: uncoupling protein 1

WAT: white adipose tissue

ABSTRACT

The ability to study adipose tissue *in vivo* has centered around the use of transgenic mice, which require significant time, resources, and investment to generate. With nearly 40% of adults in the United States considered obese, efficient strategies to improve the way in which adipose tissue is investigated are paramount. Recently, viral or nonviral delivery of CRISPR/Cas9 for inducible gene knockout in somatic tissues has been used to efficiently model disease and study gene function. Its use in adipose tissue, however, has not been attempted owing to an inability to target adipocytes *in vivo*.

My dissertation work sought to identify novel delivery strategies that would enable CRISPR/Cas9 inducible gene knockout in adipose tissue. To accomplish this, I explored the use of adeno-associated viruses (AAVs) and lipid nanoparticles (LNPs) for targeting adipose tissue *in vivo*. I demonstrated that vector and route of administration are the two key factors that govern adipocyte transduction efficiency. Local delivery of AAV serotype 8 was shown to maximize adipocyte transduction specifically in brown adipose tissue (BAT). I thus applied this delivery strategy to attempt CRISPR/Cas9 inducible gene knockout in BAT of adult mice.

I developed the Brown Adipocyte CRISPR (BAd-CRISPR) method, in which AAV8 is used to deliver a single guide RNA (sgRNA) to mice expressing Cas9. I generated a brown adipocyte Cas9-expressing mouse line and developed a cloning pipeline that enabled sgRNAs targeting any gene to be packaged into AAV8 and locally injected to BAT. BAd-CRISPR allowed for rapid interrogation of one or multiple genes and was used to knockout adiponectin (ADIPOQ), adipose triglyceride lipase (ATGL), fatty acid synthase (FASN), perilipin 1 (PLIN1), and stearoyl-CoA desaturase 1 (SCD1) specifically in BAT of adult mice. Importantly, BAd-CRISPR did not result in accumulation of substantial off-target mutations. These studies demonstrated that the BAd-CRISPR

method can be used to inducibly knockout genes in BAT and that transgenic mice can be generated in 1-2 months.

BAd-CRISPR was then used to generate the first inducible uncoupling protein 1 (UCP1) knockout mouse and assess the effects of UCP1 loss on adaptive thermogenesis in adult mice. Inducible UCP1 knockout mice defend core body temperature at 20-21ºC and at 5ºC despite complete loss of UCP1 expression. Interestingly, inducible UCP1 knockout led to an upregulation of genes involved in peroxisomal lipid oxidation and protein synthesis and turnover, and a decrease in genes involved in mitochondrial metabolism, suggesting a compensatory mechanism to maintain adaptive thermogenesis.

Ultimately, my doctoral work produced an efficient method to streamline the paths to discovery in BAT. This work demonstrated that CRISPR/Cas9 can be harnessed to generate BAT specific gene knockout models that require less financial investment and substantially reduced time compared to traditional transgenic approaches. Given the utility of this method, it is expected that with further optimization, BAd-CRISPR will be applicable not only to white and marrow adipose tissues, but also adapted for use in other tissues as well.

CHAPTER I

Introduction

Adapted from:

Romanelli, S.M., and MacDougald, O.A. (2020) Viral and nonviral transfer of genetic materials to adipose tissues: toward a gold standard approach. *Diabetes* **69**, 2581-2588. PMID: 33219099.

ABSTRACT

Gene transfer using viral or nonviral vectors enables the ability to manipulate specific cells and tissues for gene silencing, protein overexpression, or genome modification. Despite the widespread application of viral and nonviral mediated gene transfer to liver, heart, skeletal muscle, and the central nervous system, its use in adipose tissue has been limited. This is largely because adipose tissue is distributed throughout the body in distinct depots and adipocytes make up a minority of the cells within the tissue, making transduction difficult. Currently, there is no consensus methodology for efficient gene transfer to adipose tissue and many studies report conflicting information with regard to transduction efficiency and vector biodistribution. In this review, we summarize the challenges associated with gene transfer to adipose tissue and report on innovations that improve efficacy. We describe how both vector and route of administration are the two key factors that influence transduction efficiency and outline a “gold standard” approach and experimental workflow for validating gene transfer to adipose tissue. Lastly, we speculate on how CRISPR/Cas9 can be integrated to improve adipose tissue research.

I. VIRAL AND NONVIRAL GENE TRANSFER TO ADIPOSE TISSUE

Introduction to Gene Transfer

Our understanding of physiology is heightened by our ability to manipulate cells and tissues. Through gene transfer, we can deliver genetic agents for gene silencing, protein

overexpression, or genome modification to further our understanding of biological phenomena. To accomplish gene transfer in a tissue-specific manner, one must consider two critical components: the vector and the route of administration. An ideal vector shields its cargo from degradation, targets a specific tissue, facilitates unloading of its cargo into cells, and evades the host immune response. Both viral and nonviral vectors meet these criteria (1-3). Secondly, to ensure the vector reaches its desired destination, an appropriate route of administration must be determined. In general, vectors are administered systemically or locally, depending on the tissue of interest. Gene transfer has largely been aimed at the liver, heart, skeletal muscles, and the central nervous system, however, its application to adipose tissue has been met with limited success. Collectively, adipose tissues comprise the largest endocrine organ in the body with important regulatory functions for energy balance and metabolism, thus making it an attractive focal point for understanding obesity and the metabolic syndrome. In this section, we will outline how both vector and route of administration influence transduction efficiency. By carefully optimizing these two factors, gene transfer can be accomplished in an adipose-specific fashion.

Targeting Adipose Tissue: Challenges and Limitations

Adipocytes are located throughout the body mainly in subcutaneous, visceral, and marrow depots as white (WAT), brown (BAT), or more specialized adipose tissues (4-6). At the cellular level, mature adipocytes comprise only 11-40% of the total cell population in adipose tissue, which also contains preadipocytes, stem cells, macrophages, endothelial cells, and vasculature, collectively referred to as stromal vascular cells (7). WAT constitutes the bulk of adipose tissue and is found in subcutaneous and visceral depots. In mice, the subcutaneous WAT includes the interscapular, subscapular, axillary, and cervical depots in the anterior, and the dorso-lumbar, inguinal, and gluteal depots in the posterior. Subcutaneous WATs are also closely associated with lymphatic tissues and in females comprise part of the mammary glands. Visceral adipocytes are contained within the peritoneal cavity and include the mesenteric, perirenal, retroperitoneal, and gonadal (epididymal/ovarian) depots. An inability to expand these depots to store excess energy is typically associated with insulin resistance and metabolic dysfunction (5,6).

Additionally, there are several smaller depots including the intramuscular, periarticular, paracardial, epicardial, retro-orbital, and dermal WAT. By contrast, BAT is predominantly found in the interscapular depot, but also in the periaortic, perirenal, and intercostal depots (8). Brown adipocytes are characterized by a multilocular lipid droplet morphology and are rich in mitochondria (4-6,8). In response to temperatures below thermoneutrality (<~30°C in mice), brown adipocytes express uncoupling protein 1 (UCP1), a key mechanism for adaptive non-shivering thermogenesis (8). Although much smaller in terms of adipose tissue mass, BAT metabolism is the predominant energy consumer in mice at cold temperatures, making it an attractive therapeutic target for treating obesity (8,9).

Given the diversity and distribution of adipose tissue, gene transfer has remained challenging. *In vivo* manipulation has been limited to the generation of Cre-Lox and/or drug-inducible transgenic models. Cre-Lox systems enable the expression of Cre recombinase under the control of adipocyte-specific promoters. Several adipocyte-specific promoters including fatty acid binding protein-4 (aP2) and adiponectin (AdipoQ) have been developed (10). Although both have been used extensively, aP2-Cre activity has been detected in the brain, endothelial cells, macrophages, adipocyte progenitors, and embryonic tissues (11-13). Thus, the field has shifted to conditional (AdipoQ-Cre) or inducible (AdipoQ-Cre^{ERT}, AdipoChaser) lines (13-15). While useful, Cre-mice must be bred to transgenic mice harboring a floxed gene. In some cases, a new floxed line must also be generated, which is time consuming, expensive, and involves large cohorts of animals. Therefore, more efficient strategies, such as gene transfer, would be beneficial to the field.

Step 1: Selection of an Appropriate Vector

Adipose tissue is very heterogenous, and in many cases, vectors transduce stromal vascular cells more efficiently than the adipocytes (7). Thus, a vector must successfully navigate the adipose tissue microenvironment to home to the adipocytes. Important considerations when selecting a vector should include cargo, tropism, expression profile, and immune response (**Table 1.1**). In this section, we will discuss advancements using viral and nonviral vectors for targeting adipocytes.

1.1. Viral Vectors

Different classes of viruses, including lentivirus, adenovirus, and adeno-associated virus (AAV), have all been used for gene transfer to adipose tissue. While lentiviruses and adenoviruses efficiently transduce adipocytes *in vitro*, efforts to mediate gene transfer *in vivo* have been less successful. For example, lentiviruses target CD4+ cells and bind to the HAdV-C receptor, which is not expressed by adipocytes (16,17). Moreover, lentiviruses integrate into the genome leading to insertional mutagenesis (16). While several studies using adenovirus have been performed, concerns of its strong immunologic response and generation of antibodies against its capsid proteins have caused the field to shift to AAV (18-26). AAV is characterized by low immunogenicity, epichromosomal expression, and a multitude of serotypes and capsid variants (27).

Seminal work from the Bosch lab demonstrated that AAV8 and AAV9 preferentially transduce white and brown adipocytes with variable transduction efficiencies across depots (28). Following systemic delivery, AAV8- and AAV9-GFP were highly expressed in the epididymal WAT and interscapular BAT, but marginally expressed in the inguinal, retroperitoneal, and mesenteric depots. Interestingly, variability in GFP expression was observed across different strains of mice including C57/BL/6J, ICR, *ob/ob*, and *db/db*, suggesting genetic background may influence transduction efficiency (28,29). To improve tropism, recombinant AAVs (rAAV) have been engineered by capsid shuffling to increase affinity for adipose tissue. For example, Liu et al. generated rAAVs harboring GFP (Rec2-GFP) and demonstrated increased adipocyte transduction when compared to the natural AAV serotypes 1, 8, and 9 (30). Rec2 vectors were outfitted with Cre-recombinase and injected into the inguinal WAT depots of floxed-insulin receptor mice, which led to ~53% knockout of the insulin receptor and 50% decrease in inguinal WAT mass. Interestingly, these findings are in contrast with AdipoQ-Cre-mediated knockout mice, which develop lipodystrophy and metabolic dysfunction characterized by insulin resistance and hyperglycemia (31). This might be explained by the fact that Rec2-Cre knockout occurs in the adult mouse whereas AdipoQ-Cre causes recombination early in adipocyte development.

1.2. Nonviral Vectors

As an alternative approach, nonviral vectors, including organic and inorganic nanoparticles, have also been explored for gene transfer to adipose tissue. Nonviral nanoscale vectors (<200 nm in diameter) have unique characteristics that make them attractive targets for gene transfer and pharmacologic applications. For example, nonviral vectors can be functionalized with macromolecules to impart tissue specificity (2,3). Efforts to impart adipose specificity have largely focused on conjugating nonviral vectors with the peptide sequence CKGGRAKDC (ATS), which binds to the prohibitin receptor on the subcutaneous WAT vasculature (32). Hossen et al. formulated ATS-conjugated nanoparticles that accumulated in the adipose tissue vasculature of diet-induced obese mice (33). In another study, cadmium-based quantum dots functionalized with ATS targeted the WAT of obese Wistar rats (34). Whilst the mechanism by which ATS-based vectors escape the vasculature to transfect adipocytes remains unknown, research has shown that targeting adipose tissue vasculature directly can influence the surrounding tissue. For example, Xue et al. developed polymer-based nanoparticles conjugated to ATS and loaded with rosiglitazone or prostaglandin E2 analog (35). In treated obese mice, WAT vascular density was increased coupled with the upregulation of the BAT markers *Ucp1*, *Cidea*, and *Dio2*. Thus, modulation of adipose tissues can be achieved by targeting the vasculature.

Modulation of adipose tissue can also be achieved by targeting the resident macrophages to suppress obesity-induced inflammation. In the obese state, endogenous low molecular weight hyaluronic acid binds to CD44-expressing cells to trigger inflammation and insulin resistance (36). Rho et al. developed hyaluronic acid nanoparticles (HA-NPs) to block this pathway and reduce inflammation. HA-NP treated obese mice had significant reductions in body weight, glucose tolerance, and insulin resistance. Additionally, HA-NPs reduced macrophage infiltration and production of inflammatory cytokines in epididymal WAT, likely by outcompeting low molecular weight hyaluronic acid for CD44 binding sites. It should be emphasized, however, that HA-NPs accumulated predominantly in liver, lungs, and kidneys with only marginal transfection observed in the epididymal, subcutaneous, and brown depots. In another study, Ma et al. synthesized dextran-conjugates loaded with dexamethasone to reduce inflammation in

obese mice (37). Impressively, a single dose reduced the expression of TNFα, IL-6, and MCP-1 in the gonadal, perirenal, mesenteric, and subcutaneous depots. Although these studies do not involve gene transfer *per se*, it can be reasoned that genetic cargo can be incorporated into these nonviral vectors. In fact, several nonviral nanoscale vectors have entered clinical trials for the delivery of siRNA to the vasculature (38). Thus, future strategies may involve nonviral-mediated gene transfer to adipocytes, vasculature, or macrophages.

1.3. Insights into Targeted Vector Design

Although both viral and nonviral vectors have been investigated (**Figure 1.1**), there is no consensus method for transducing adipose tissue largely because adipocyte specificity remains a major limitation. Therefore, future success will depend on creating targeted vectors that enhance tissue tropism and impart tissue-specific transcriptional control. To improve tissue tropism, viral envelope glycoproteins have been modified with ligands, peptides, and antibodies. Yang et al. created an efficient method that incorporates antibodies onto the viral surface and enables the virus to bind to a specific cell type and deliver its transgene (39). While this method has not been used to transduce adipocytes directly, one can envision the use of adipocyte-specific antibodies against adipocyte-selective targets such as the amino acid transporter ASC-1 or the brown cell surface markers PAT2 or P2RK5 to improve tropism (40). To impart transcriptional control, adipose-specific promoters such as AdipoQ or UCP1 can limit off-target transgene expression (10,13). It should be noted that the large size of the AdipoQ locus required for adipocyte-specificity restricts its use with AAV, although “mini” promoters such as mini/UCP1, have been implemented (28). Another strategy employs tissue-specific microRNAs targeting posttranscriptional regulatory elements of the transgene. For example, Jimenez et al. incorporated multiple microRNAs to prevent transgene expression in liver and heart but retained transgene expression in WAT and BAT, respectively (28). Thus, targeted vector design that enhances tropism and imparts adipose-selective transcriptional control can significantly improve transduction efficiency and limit off-target expression. A combination of these strategies will likely emerge as the consensus method for gene transfer to adipose tissue. It should be emphasized that

careful consideration should be paid to validating transduction efficiency and selectivity, either by incorporating a fluorescent probe or by separating the adipocytes from stromal vascular cells. We will now turn our attention to the second critical component of delivery: route of administration.

Step 2: Optimizing the Route of Administration

Generally speaking, vector administration can proceed via systemic or local delivery (**Figure 1.2**). Ideally, a vector should transduce every adipocyte across all adipose depots, although this goal has never been fully realized. Therefore, selecting a route should carefully consider the experimental aims, anatomical location, degree of vascularization, and invasiveness in order to optimize transduction efficiency.

2.1. Systemic Delivery via Intravenous Injection

Intravenous injection capitalizes on the circulatory system's direct access to all tissues in the body. Despite this, the varying degree of vascularization in each adipose depot coupled with vector accumulation in reticuloendothelial organs (liver, lung, heart, and kidney) limits adipocyte transduction efficiency (1,2,5,6). Successful gene transfer using intravenous injection via the tail vein has only been accomplished with adenovirus or AAV, however, the field has since shifted exclusively to AAV because of its favorable properties. For example, O'Neill et al. intravenously injected AAV2/8 encoding leptin to leptin-deficient mice (41). A single injection increased plasma leptin levels to 7% of that observed in wild type mice, which led to decreased body weight, food intake, fasting insulin levels, and improved glucose tolerance. In another study, rAAV8 vectors expressing perilipin A were intravenously injected into mice (42). Treated mice showed elevated expression of perilipin A in visceral and subcutaneous WAT and the liver with a decrease in serum free fatty acids. Interestingly, however, both of these studies reported transgene expression in reticuloendothelial organs despite having transcriptional control features, thus highlighting the off-target issues associated with systemic delivery.

2.2. Systemic Delivery via Intraperitoneal Injection

Intraperitoneal injection can be rapidly accomplished in conscious animals with minimal restraint. Vectors injected intraperitoneally are primarily absorbed into the mesenteric vessels that drain into the portal vein and pass through the liver (43). Huang et al. injected mice with Rec2-GFP vectors encoding a liver-specific microRNA to prevent off-target expression (44). Substantial GFP expression was observed in the epididymal WAT but not in other adipose tissues examined nor in reticuloendothelial organs. GFP was exchanged for leptin and injected into leptin-deficient mice, which increased lean mass and circulating leptin levels, improved glucose tolerance, and reversed hepatic steatosis. An important caveat to this study is that vectors transduced only one adipose depot despite being injected via a systemic route.

2.3. Systemic Delivery via Oral Gavage

Enteral delivery through oral gavage is economical, convenient, relatively safe, and requires moderate technical skill (43). In a proof of concept study, Huang et al. examined the effect of oral gavage on the biodistribution of Rec2 vectors (45). Interestingly, Rec2-GFP expression was only detected in the BAT, inguinal WAT, and liver, and not in the stomach, intestine, heart, kidney, or brain. Rec2-Cre vectors were orally administered to floxed-VEGF mice for targeted deletion in BAT. Cold exposure (4°C for 4 hours) led to an inability to defend core body temperature, decreased BAT mass, and VEGF protein depleted by ~80%. VEGF was then overexpressed using orally administered Rec2, which led to an increase in BAT mass and VEGF, UCP1, and CD31 protein levels. The potential mechanism by which Rec2 bypasses the gastro-intestinal system to preferentially transduce BAT has not been described, however, the authors postulate that the lymphatic system may play a role, as Rec2 was detected in the mesenteric adipose depot, which is rich in lymph nodes.

2.4. Local Delivery via Intra-Depot Injection

In contrast to systemic delivery, local delivery is a more targeted approach in which vectors are administered directly into a tissue. Although slightly more invasive, time consuming, and resource heavy, local delivery via intra-depot injection retains vectors at the site of injection, enabling the study of depot-specific function (27,43,46). For adipose

tissue, intra-depot injection has proceeded through intra-WAT or intra-BAT injection of viral and nonviral vectors. Before attempting intra-depot injection, we recommend reviewing references (4-6,27,46) for guidance on how to access these tissues.

2.5. Local Delivery via Intra-WAT Injection

Mizukami et al. was the first group to optimize intra-WAT injection by administering AAV1-erythropoietin into the subcutaneous WAT (47). Treated mice showed elevated plasma erythropoietin concentration compared to controls. The transduced subcutaneous WAT was then surgically removed, causing plasma erythropoietin concentrations to return to baseline, indicating that increased circulating erythropoietin was the result of gene transfer to WAT specifically. Work from the Bosch lab explored AAV-mediated gene transfer to overexpress fibroblast growth factor 21 as a therapeutic strategy for treating obesity (48). AAV8 that expressed fibroblast growth factor 21 was administered directly into liver, epididymal WAT, or skeletal muscle of obese mice. Interestingly, a single injection into the epididymal WAT led to a dose dependent reduction in adipocyte size, improvement in insulin sensitivity, and prevention of hepatic steatosis, which was comparable to both liver- and skeletal muscle-specific injections. Collectively, these studies demonstrate that a single dose of AAV to one adipose depot is sufficient to mediate systemic changes to metabolism.

Lentiviruses have also been used for intra-WAT gene transfer applications. Gnad et al. injected a lentivirus expressing the A_{2A} receptor into the inguinal WAT of obese mice as an anti-obesity therapy (49). Stimulation of sympathetic drive causes BAT to release adenosine, which binds to the A_{2A} receptor to increase energy expenditure. It was hypothesized that overexpression of the A_{2A} receptor in inguinal WAT, which has the capacity for browning, might have therapeutic potential. Interestingly, lentiviral expression of the A_{2A} receptor significantly increased thermogenic and lipogenic markers and led to a brown adipocyte-like morphology in the inguinal WAT with increased expression of *Ucp1*, *Pgc1α*, and *Prdm16*.

Only one study has attempted intra-WAT injection of a nonviral vector for gene transfer. The Kim lab synthesized an ATS-oligopeptide complex to administer shRNA to silence fatty acid binding protein-4 (FABP4) and combat obesity (50). Obese mice were

administered the complex via intra-WAT injection on one side of the “abdominal” adipose tissue. Strikingly, FABP4 expression was decreased by 70% when compared to the contralateral depot. Treated mice also showed significant improvements in insulin sensitivity and reduced blood glucose levels. Perhaps the most surprising data are that treated mice lost nearly 20% of their body weight following a single administration to one WAT depot. While these data are interesting, they also raise several red flags. Firstly, the mechanism by which the ATS-oligopeptide-shRNA complex binds to prohibitin on adipose tissue vasculature and escapes to transduce the adipocytes has not been explained. Secondly, the authors do not report changes in energy balance, lipolysis, inflammation, apoptosis, cell death, nor changes in tissue mass in the injected WAT depot, leading us to question how silencing FABP4 in one adipose tissue equates to a 20% reduction in body weight. This study is also in direct contradiction with previous work that shows FABP4 knockdown or knockout in obese mice increases body weight and fat mass without changes in glucose homeostasis (51,52). Moreover, it does not report on FABP5 expression, which is compensatory to loss of FABP4 (53).

2.6. Local Delivery via Intra-BAT Injection

Similar to intra-WAT injection, AAV has remained the most commonly used vector for intra-BAT injection. Two aforementioned studies attempted intra-BAT injection using AAVs. Jimenez et al. showed that intra-BAT injection of AAV9 encoding VEGF164 under the control of the mini/UCP1 promoter increased vessel density and VEGF164 expression specifically in BAT (28). In the second study, Liu et al. administered Rec2-Cre bilaterally into the BAT of floxed-insulin receptor mice which decreased BAT size by 50% and expression of insulin receptor protein by ~60% (30). Surprisingly, disruption of insulin receptor signaling in BAT induced gene expression changes in the hypothalamus, highlighting that depot-specific gene transfer can be used to study the interaction between adipose tissue and the central nervous system.

The “Gold Standard” Approach for Adipose Tissue Gene Transfer

Although significant progress has been made using viral and nonviral vectors, the field lacks a gold standard approach. Experimental aims will always dictate the selection of a

vector and route of administration; however, to guide the reader we propose the following set of guidelines:

1. Transcriptionally controlled AAVs currently show the most promise for transducing adipocytes in adipose tissues. Researchers should prioritize rAAV, AAV8, or AAV9 that incorporates an adipose-specific promoter-driven transgene (mini/AdipoQ or mini/UCP1), a microRNA to limit transgene expression in off-target tissues, and a reporter molecule to validate transduction efficiency.

2. To maximize adipocyte transduction efficiency and limit accumulation in off-target tissues, vectors should be administered locally via intra-WAT or intra-BAT injection.

3. To validate your experiment, follow the gold standard approach outlined in **Figure 1.3**. For validating adipocyte transduction, vectors should be outfitted with fluorescent probes or administered to reporter lines such as the mT/mG mouse (54). Successful transduction is characterized by a fluorescent "halo" surrounding the adipocyte. As adipocytes represent only a small fraction of the total cells in adipose tissue, they should be separated from stromal vascular cells by buoyant-density centrifugation, and both fractions analyzed for transduction.

While we have focused on transducing adipocytes, it should be noted that targeting the vasculature or resident macrophages is an alternative strategy for manipulating adipose tissues. This is particularly true for nonviral vectors, although continued research is required.

II. CRISPR/CAS9: THE FUTURE OF ADIPOSE TISSUE GENE TRANSFER

CRISPR/Cas9 Gene Transfer in Adipose Tissue

With the emergence of powerful gene editing technologies like CRISPR/Cas9, researchers can modify virtually any region of the genome. CRISPR/Cas9 is composed

of two components: the Cas9 endonuclease, and a programmable single guide RNA (sgRNA) that directs Cas9 where to create double-strand breaks in genomic DNA (55). CRISPR/Cas9 is thus easily amendable to viral or nonviral gene transfer as its constitutive parts can be genetically encoded. Despite the adoption of CRISPR/Cas9 gene transfer to a variety of tissues (56-59), only one study reports its use in adipose tissue (60). We recommend caution, however, as this study uses the ATS-oligopeptide complex described above for CRISPR-interference silencing of FABP4 (50,60).

Two studies have recently reported on *in vitro* delivery of CRISPR/Cas9 to cultured adipocyte precursors. The Czech lab successfully transfected isolated primary preadipocytes with nonviral vectors loaded with Cas9 protein and a sgRNA targeted to *Nrip1* (61). Treated cells showed a mutation frequency of 43.8% in the *Nrip1* locus coupled with increased expression of the brown-like genes *Ucp1*, *Cidea*, *Pgc1α*, *Prdm16*, and *Cpt1b*. Importantly, no off-target mutations were detected and CRISPR/Cas9 did not affect the capacity to differentiate. In a second study, Kamble et al. electroporated human preadipocytes with a ribonucleoprotein complex of Cas9 and a sgRNA targeted to *Pparg* or *Fkbp5* (62). Impressively, treated cells achieved 90% efficiency and did not require selection or clonal isolation of edited cells. While these studies demonstrate *in vitro* proof of principle, the field has yet to report successful *in vivo* gene transfer of CRISPR/Cas9 to adipose tissue.

The Future of Adipose Tissue Genome Editing

CRISPR/Cas9 gene transfer to adipose tissue is in its infancy, however, we can gain several insights from its use in other tissues and apply these to the gold standard approach. For example, CRISPR/Cas9 gene transfer can proceed via exogenous expression or a combination of exogenous/endogenous expression of its components. In the exogenous method, both Cas9 and sgRNA are delivered via a vector. In the exogenous/endogenous method, the sgRNA is delivered to a Cas9-expressing mouse line (63,64). Thus, rAAVs can be encoded with one or multiple sgRNAs and administered locally to AdipoQ-Cre dependent Cas9 mice to enable spatial control (63). Cas9 expression can also be temporally regulated using a doxycycline-inducible line developed by Dow and Fisher (64). Ultimately, CRISPR/Cas9 has immense potential for elucidating

the underlying mechanisms to a myriad of metabolic diseases. For instance, future application of CRISPR/Cas9 might entail homology-directed repair to correct single nucleotide polymorphisms associated with aberrant metabolism (65). Particular focus should be paid to integrating CRISPR/Cas9 with well-established gene transfer techniques such as AAV and Cre-Lox mouse models (63,64). Moreover, we also recommend a strong adherence to the gold standard approach to validate transduction efficiency. With these powerful technologies in hand, the field of adipose tissue biology is poised to enter a new era of research.

Indeed, selectively targeting adipocytes for CRISPR/Cas9 somatic mutagenesis can significantly improve the way in which we study adipose tissues *in vivo*. However, current delivery strategies must first be optimized and validated before such technologies can be applied. Thus, my doctoral work described in the following chapters will provide a framework by which viral and nonviral vectors were tested for adipocyte specificity *in vivo* and then applied to enable CRISPR/Cas9 inducible knockout in BAT. As such, I developed an efficient methodology to significantly improve the way in which we study BAT that can benefit the field of adipose tissue biology and beyond.

TABLE 1.1

Table 1—Viral and nonviral vector properties and affinity for adipose tissue

Vector	Cargo	Genome size (kb)	Affinity for adipose tissue	Expression profile	Immune response	Genome integration	References
Lentivirus	ssRNA	9.7	Adipocytes, stromal vascular cells, cultured preadipocytes and adipocytes	Stable (permanent)	Low	Yes	16,17,49
Adenovirus	dsDNA	26–46		Transient (weeks)	High	No	18–26
AAV	ssDNA	4.7		Transient (months to years)	Very low	Rare	27–30,41,42,44–48
Nonviral	DNA, mRNA, shRNA, protein	Not restricted	Stromal vascular cells, cultured preadipocytes	Transient (hours to days)	Low to moderate	No	32–37,50,60–62

Table 1.1. Viral and nonviral vector properties and affinity for adipose tissue. Viral vectors including lentivirus, adenovirus, and AAV can transduce adipose tissues as well as cultured preadipocytes and adipocytes. Of the classes of viruses, AAV has been the most widely used owing to its tropism, expression profile, and low immune response. Nonviral vectors including organic and inorganic nanoparticles have been shown to transfect adipose tissue vasculature and macrophages in addition to cultured preadipocytes. Further research is required to confirm nonviral transfection of adipocytes *in vivo*. dsDNA, double-stranded DNA; ssRNA, single-stranded RNA.

FIGURE 1.1

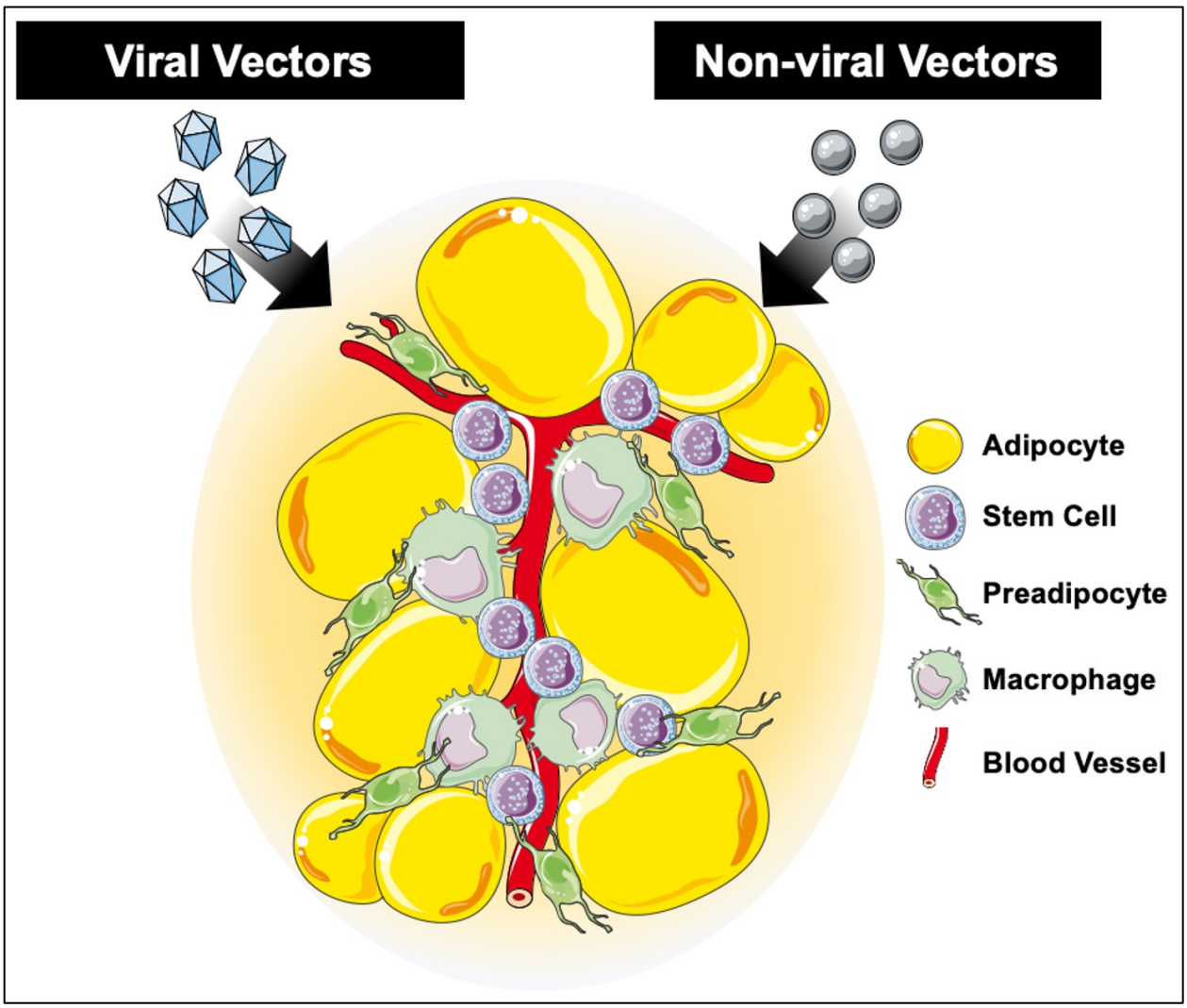

Figure 1.1. Viral and nonviral vectors have been used to target adipose tissue. Adipose tissue is very heterogeneous, and adipocytes represent a minority of cells in adipose tissue. Thus, a vector must successfully navigate through a variety of cell types to home to the target cell. Viral vectors have been used to transduce adipocytes. Nonviral vectors have been used to transfect adipose tissue vasculature and resident macrophages to elicit physiological changes to the tissue.

FIGURE 1.2

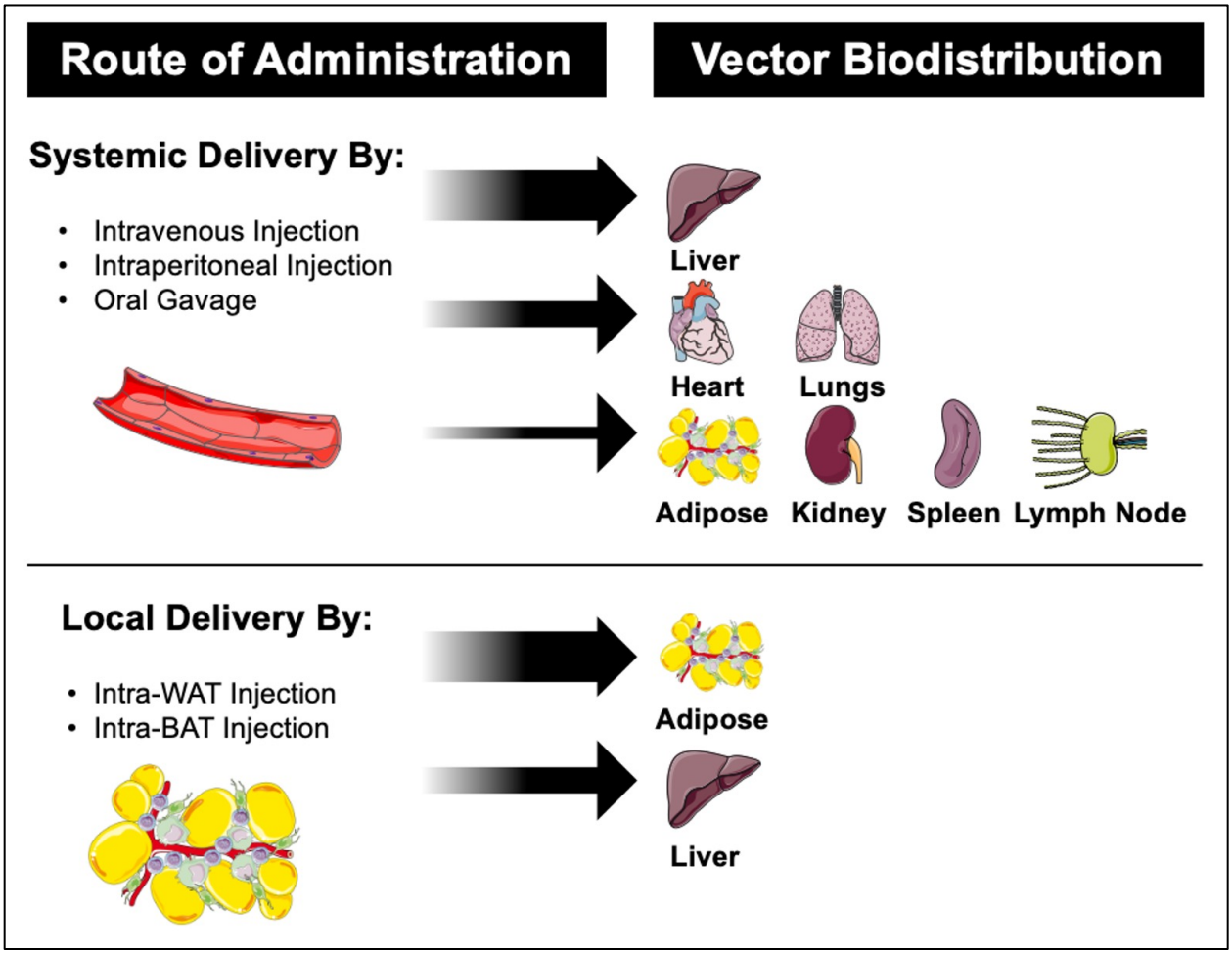

Figure 1.2. Adipocyte transduction efficiency is highly dependent upon route of administration. Gene transfer to adipose tissue has proceeded through both systemic and local delivery of viral and nonviral vectors. Systemic delivery via intravenous injection, intraperitoneal injection, or oral gavage accumulates largely in liver and reticuloendothelial organs even when vectors are outfitted with transcriptional control features. By contrast, local delivery via intra-WAT or intra-BAT injection retains the vector at the site of the injection with minimal leak to liver. Arrow size indicates degree of vector distribution.

FIGURE 1.3

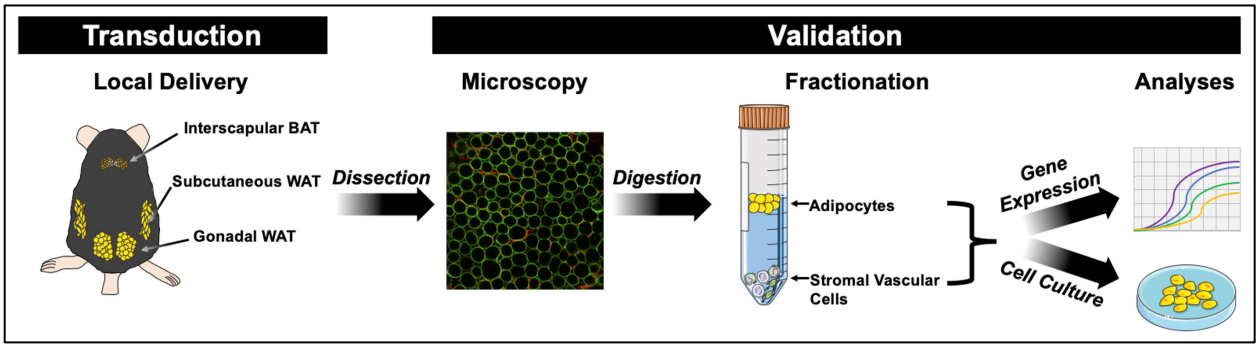

Figure 1.3. The "gold standard" approach for validation of adipose tissue gene transfer. For maximal transduction efficiency and minimal accumulation in off-target tissues, vectors (preferably AAV) should be administered locally through intradepot injection. The most commonly targeted adipose depots are the interscapular BAT, the posterior subcutaneous WAT, and the gonadal WAT. For validation of successful gene transfer, AAV vectors should be outfitted with a reporter such as a fluorescent protein and/or Cre recombinase. Dissected tissues should be imaged or fixed to confirm adipocyte transduction. In this example, mT/mG mice were administered AAV8-Cre via local injection into the posterior subcutaneous WAT. GFP expression is indicative of successful gene transfer and expression of Cre within the adipocytes. Adipose tissue should then be digest and fractionated to separate adipocytes from stromal vascular cells. The isolated adipocytes and stromal vascular cells can then be analyzed for specificity of transgene expression or cultured for further analyses.

REFERENCES

1. Mingozzi, F., and High, K. A. (2011) Therapeutic in vivo gene transfer for genetic disease using AAV: progress and challenges. *Nat Rev Genet* **12**, 341-355
2. Nayerossadat, N., Maedeh, T., and Ali, P. A. (2012) Viral and nonviral delivery systems for gene delivery. *Adv Biomed Res* **1**, 27
3. Yang, N. (2015) An overview of viral and nonviral delivery systems for microRNA. *Int J Pharm Investig* **5**, 179-181
4. Bagchi, D. P., Forss, I., Mandrup, S., and MacDougald, O. A. (2018) SnapShot: Niche Determines Adipocyte Character I. *Cell Metab* **27**, 264-264 e261
5. Bagchi, D. P., Forss, I., Mandrup, S., and MacDougald, O. A. (2018) SnapShot: Niche Determines Adipocyte Character II. *Cell Metab* **27**, 266-266 e261
6. Bagchi, D. P., and MacDougald, O. A. (2019) Identification and Dissection of Diverse Mouse Adipose Depots. *J Vis Exp*
7. Parlee, S. D., Lentz, S. I., Mori, H., and MacDougald, O. A. (2014) Quantifying size and number of adipocytes in adipose tissue. *Methods Enzymol* **537**, 93-122
8. Cannon, B., and Nedergaard, J. (2004) Brown adipose tissue: function and physiological significance. *Physiol Rev* **84**, 277-359
9. Chechi, K., Carpentier, A. C., and Richard, D. (2013) Understanding the brown adipocyte as a contributor to energy homeostasis. *Trends Endocrinol Metab* **24**, 408-420
10. Jeffery, E., Berry, R., Church, C. D., Yu, S., Shook, B. A., Horsley, V., Rosen, E. D., and Rodeheffer, M. S. (2014) Characterization of Cre recombinase models for the study of adipose tissue. *Adipocyte* **3**, 206-211
11. Mullican, S. E., Tomaru, T., Gaddis, C. A., Peed, L. C., Sundaram, A., and Lazar, M. A. (2013) A novel adipose-specific gene deletion model demonstrates potential pitfalls of existing methods. *Mol Endocrinol* **27**, 127-134
12. Urs, S., Harrington, A., Liaw, L., and Small, D. (2006) Selective expression of an aP2/Fatty Acid Binding Protein 4-Cre transgene in non-adipogenic tissues during embryonic development. *Transgenic Res* **15**, 647-653
13. Lee, K. Y., Russell, S. J., Ussar, S., Boucher, J., Vernochet, C., Mori, M. A., Smyth, G., Rourk, M., Cederquist, C., Rosen, E. D., Kahn, B. B., and Kahn, C. R. (2013) Lessons on conditional gene targeting in mouse adipose tissue. *Diabetes* **62**, 864-874
14. Eguchi, J., Wang, X., Yu, S., Kershaw, E. E., Chiu, P. C., Dushay, J., Estall, J. L., Klein, U., Maratos-Flier, E., and Rosen, E. D. (2011) Transcriptional control of adipose lipid handling by IRF4. *Cell Metab* **13**, 249-259
15. Wang, Q. A., and Scherer, P. E. (2014) The AdipoChaser mouse: A model tracking adipogenesis in vivo. *Adipocyte* **3**, 146-150
16. Quinonez, R., and Sutton, R. E. (2002) Lentiviral vectors for gene delivery into cells. *DNA Cell Biol* **21**, 937-951
17. Kobinger, G. P., Weiner, D. J., Yu, Q. C., and Wilson, J. M. (2001) Filovirus-pseudotyped lentiviral vector can efficiently and stably transduce airway epithelia in vivo. *Nat Biotechnol* **19**, 225-230
18. Wold, W. S., and Toth, K. (2013) Adenovirus vectors for gene therapy, vaccination and cancer gene therapy. *Curr Gene Ther* **13**, 421-433

19. Yang, Y., Nunes, F. A., Berencsi, K., Furth, E. E., Gonczol, E., and Wilson, J. M. (1994) Cellular immunity to viral antigens limits E1-deleted adenoviruses for gene therapy. *Proc Natl Acad Sci U S A* **91**, 4407-4411
20. Yang, Y., Ertl, H. C., and Wilson, J. M. (1994) MHC class I-restricted cytotoxic T lymphocytes to viral antigens destroy hepatocytes in mice infected with E1-deleted recombinant adenoviruses. *Immunity* **1**, 433-442
21. Muzzin, P., Eisensmith, R. C., Copeland, K. C., and Woo, S. L. (1996) Correction of obesity and diabetes in genetically obese mice by leptin gene therapy. *Proc Natl Acad Sci U S A* **93**, 14804-14808
22. Lee, S., Zhang, H., Chen, J., Dellsperger, K. C., Hill, M. A., and Zhang, C. (2012) Adiponectin abates diabetes-induced endothelial dysfunction by suppressing oxidative stress, adhesion molecules, and inflammation in type 2 diabetic mice. *Am J Physiol Heart Circ Physiol* **303**, H106-115
23. Lo, J. C., Ljubicic, S., Leibiger, B., Kern, M., Leibiger, I. B., Moede, T., Kelly, M. E., Chatterjee Bhowmick, D., Murano, I., Cohen, P., Banks, A. S., Khandekar, M. J., Dietrich, A., Flier, J. S., Cinti, S., Bluher, M., Danial, N. N., Berggren, P. O., and Spiegelman, B. M. (2014) Adipsin is an adipokine that improves beta cell function in diabetes. *Cell* **158**, 41-53
24. Bostrom, P., Wu, J., Jedrychowski, M. P., Korde, A., Ye, L., Lo, J. C., Rasbach, K. A., Bostrom, E. A., Choi, J. H., Long, J. Z., Kajimura, S., Zingaretti, M. C., Vind, B. F., Tu, H., Cinti, S., Hojlund, K., Gygi, S. P., and Spiegelman, B. M. (2012) A PGC1-alpha-dependent myokine that drives brown-fat-like development of white fat and thermogenesis. *Nature* **481**, 463-468
25. Rao, R. R., Long, J. Z., White, J. P., Svensson, K. J., Lou, J., Lokurkar, I., Jedrychowski, M. P., Ruas, J. L., Wrann, C. D., Lo, J. C., Camera, D. M., Lachey, J., Gygi, S., Seehra, J., Hawley, J. A., and Spiegelman, B. M. (2014) Meteorin-like is a hormone that regulates immune-adipose interactions to increase beige fat thermogenesis. *Cell* **157**, 1279-1291
26. Svensson, K. J., Long, J. Z., Jedrychowski, M. P., Cohen, P., Lo, J. C., Serag, S., Kir, S., Shinoda, K., Tartaglia, J. A., Rao, R. R., Chedotal, A., Kajimura, S., Gygi, S. P., and Spiegelman, B. M. (2016) A Secreted Slit2 Fragment Regulates Adipose Tissue Thermogenesis and Metabolic Function. *Cell Metab* **23**, 454-466
27. Huang, W., Queen, N. J., and Cao, L. (2019) rAAV-Mediated Gene Delivery to Adipose Tissue. *Methods Mol Biol* **1950**, 389-405
28. Jimenez, V., Munoz, S., Casana, E., Mallol, C., Elias, I., Jambrina, C., Ribera, A., Ferre, T., Franckhauser, S., and Bosch, F. (2013) In vivo adeno-associated viral vector-mediated genetic engineering of white and brown adipose tissue in adult mice. *Diabetes* **62**, 4012-4022
29. Zincarelli, C., Soltys, S., Rengo, G., and Rabinowitz, J. E. (2008) Analysis of AAV serotypes 1-9 mediated gene expression and tropism in mice after systemic injection. *Mol Ther* **16**, 1073-1080
30. Liu, X., Magee, D., Wang, C., McMurphy, T., Slater, A., During, M., and Cao, L. (2014) Adipose tissue insulin receptor knockdown via a new primate-derived hybrid recombinant AAV serotype. *Mol Ther Methods Clin Dev* **1**
31. Qiang, G., Whang Kong, H., Xu, S., Pham, H. A., Parlee, S. D., Burr, A. A., Gil, V., Pang, J., Hughes, A., Gu, X., Fantuzzi, G., MacDougald, O. A., and Liew, C. W.

(2016) Lipodystrophy and severe metabolic dysfunction in mice with adipose tissue-specific insulin receptor ablation. *Mol Metab* **5**, 480-490
32. Kolonin, M. G., Saha, P. K., Chan, L., Pasqualini, R., and Arap, W. (2004) Reversal of obesity by targeted ablation of adipose tissue. *Nat Med* **10**, 625-632
33. Hossen, M. N., Kajimoto, K., Akita, H., Hyodo, M., and Harashima, H. (2012) Vascular-targeted nanotherapy for obesity: unexpected passive targeting mechanism to obese fat for the enhancement of active drug delivery. *J Control Release* **163**, 101-110
34. Thovhogi, N., Sibuyi, N. R. S., Onani, M. O., Meyer, M., and Madiehe, A. M. (2018) Peptide-functionalized quantum dots for potential applications in the imaging and treatment of obesity. *Int J Nanomedicine* **13**, 2551-2559
35. Xue, Y., Xu, X., Zhang, X. Q., Farokhzad, O. C., and Langer, R. (2016) Preventing diet-induced obesity in mice by adipose tissue transformation and angiogenesis using targeted nanoparticles. *Proc Natl Acad Sci U S A* **113**, 5552-5557
36. Rho, J. G., Han, H. S., Han, J. H., Lee, H., Nguyen, V. Q., Lee, W. H., Kwon, S., Heo, S., Yoon, J., Shin, H. H., Lee, E. Y., Kang, H., Yang, S., Lee, E. K., Park, J. H., and Kim, W. (2018) Self-assembled hyaluronic acid nanoparticles: Implications as a nanomedicine for treatment of type 2 diabetes. *J Control Release* **279**, 89-98
37. Ma, L., Liu, T. W., Wallig, M. A., Dobrucki, I. T., Dobrucki, L. W., Nelson, E. R., Swanson, K. S., and Smith, A. M. (2016) Efficient Targeting of Adipose Tissue Macrophages in Obesity with Polysaccharide Nanocarriers. *ACS Nano* **10**, 6952-6962
38. Cullis, P. R., and Hope, M. J. (2017) Lipid Nanoparticle Systems for Enabling Gene Therapies. *Mol Ther* **25**, 1467-1475
39. Yang, L., Bailey, L., Baltimore, D., and Wang, P. (2006) Targeting lentiviral vectors to specific cell types in vivo. *Proc Natl Acad Sci U S A* **103**, 11479-11484
40. Ussar, S., Lee, K. Y., Dankel, S. N., Boucher, J., Haering, M. F., Kleinridders, A., Thomou, T., Xue, R., Macotela, Y., Cypess, A. M., Tseng, Y. H., Mellgren, G., and Kahn, C. R. (2014) ASC-1, PAT2, and P2RX5 are cell surface markers for white, beige, and brown adipocytes. *Sci Transl Med* **6**, 247ra103
41. O'Neill, S. M., Hinkle, C., Chen, S. J., Sandhu, A., Hovhannisyan, R., Stephan, S., Lagor, W. R., Ahima, R. S., Johnston, J. C., and Reilly, M. P. (2014) Targeting adipose tissue via systemic gene therapy. *Gene Ther* **21**, 653-661
42. Uhrig-Schmidt, S., Geiger, M., Luippold, G., Birk, G., Mennerich, D., Neubauer, H., Grimm, D., Wolfrum, C., and Kreuz, S. (2014) Gene delivery to adipose tissue using transcriptionally targeted rAAV8 vectors. *PLoS One* **9**, e116288
43. Turner, P. V., Brabb, T., Pekow, C., and Vasbinder, M. A. (2011) Administration of substances to laboratory animals: routes of administration and factors to consider. *J Am Assoc Lab Anim Sci* **50**, 600-613
44. Huang, W., Liu, X., Queen, N. J., and Cao, L. (2017) Targeting Visceral Fat by Intraperitoneal Delivery of Novel AAV Serotype Vector Restricting Off-Target Transduction in Liver. *Mol Ther Methods Clin Dev* **6**, 68-78
45. Huang, W., McMurphy, T., Liu, X., Wang, C., and Cao, L. (2016) Genetic Manipulation of Brown Fat Via Oral Administration of an Engineered Recombinant Adeno-associated Viral Serotype Vector. *Mol Ther* **24**, 1062-1069

46. Gomez-Banoy, N., and Lo, J. C. (2017) Genetic Manipulation with Viral Vectors to Assess Metabolism and Adipose Tissue Function. *Methods Mol Biol* **1566**, 109-124
47. Mizukami, H., Mimuro, J., Ogura, T., Okada, T., Urabe, M., Kume, A., Sakata, Y., and Ozawa, K. (2006) Adipose tissue as a novel target for in vivo gene transfer by adeno-associated viral vectors. *Hum Gene Ther* **17**, 921-928
48. Jimenez, V., Jambrina, C., Casana, E., Sacristan, V., Munoz, S., Darriba, S., Rodo, J., Mallol, C., Garcia, M., Leon, X., Marco, S., Ribera, A., Elias, I., Casellas, A., Grass, I., Elias, G., Ferre, T., Motas, S., Franckhauser, S., Mulero, F., Navarro, M., Haurigot, V., Ruberte, J., and Bosch, F. (2018) FGF21 gene therapy as treatment for obesity and insulin resistance. *EMBO Mol Med* **10**
49. Gnad, T., Scheibler, S., von Kugelgen, I., Scheele, C., Kilic, A., Glode, A., Hoffmann, L. S., Reverte-Salisa, L., Horn, P., Mutlu, S., El-Tayeb, A., Kranz, M., Deuther-Conrad, W., Brust, P., Lidell, M. E., Betz, M. J., Enerback, S., Schrader, J., Yegutkin, G. G., Muller, C. E., and Pfeifer, A. (2014) Adenosine activates brown adipose tissue and recruits beige adipocytes via A2A receptors. *Nature* **516**, 395-399
50. Won, Y. W., Adhikary, P. P., Lim, K. S., Kim, H. J., Kim, J. K., and Kim, Y. H. (2014) Oligopeptide complex for targeted non-viral gene delivery to adipocytes. *Nat Mater* **13**, 1157-1164
51. Yang, R., Castriota, G., Chen, Y., Cleary, M. A., Ellsworth, K., Shin, M. K., Tran, J. L., Vogt, T. F., Wu, M., Xu, S., Yang, X., Zhang, B. B., Berger, J. P., and Qureshi, S. A. (2011) RNAi-mediated germline knockdown of FABP4 increases body weight but does not improve the deranged nutrient metabolism of diet-induced obese mice. *Int J Obes (Lond)* **35**, 217-225
52. Coe, N. R., Simpson, M. A., and Bernlohr, D. A. (1999) Targeted disruption of the adipocyte lipid-binding protein (aP2 protein) gene impairs fat cell lipolysis and increases cellular fatty acid levels. *J Lipid Res* **40**, 967-972
53. Hotamisligil, G. S., Johnson, R. S., Distel, R. J., Ellis, R., Papaioannou, V. E., and Spiegelman, B. M. (1996) Uncoupling of obesity from insulin resistance through a targeted mutation in aP2, the adipocyte fatty acid binding protein. *Science* **274**, 1377-1379
54. Muzumdar, M. D., Tasic, B., Miyamichi, K., Li, L., and Luo, L. (2007) A global double-fluorescent Cre reporter mouse. *Genesis* **45**, 593-605
55. Doudna, J. A., and Charpentier, E. (2014) Genome editing. The new frontier of genome engineering with CRISPR-Cas9. *Science* **346**, 1258096
56. Swiech, L., Heidenreich, M., Banerjee, A., Habib, N., Li, Y., Trombetta, J., Sur, M., and Zhang, F. (2015) In vivo interrogation of gene function in the mammalian brain using CRISPR-Cas9. *Nat Biotechnol* **33**, 102-106
57. Yin, H., Song, C. Q., Dorkin, J. R., Zhu, L. J., Li, Y., Wu, Q., Park, A., Yang, J., Suresh, S., Bizhanova, A., Gupta, A., Bolukbasi, M. F., Walsh, S., Bogorad, R. L., Gao, G., Weng, Z., Dong, Y., Koteliansky, V., Wolfe, S. A., Langer, R., Xue, W., and Anderson, D. G. (2016) Therapeutic genome editing by combined viral and non-viral delivery of CRISPR system components in vivo. *Nat Biotechnol* **34**, 328-333

58. Guo, Y., VanDusen, N. J., Zhang, L., Gu, W., Sethi, I., Guatimosim, S., Ma, Q., Jardin, B. D., Ai, Y., Zhang, D., Chen, B., Guo, A., Yuan, G. C., Song, L. S., and Pu, W. T. (2017) Analysis of Cardiac Myocyte Maturation Using CASAAV, a Platform for Rapid Dissection of Cardiac Myocyte Gene Function In Vivo. *Circ Res* **120**, 1874-1888
59. Finn, J. D., Smith, A. R., Patel, M. C., Shaw, L., Youniss, M. R., van Heteren, J., Dirstine, T., Ciullo, C., Lescarbeau, R., Seitzer, J., Shah, R. R., Shah, A., Ling, D., Growe, J., Pink, M., Rohde, E., Wood, K. M., Salomon, W. E., Harrington, W. F., Dombrowski, C., Strapps, W. R., Chang, Y., and Morrissey, D. V. (2018) A Single Administration of CRISPR/Cas9 Lipid Nanoparticles Achieves Robust and Persistent In Vivo Genome Editing. *Cell Rep* **22**, 2227-2235
60. Chung, J. Y., Ain, Q. U., Song, Y., Yong, S. B., and Kim, Y. H. (2019) Targeted delivery of CRISPR interference system against Fabp4 to white adipocytes ameliorates obesity, inflammation, hepatic steatosis, and insulin resistance. *Genome Res* **29**, 1442-1452
61. Shen, Y., Cohen, J. L., Nicoloro, S. M., Kelly, M., Yenilmez, B., Henriques, F., Tsagkaraki, E., Edwards, Y. J. K., Hu, X., Friedline, R. H., Kim, J. K., and Czech, M. P. (2018) CRISPR-delivery particles targeting nuclear receptor-interacting protein 1 (Nrip1) in adipose cells to enhance energy expenditure. *J Biol Chem* **293**, 17291-17305
62. Kamble, P. G., Hetty, S., Vranic, M., Almby, K., Castillejo-Lopez, C., Abalo, X. M., Pereira, M. J., and Eriksson, J. W. (2020) Proof-of-concept for CRISPR/Cas9 gene editing in human preadipocytes: Deletion of FKBP5 and PPARG and effects on adipocyte differentiation and metabolism. *Sci Rep* **10**, 10565
63. Platt, R. J., Chen, S., Zhou, Y., Yim, M. J., Swiech, L., Kempton, H. R., Dahlman, J. E., Parnas, O., Eisenhaure, T. M., Jovanovic, M., Graham, D. B., Jhunjhunwala, S., Heidenreich, M., Xavier, R. J., Langer, R., Anderson, D. G., Hacohen, N., Regev, A., Feng, G., Sharp, P. A., and Zhang, F. (2014) CRISPR-Cas9 knockin mice for genome editing and cancer modeling. *Cell* **159**, 440-455
64. Dow, L. E., Fisher, J., O'Rourke, K. P., Muley, A., Kastenhuber, E. R., Livshits, G., Tschaharganeh, D. F., Socci, N. D., and Lowe, S. W. (2015) Inducible in vivo genome editing with CRISPR-Cas9. *Nat Biotechnol* **33**, 390-394
65. Cheng, M., Mei, B., Zhou, Q., Zhang, M., Huang, H., Han, L., and Huang, Q. (2018) Computational analyses of obesity associated loci generated by genome-wide association studies. *PLoS One* **13**, e0199987

CHAPTER II

Targeting Adipose Tissue Using Lipid Nanoparticles and Adeno-Associated Viruses

ABSTRACT

Transduction of adipose tissues is notoriously difficult as adipocytes are located throughout the body in distinct depots. Thus, we sought to identify strategies to maximize transduction of adipose tissues using viral and nonviral vectors. We formulated a library of lipid nanoparticles (LNPs) encapsulating messenger RNA (mRNA) or plasmid DNA (pDNA) using two microfluidics devices. Physical properties were fine-tuned by altering the genetic cargo, lipid molarity, nitrogen/phosphate (N/P) ratio, and flow rate. Lead LNP formulations demonstrated transfection without cytotoxicity *in vitro*. Additionally, we explored LNP biodistribution kinetics *in vivo* and found that genetic cargo strongly influenced biodistribution. pDNA loaded LNPs showed intrinsic affinity for white adipose tissues (WATs) but also transduced reticuloendothelial organs, indicating that additional work is required to impart increased adipose tissue tropism. While we were unable to demonstrate uptake by adipocytes *per se*, we show for the first time that systemic delivery of LNPs can be used to transfect adipose tissues. We then focused our attention to optimize adipose transduction using adeno-associated virus 8 (AAV8) by testing systemic and local routes of administration. Systemic delivery by intravenous injection and local delivery by intra-WAT injection did not effectively transduce adipose tissues. Interestingly, local delivery by intra-BAT injection led to robust transduction of brown adipocytes within the interscapular BAT. Thus, we propose intra-BAT injection as a delivery strategy to maximize brown adipocyte transduction. This may enable the use of AAV8 to administer CRISPR/Cas9 for inducible gene knockout as an efficient tool to study BAT.

INTRODUCTION

Targeted delivery of genetic materials to adipocytes represents a major hurdle for the field of adipose tissue research. This is largely because adipocytes are found throughout the body in unique depots and each depot is functionally distinct from others, leading some to propose that each should be classified as a separate “mini-organ” (1). Differential gene expression, variation in cellular composition, degree of vascularization, and neurological and/or hormonal factors also contribute to regional differences in adipose tissues (1-3). Moreover, adipocytes comprise a minority of the total cell population in each depot, which is predominantly populated by stromal vascular cells, macrophages, preadipocytes, and stem cells (4). Collectively, these characteristics complicate targeting adipocytes *in vivo*. Efficient transfection of adipocytes *in vitro* also remains challenging, as immortalized murine and human cell lines including 3T3-L1, BCF-1, HB2, human adipose-derived stem cells, and Simpson-Golabi-Behmel syndrome cells, are largely resistant to traditional transfection and electroporation techniques as compared to other cell types (5-7). In many ways, an inability to effectively transduce adipose tissues has caused the field to lag in implementing more advanced technologies such as CRISPR/Cas9 inducible gene knockout towards understanding adipose tissues.

Currently, the use of recombinant adeno-associated viruses (AAVs) is considered the “gold standard” for transducing adipocytes *in vivo* (8-10). In contrast to lentiviruses and adenoviruses, AAV remains episomal and does not elicit a strong immune response, which coupled with its multitude of capsid serotypes, makes it a favorable vector for gene transfer applications (11). Several studies have identified that AAV serotypes 8 and 9 show high affinity for adipose tissues (12-20). Collectively, these studies have helped shape the current “gold standard” approach for transducing adipose tissues, which posits that local delivery of recombinant AAV serotype 8 or 9 maximizes adipocyte transduction in white (WAT) and brown (BAT) adipose tissues (9). Although AAV8 and AAV9 have been used to transduce individual adipose depots, whole-body transduction of all adipose tissues has not been accomplished. Neither local delivery nor systemic delivery via intravenous injection, intraperitoneal injection, nor oral gavage have resulted in total transduction of all adipose depots across the body (9). For instance, following systemic

delivery of AAV8 or AAV9, Jimenez et al. reported broad variations in transduction efficiency across inguinal, retroperitoneal, mesenteric, and epididymal WAT as well as interscapular BAT (13). Moreover, variations in transduction efficiency were also observed across different genetic strains of mice (13). Despite the affinity of AAV8 and AAV9 for adipose tissue, systemic delivery primarily results in significant vector accumulation in liver. O'Neill and colleagues demonstrated that systemic delivery of AAV8 resulted in >200-fold more copies of AAV DNA in liver than in BAT, gonadal, or omental WATs (14). Thus, identifying alternative delivery strategies may be necessary to achieve whole-body adipose tissue transduction and limit accumulation in liver.

Nanoparticles (NPs) are an alternative delivery strategy that have recently been employed to target adipose tissues. Broadly speaking, NPs are nonviral vectors between 1-1000 nm in diameter that can facilitate the delivery of genetic and/or therapeutic cargoes to tissues of interest (21). NPs are classified according to the materials with which they are composed. For example, NPs can be categorized as polymeric (polymersomes, dendrimers, nanospheres), inorganic (quantum dots, iron oxide NPs, gold NPs), or lipid-based (liposomes, lipid NPs, emulsions) (22). Unlike viral vectors, NPs are synthetically produced, meaning particle architecture and composition can be fine-tuned for specific applications. A growing body of literature has begun to explore NPs for targeting adipose tissue (23-30). For instance, polymeric NPs have been functionalized to target WAT vasculature (24,25,28,29). Polymeric NPs have also been used to reduce inflammation in obese mice by binding to adipose tissue resident macrophages (26,27). Peptide-functionalized quantum dots have also been developed to image WAT vasculature in obese Wistar rats (30). However, while these studies demonstrate that NPs can be used to target WAT vasculature or resident macrophages, they ultimately fail to transfect adipocytes. In fact, the majority of transfection is observed in off-target tissues. Ma et al. reported accumulation of NPs predominantly in liver, lung, and kidney, with marginal transfection observed in epididymal, subcutaneous, and brown adipose tissues (27). Therefore, continued research is required to i.) demonstrate NP uptake by adipocytes, and ii.) prevent uptake in off-target tissues. To accomplish this, testing different classes of NPs, such as lipid-based NPs, is warranted.

Lipid nanoparticles (LNPs) represent a mature class of NP that have transformed the world as of recent by facilitating the delivery of mRNA for vaccination against SARS-CoV-2 (31). Relative to other NP classes, LNPs are significantly easier to manufacture and have a highly efficient encapsulation process to enable loading with oligonucleotides or plasmid DNA (pDNA) for gene transfer applications (32). LNPs are typically composed of a cationic ionizable lipid, a structural or "helper" lipid, cholesterol (Chol), and polyethyleneglycol (PEG) (33). A combination of these lipid specifies causes the destabilization of the endosomal membrane following cellular uptake and facilitates cytoplasmic release of the genetic cargo (34). Recently, LNPs have shown promise in targeting adipocytes *in vitro*. The Pharmaceutical Sciences iMed Biotech Unit at AstraZeneca utilized LNPs containing human erythropoietin mRNA and demonstrated gene transfer to cultured primary human adipocytes (35). To this point, however, the affinity of LNPs for adipose tissues has not been explored *in vivo*.

Thus, we formulated LNPs and tested their affinity for adipose tissues. We generated a library of LNPs using two different microfluidic devices to rapidly mix the cationic ionizable lipid DLin-MC3-DMA (MC3), distearoylphosphatidylcholine (DSPC), Chol, and PEG with pDNA or mRNA. LNPs ranged in size from 80-267 nm in diameter depending on the genetic cargo, lipid molarity, nitrogen/phosphate (N/P) ratio, and microfluidics device used to formulate the LNP. After assessing LNPs *in vitro*, we selected two formulations, one from each microfluidics device, for *in vivo* biodistribution studies. Interestingly, we found that LNP biodistribution following intravenous injection was strongly influenced by genetic cargo. IVIS imaging showed LNPs loaded with mRNA (mRNA-LNPs) mainly localized to liver and expression was maximal between 6-24 hours. By contrast, LNPs loaded with pDNA (pDNA-LNPs) were more broadly distributed across tissues, especially in WATs, and expression was maximal between 24-48 hours. Despite an affinity of pDNA-LNPs for adipose tissues, pDNA-LNPs were also detected in liver, spleen, kidney, lung, and heart, highlighting that systemic delivery of LNPs leads to off-target transfection. While we were unable to confirm that LNPs are taken up specifically by adipocytes, we show that pDNA-LNPs are intrinsically adipophilic, suggesting that conjugation with adipocyte-specific moieties may enhance tissue tropism.

We then shifted our focus towards applying AAV8 to transduce adipose tissues. Specifically, we explored how route of administration influences adipose tissue transduction. We found that local injection specifically to the interscapular BAT leads to robust transduction with minimal leak to liver. Interestingly, neither local delivery to the posterior subcutaneous WAT nor systemic delivery via intravenous injection resulted in sufficient transduction of WATs or BAT. Thus, we show that local injection of AAV8 to BAT facilitates efficient gene transfer and therefore may potentially enable the use of CRISPR/Cas9 inducible gene knockout as a tool to study adipose tissues *in vivo*.

RESULTS

Microfluidic mixing formulates LNPs with different physical properties

LNPs are typically formulated via the rapid mixing of nucleic acids dissolved in water (aqueous phase) and lipids dissolved in ethanol (lipid phase) (**Figure 2.1a**). Millisecond mixing of the lipid and aqueous phase drives the formation of an inverted micelle that encapsulates the nucleic acid and prevents aggregation to produce a monodisperse LNP suspension (32,36). We used two microfluidics devices to produce LNPs: the NanoAssemblr Benchtop and the Hamilton MicroLab Star. Both devices rely upon rapid mixing using a staggered herringbone microfluidic channel. Herringbone structures induce chaotic advection of laminar streams, which rapidly mixes the aqueous and lipid phases to increase polarity, leading to LNP precipitation (36). This process enables "bottom-up" synthesis of LNPs by spontaneous self-assembly. We followed the protocol established by Belliveau et al. to formulate LNPs containing MC3:DSPC:Chol:PEG (50:10:38.5:1.5) and loaded LNPs with pDNA encoding mCherry at a ratio of 1:3 (lipid:pDNA) (37). In total, we formulated four LNP formulations using the NanoAssemblr (N1, N2, N3, N4), and four LNP formulations using the Hamilton (H1, H2, H3, H4) (**Figure 2.1b-c, Table 2.1**). We varied lipid molarity, N/P ratio, mixing speed, and PEG content which influenced both the diameter and polydispersity index ($Đ_M$) of the LNPs (**Figure 2.1b-c, Table 2.1**). The N/P ratio is the ratio of positively charged amines (MC3) to negatively charged nucleic acid phosphates (pDNA). The N/P ratio influences LNP surface charge, size, and stability, with higher N/P ratios enhancing intracellular delivery (38). In general, a net positive N/P ratio has been reported to improve LNP efficacy for

gene transfer applications; however, too high of a positive ratio can be cytotoxic (39). Our pDNA-LNPs had a N/P ratio between 6.2-12.4, which is in line with previously established systems (**Table 2.1**) (33). We measured LNP size using dynamic light scattering, which calculates the hydrodynamic diameter by measuring the speed of LNPs dispersed in solution, given by the Stokes-Einstein equation:

$$D_h = \frac{k_B T}{3\pi\eta D_t}$$

Where D_h = translational diffusion coefficient [m^2/s], k_B = Boltzmann constant [m^2kg/Ks^2], T = temperature [K], η = viscosity [Pa·s], and D_t = hydrodynamic radius [m] (40). pDNA-LNPs formulated using the NanoAssemblr were smaller (91-127 nm) compared to LNPs generated using the Hamilton (170-267 nm) (**Figure 2.1b**). This is likely caused by differences in the microfluidics channels between the two devices. Dynamic light scattering was also used to calculate polydispersity index ($Đ_M$):

$$Đ_M = \frac{M_W}{M_n}$$

Where $Đ_M$ = polydispersity index, M_W = weight average molecular weight, and M_n = number average molecular weight (40). All pDNA-LNPs formulated by the NanoAssemblr, or Hamilton were homogenous in size and distribution (**Figure 2.1c**).

LNPs transfect cells *in vitro* and are non-cytotoxic

Positively charged LNPs interact with negatively charged cell surfaces and are taken up via endocytosis (**Figure 2.2a**) (39). Once inside an endosome, the cationic MC3 lipid destabilizes the membrane by forming ion pairs with anionic phospholipids in the endosomal membrane, causing the membrane to adopt a non-bilayer lipid structure and allowing the pDNA to escape into the cytosol (**Figure 2.2a**) (34). To test if the NanoAssemblr and Hamilton LNPs followed this mechanism, we transfected B16-F10 cells using LNPs loaded with mCherry pDNA. We selected two LNP formulations–one

formulated using the NanoAssemblr (N2-LNP) and the other using the Hamilton (H2-LNP)– based on size, N/P ratio, and encapsulation efficiency (**Figure 2.1b-c, Table 2.1, Figure 2.2b**). While a multitude of studies have shown efficient delivery of siRNA or mRNA using LNPs, much less is known about their ability to deliver pDNA. This stems from differences in size and charge of pDNA compared to smaller oligonucleotide cargoes, which necessitates modification of lipid and N/P charge ratios to maximize cellular uptake (33). Both N2-LNPs and H2-LNPs had a N/P ratio of 9.3 (**Table 2.1**). Based on this, we were able to estimate that mCherry pDNA (5.3 kb; 5.3×10^3 total negative charges) corresponds to 4.9×10^4 amino-lipids per pDNA, which reflects a condensed structure of the encapsulated pDNA (33).

Next, N2-LNPs and H2-LNPs were transfected into murine B16-F10 cells and mCherry expression was monitored in real-time (**Figure 2.2c**). We dosed LNPs at concentrations of 1 μg/mL, 3 μg/mL, and 6 μg/mL, and used Lipofectamine 3000 as a positive control to assess transfection efficiency. We observed a dose-dependent increase in mCherry expression for both N2-LNPs and H2-LNPs (**Figure 2.2c-d**). N2-LNPs were more efficient, with maximal transfection in 33% of cells observed at 72 hours compared to H2-LNPs, which had maximal transfection of 11% at 84 hours (**Figure 2.2c**). This is likely due to the differences in size between the two LNPs, as smaller LNP systems have improved transfection potency (**Figure 2.1b, Table 2.1**) (33,41). Additionally, the percent encapsulated pDNA was higher in the N2-LNPs compared to H2-LNPs (92% and 68%), which might also account for the differences in mCherry expression (**Figure 2.2b**). Although Lipofectamine 3000 showed maximal transfection at 30 hours and transfected ~40% of cells, it was also much harsher relative to both N2-LNPs and H2-LNPs when used to dose an equal amount of pDNA (**Figure 2.2e**). Collectively, these data show that N2-LNPs and H2-LNPs can deliver pDNA to cells *in vitro* and are non-cytotoxic.

Systemic delivery of mRNA-LNPs primary transfects liver but not adipose tissues

LNPs have been used extensively for the delivery of mRNA both experimentally in animal models and clinically in humans, however, their affinity for adipose tissues following systemic delivery has not been reported (31,32,42,43). Thus, we sought to characterize the biodistribution kinetics of N2-LNPs and H2-LNPs loaded with luciferase mRNA. LNPs

were formulated as described previously, with the lipid to nucleotide mass ratio adjusted to 20:1 to account for the mRNA cargo. As a result, mRNA-LNPs were smaller compared to pDNA-LNPs; N2-LNPs were 80 nm in diameter while H2-LNPs were 176 nm in diameter, respectively (**Figure 2.3a**). To assess biodistribution kinetics, mice were injected with 0.25 mg/kg N2-LNP or H2-LNP by intravenous injection via the tail vein and imaged at 6 and 24 hours post injection (n = 3 mice) (**Figure 2.3a**). Prior to imaging, mice were administered 150 mg/kg of D-luciferin by intraperitoneal injection. Maximal luminescence was detected at 6 hours post injection for both N2-LNPs and H2-LNPs (**Figure 2.3a**). Interestingly, H2-LNPs showed a higher average radiance compared to N2-LNPs, despite having a larger diameter (**Figure 2.3a**). IVIS imaging suggested both N2-LNPs and H2-LNPs localized to liver at both 6 and 24 hours, with decreased luminescence detected at 24 hours post injection (data not shown). To further assess tissue biodistribution, mice were sacrificed at 24 hours and tissues were imaged for luciferase expression. We observed robust luminescence in liver for both N2-LNPs and H2-LNPs and mild signal in posterior subcutaneous WAT (psWAT) and spleen, but no indication of sufficient transfection of BAT or epididymal WAT (eWAT) (**Figure 2.3b**). These results demonstrate that mRNA-LNPs do not show inherent affinity for adipose tissues.

pDNA-LNPs localize to adipose tissues and reticuloendothelial organs following systemic delivery

We next sought to explore the biodistribution kinetics of LNPs loaded with luciferase pDNA to see if altering the genetic cargo influenced transfection efficiency *in vivo*. LNPs were formulated as described above, however, the ratio of lipid to pDNA was adjusted to 33:1 to compensate for the larger genetic cargo. Relative to mRNA-LNPs, pDNA-LNPs were larger in size; N2-LNPs were 132 nm in diameter and H2-LNPs were 199 nm in diameter, respectively (**Figure 2.4a**). Mice were injected with 0.25 mg/kg N2-LNP or H2-LNP by intravenous injection via the tail vein and were administered 150 mg/kg of D-luciferin by intraperitoneal injection prior to imaging (n = 3). Luminescence was not detected at 6 or 24 hours post injection (data not shown), but robust signal was observed throughout the abdomen after 48 hours (**Figure 2.4a**). The delayed onset of luciferase

expression arises because pDNA must first be transcribed to mRNA before it is translated to luciferase protein. There was no difference in transfection efficiency between N2-LNPs and H2-LNPs as measured by average radiance (**Figure 2.4a**). After 48 hours, mice were sacrificed, and tissues were imaged to characterize biodistribution kinetics. Interestingly, we observed pronounced luminescence signal in the psWAT and eWAT with reduced signal detected in liver (**Figure 2.4b**). N2-LNPs and H2-LNPs also localized to BAT, spleen, kidney, lung, and heart.

The mechanism by which pDNA-LNPs and not mRNA-LNPs localize to WATs remains to be determined. Following systemic delivery into the bloodstream, LNPs become opsonized, a process by which nonspecific proteins coat the surface of the LNP (44). Physical properties, such as charge, size, and surface composition influence the protein “corona” that forms around the LNP. The proteins that bind to the surface of the LNP can have important consequences on its biodistribution kinetics. For instance, opsonized LNPs can be taken up by Kupffer cells in the liver or by macrophages in the spleen, as well as by other phagocytic cells of the reticuloendothelial system for degradation (44). In general, opsonization of LNPs is governed by hydrophobic and electrostatic interactions of proteins with the surface of the LNP (45,46). Given the differences in size of mRNA and pDNA cargoes, we had to adjust the ratio of lipid to nucleic acid to formulate mRNA-LNPs and pDNA-LNPs. As a result, the surface charge and LNP size was different. Lundqvist et al. showed that NP size and charge strongly influence the protein corona (47). Thus, although the lipid species utilized to formulate mRNA-LNPs and pDNA-LNPs were the same, the different physical properties of each likely account for changes in biodistribution kinetics.

While we did observe luminescence in psWAT, eWAT, and minor signal in BAT, we were unable to confirm if pDNA-LNPs were taken up by adipocytes or by stromal vascular cells (**Figure 2.4b**). It is possible that LNPs home to adipose tissues but remain trapped in the adipose tissue vasculature, or are phagocytosed by resident macrophages which take up the opsonin-coated LNPs (47). Future work will therefore need to validate LNP affinity for adipocytes, perhaps by administering LNPs loaded with Cre-recombinase pDNA to mT/mG reporter mice (48). Moreover, significant work is required to promote transfection of all adipose tissues throughout the body and to reduce LNP accumulation

in off-target organs. Thus, while these initial results using LNPs show promise, they unfortunately fail to resolve the issue of sufficiently targeting all adipose tissues. Therefore, we shifted our focus back to optimizing the current gold standard approach for transducing adipose tissues: adeno-associated virus 8 (AAV8).

Route of administration strongly influences AAV8 transduction efficiency of adipose tissues

AAV8 remains the gold standard for transducing adipose tissues, however, the broad variability in transduction efficiency and lack of consistency in assessing degree of transduction that have been reported in the literature call into question its true affinity for adipose tissues (8-10). Careful assessment of the literature has shown that route of administration plays an important role in AAV8 biodistribution (9). In order to assess how route of administration influences adipose tissue transduction, we administered AAV8-mCherry to mice via three different routes of administration: systemic delivery by intravenous injection, local delivery by intra-BAT injection, and local delivery by intra-WAT injection.

Mice were administered 100 µL 10^{12} vg/mL AAV8-mCherry according to previously established protocols (13,49). Intravenous injection was accomplished via the tail vein, whereas intra-BAT and intra-WAT injections were performed by making a 1-2 cm incision and peeling back the skin to visualize the interscapular BAT or the posterior subcutaneous WAT and injecting AAV8-mCherry directly into the depot **(Figure 2.5a-c**) (13,49). Mice were sacrificed 14 days after injection and tissues were analyzed for AAV8 biodistribution and adipocyte transduction efficiency. Quantitative PCR (qPCR) indicated that *mCherry* mRNA tissue expression was influenced entirely by route of administration (**Figure 2.5a-c**). Intravenous injection resulted in pronounced *mCherry* expression in liver, and confocal microscopy confirmed transduction was liver-specific with very few adipocytes transduced in BAT and psWAT (**Figure 2.5a, 2.5d**). By contrast, local delivery via intra-BAT injection led to robust mCherry signal in BAT and reduced signal detected in liver (**Figure 2.5b, 2.5d**). We did not detect mCherry expression in WATs using intra-BAT injection. Interestingly, local delivery via intra-WAT injection led to mild transduction of both psWAT and BAT, with robust mCherry expression detected in liver (**Figure 2.5c,**

2.5d). We did not observe transduction of eWAT in any route tested (**Figure 2.5a-d**). Thus, we unfortunately were unable to transduce all adipose tissues regardless of the route by which AAV8-mCherry was administered. We did however notice an apparent affinity of AAV8 for BAT, as each route showed positive transduction of brown adipocytes in the interscapular depot (**Figure 2.5a-d**). BAT is a unique adipose tissue involved in adaptive thermogenesis and in rodents is found predominantly in an easily accessible interscapular location (2,3,48,50). BAT also has important endocrine functions and in humans is inversely associated with body mass index (51,52). Thus, based on these results, we reframed our approach to focus on applying AAV8 to facilitate CRISPR/Cas9 for use in adipose tissue. In chapter 3, we demonstrate for the first time that local injection of AAV8 enables CRISPR/Cas9 inducible gene knockout in BAT.

DISCUSSION

An emerging trend to model disease or study gene function has focused on the delivery of CRISPR/Cas9 to tissues of interest. Viral transduction, nonviral transfection, and/or combination with transgenic Cas9 animal models has enabled use of CRISPR/Cas9 in tissues such as liver, heart, skeletal muscle, and the central nervous system for somatic gene editing (53,54). As highlighted above, targeting adipose tissues using viral or nonviral approaches has proved a major challenge for the field and has therefore prevented the delivery of CRISPR/Cas9 to improve our understanding of these metabolically important organs. In this work we report preliminary results on the use of LNPs to target adipose tissues *in vivo*. While we were unable to show that pDNA-LNPs directly transfect adipocytes *per se*, we provide evidence that pDNA-LNPs have inherent tropism to adipose tissues, suggesting that further optimization can lead to robust adipocyte transduction and limited uptake in off-target organs. We also show that local delivery of AAV8 to BAT yields sufficient transduction of brown adipocytes with minimal leak to liver. Ultimately, we anticipate that future work will build off these preliminary data to identify strategies that improve transduction to enable delivery of CRISPR/Cas9 to adipose tissues.

In this study, two microfluidics devices were used to formulate a library of LNPs encapsulating pDNA via the rapid mixing of aqueous and lipid phases. This generated LNPs ranging in size from 80-267 nm in diameter. We found that LNP size was largely determined by the microfluidic device used to formulate the LNPs, with formulations generated using the NanoAssemblr having a smaller size than those generated using the Hamilton. The size of LNPs was also influenced by the PEG content, as formulations N3-LNP and H3-LNP, in which the PEG molarity was increased to 2.5 mM and Chol decreased to 37.5 mM, were 91 nm and 182 nm in diameter, respectively. PEG resides in the outer monolayer of the LNP and allows higher surface-to-volume ratios that results in smaller limit sizes as the PEG content is increased (37,55). PEG also decreases the adsorption of serum proteins involved in the opsonization process, which can improve delivery *in vivo* (56). While PEG can impart beneficial physical properties to LNPs, multiple studies have reported unexpected immunological responses to PEG-conjugated NPs (57). Therefore, future formulations should consider these factors to decrease LNP size, shield LNPs from opsonization, and prevent immunological responses.

LNPs used for *in vitro* and *in vivo* studies were all composed of the same four lipid species: MC3:DSPC:Chol:PEG. We chose MC3 as the cationic lipid because it has been used extensively for efficient *in vivo* delivery of nucleic acids and is non-cytotoxic (33,37,58). MC3 has a pKa of 6.4, which is low enough that the LNP is tolerated at physiological pH but high enough that it is ionized at endosomal pH to disrupt the endosomal membrane (59). Several other cationic lipids have been used to formulate LNPs. For example, the amino-lipids DLin-KC2-DMA, DLinDMA, DLinDAP, DOTAP, and DSGLA have all been used (60-62). Moreover, a variety of helper lipids have also been tested. For example, Kulkarni et al. demonstrated that LNPs containing the helper lipids DOPE or DOPC showed improved transfection *in vivo* compared to LNPs containing DSPC (33). Thus, altering the lipid composition of LNPs may lead to improved affinity for adipose tissue. Additionally, conjugating LNPs with adipophilic moieties may improve transduction. For instance, the peptide sequence CKGGRAKDC, which binds to prohibitin in WAT vasculature, has been shown to enhance homing of NPs to adipose tissues (28-30). Future LNP formulations will thus require careful design using different combinations

of cationic lipids, helper lipids, PEG content, and peptide sequences to impart specificity and prevent off-target accumulation.

Interestingly, we observed differences in the uptake kinetics of LNPs *in vitro* and *in vivo*. For instance, N2-LNPs vastly outperformed H2-LNPs in transfecting cells in culture, however, *in vivo*, both N2-LNPs and H2-LNPs loaded with pDNA transfected tissues to a similar degree. In fact, *in vitro* experiments are typically poor indicators for *in vivo* bioavailability of NPs. This is because *in vitro* systems lack the complexities associated with *in vivo* systems, in which a number of variables affect transfection efficiency (63). Whitehead et al. reported that using primary hepatocytes to test LNP systems *in vitro* had the best correlations with *in vivo* studies in which LNPs were targeted to liver, suggesting that when possible, primary cell lines should be used to most closely model *in vivo* kinetics (63). In our studies, we performed *in vitro* studies using B16-F10 cancer cells, as well as immortalized 3T3-L1 cells. While we did observe transfection of B16-F10 cells, we were unsuccessful in transfecting preadipocyte and differentiated 3T3-L1s (data not shown). For future studies, however, transfecting primary preadipocytes and differentiated adipocytes should be attempted, and results compared to *in vivo* studies to determine if corollaries exist. Such research can be used to significantly enhance LNP affinity for adipose tissues.

Although we were able to demonstrate transfection of WATs *in vivo*, we were unable to determine if LNPs were taken-up by adipocytes or stromal vascular cells. As such, we shifted our attention back to the current gold standard, AAV8. We showed that local delivery of AAV8 led to robust transduction of brown adipocytes within BAT, and therefore decided to focus on targeting BAT for CRISPR/Cas9 inducible gene knockout. To ultimately realize CRISPR/Cas9 inducible gene knockout in adipose tissues, however, significant work is required. First, packaging limitations of AAV prevent the incorporation of both Cas9 and a single guide RNA (sgRNA) (9,10). To overcome this, transgenic Cas9 expressing mice should therefore be considered (64). Second, because AAV8 also transduces liver when administered by local injection to the interscapular BAT, transcriptional control features should be utilized to prevent off-target mutations in non-target tissues. Thus, we hope that lessons from this study provide a foundational context

for future studies that seek to apply LNPs or AAV8 to induce CRISPR/Cas9 gene knockout in adipose tissues.

MATERIALS AND METHODS

LNP Formulation and Characterization

LNPs were formulated by following the protocol established by Belliveau et al. (37). For *in vitro* studies, LNPs were loaded with pDNA containing mCherry (#87916, Addgene, Watertown, MA, USA). pDNA was prepared in 25 mM citrate buffer at pH 4.0 to create the aqueous phase. The lipid phase was prepared by dissolving DLin-MC3-DMA (545-70-2, AstraZeneca R&D Charnwood, Loughborough, UK), distearoylphosphatidylcholine, cholesterol, and polyethyleneglycol (AstraZeneca Granta Park, Cambridge, UK) in 100% ethanol at a molar ratio of 50:10:38.5:1.5. The aqueous and lipid phases were rapidly mixed using two microfluidic devices, the NanoAssemblr Benchtop (Precision Nanosystems, Vancouver, BC, Canada) or the Hamilton MicroLab Star (Hamilton, Reno, NV, USA) according to the flow rate outlined in the text. LNPs were then dialyzed in PBS at 4ºC overnight. Dynamic light scattering was used to determine LNP size and polydispersity index. In brief, 10 µL of dialyzed LNPs were diluted in 700 µL PBS and analyzed at a fixed temperature of 25ºC. Encapsulation efficiency was calculated by incubating LNPs with nucleic acid green dye to measure the amount of free pDNA that was not encapsulated. LNPs were then incubated with Triton X to break open the LNPs and nucleic acid green dye was added to stain the encapsulated pDNA. Absorbance was read using a plate reader at 480 nm excitation. Percent encapsulation was then calculated by subtracting free pDNA from encapsulated DNA and dividing that number by the total pDNA.

Cell Culture

Murine B16-F10 cells were cultured at 5% CO_2 and maintained in DMEM:F12 medium (Thermo Fisher Scientific, Waltham, MA, USA) containing 10% fetal bovine serum and 1% Penicillin-Streptomycin (Thermo Fisher Scientific, Waltham, MA, USA). LNP transfection was performed when cells reached 90% confluence. LNPs were diluted in media to reach a concentration of 1 µg/mL, 3 µg/mL, and 6 µg/mL and were added directly to cells. Lipofectamine 3000 was used by following the manufacturer's protocol (Thermo Fisher Scientific, Waltham, MA, USA). Real-time cell imaging was done using the

IncuCyte ZOOM (Essen BioScience, Inc., Ann Arbor, MI, USA). Fluorescence and confluence were measured and analyzed using the IncuCyte ZOOM Analysis software.

LNP In Vivo Studies

Male albino mice (AstraZeneca Granta Park, Cambridge, UK) were administered 100 µL N2-LNP or H2-LNP loaded with mRNA luciferase (CleanCap Fluc mRNA, L-7602, TriLink Biotechnologies, San Diego, CA, USA) or pDNA luciferase at a dose of 0.25 mg/kg. Control mice were administered 100 µL PBS. Mice were injected with 150 mg/kg of D-luciferin by intraperitoneal injection prior to imaging at 6, 24, and 48 hours post LNP injection, anesthetized with 2-4% inhaled isoflurane in O_2, and imaged using the IVIS Spectrum In Vivo Imaging System (PerkinElmer, Waltham, MA, USA). All animal studies were approved by and conducted in compliance with the polices of AstraZeneca UK.

AAV Production

The AAV expression plasmid containing mCherry (#87916, Addgene, Watertown, MA, USA) was transformed into competent DH5α *E. coli* (Thermo Fisher Scientific, Waltham, MA, USA). Plasmids were isolated using the Qiagen Plasmid Maxi Kit (Qiagen, Hilden Germany). Isolated mCherry pDNA was then used to generate AAV8 by the University of Michigan Vector Core.

AAV In Vivo Studies

Male C57BL/6J mice (#000664, Jackson Labs, Bar Harbor, ME, USA) were injected with AAV8 as previously described (8,49). For intravenous injection, 100 µL 10^{12} vg/mL AAV8-mCherry was administered via the tail vein. For intra-BAT and intra-WAT injection, mice were anesthetized with 2-4% inhaled isoflurane in O_2 and a small area in the interscapular region or posterior subcutaneous region was shaved to access BAT of psWAT. A 1-2 cm incision was made, and the skin was peeled back to visualize the interscapular BAT or psWAT. For each, 100 µL 10^{12} vg/mL AAV8-mCherry was administered to each tissue by inserting the needle into the depot at 2-3 distinct sport and dispensing the virus. Freshly dissected tissues were placed in PBS and stored on ice followed by imaging using a Nikon A1 laser scanning confocal microscope.

Quantitative PCR

Total RNA was purified from frozen tissue using RNA STAT-60 (Tel Test, Alvin, TX, USA) according to the manufacturer's instructions. One µg of total RNA was reverse-transcribed to cDNA using M-MLV Reverse Transcriptase (Invitrogen, Carlsbad, CA, USA). qPCR was performed using a StepOnePlus System (Applied Biosystems, Beverly Hills, MI, USA). mCherry qPCR primers (mCherry qPCR F: GAGGCTGAAGCTGAAGGAC, mCherry qPCR R: GATGGTGTAGTCCTCGTTGTG) were validated with a cDNA titration curve and product specificity was evaluated by melting curve analysis and gel electrophoresis of the qPCR products. Gene expression was calculated using a cDNA titration curve within each plate and then normalized to the expression of peptidylprolyl isomerase A (*Ppia*) mRNA (Ppia qPCR F: CACCGTGTTCTTCGACATCA, Ppia qPCR R: CAGTGCTCAGAGCTCGAAAGT).

TABLE 2.1

Device	Formulation	Lipid Molarity (mM)	PEG Molarity (mM)	N/P Ratio	Mixing Rate (mL/min)	Diameter (nm)	$Đ_M$
NanoAssemblr Benchtop	N1	5.0	1.5	6.2	12	127	0.26
	N2*	7.5	1.5	9.3	18	100	0.23
	N3	7.5	2.5	9.3	18	91	0.25
	N4	10.0	1.5	12.4	18	99	0.23
Hamilton MicroLab Star	H1	5.0	1.5	6.2	18	170	0.15
	H2*	7.5	1.5	9.3	18	210	0.18
	H3	7.5	2.5	9.3	18	182	0.18
	H4	7.5	1.5	9.3	18	267	0.37

* = Lead formulation

Table 2.1. Physical properties of LNPs. A library of LNPs was generated using two microfluidics devices: the NanoAssemblr Benchtop and the Hamilton MicroLab Star. By altering the lipid molarity, PEG molarity, N/P ratio, and mixing rate, we were able to formulate LNPs with different sizes and physical characteristics. * indicates the lead formulation for each microfluidics device.

FIGURE 2.1

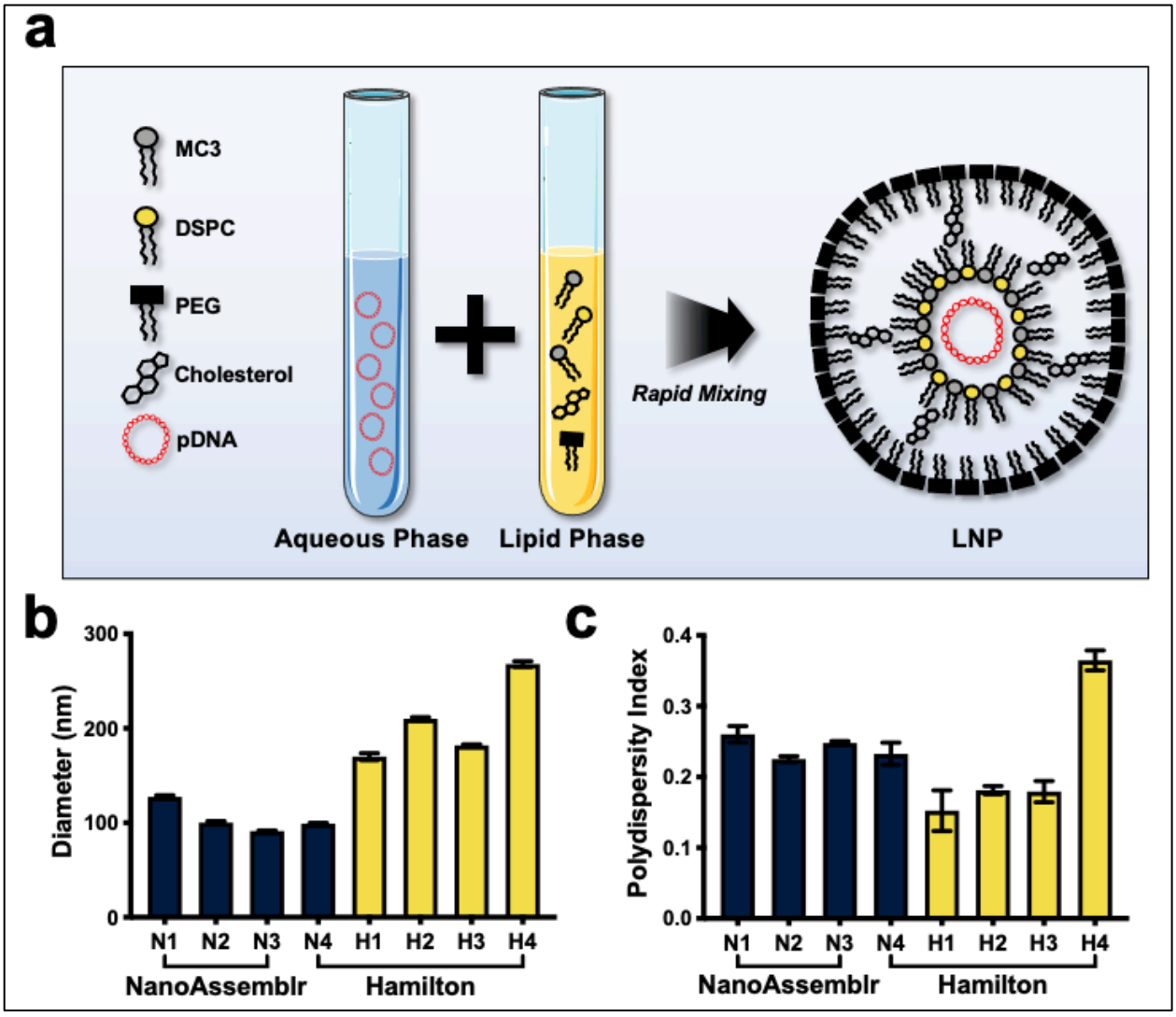

Figure 2.1. Microfluidic mixing formulates LNPs with different physical properties. (***a***) LNPs were formulated by the rapid mixing of aqueous and lipid phases to create a monodisperse suspension of LNPs encapsulating pDNA. (***b-c***) LNPs diameter and polydispersity index were determined using dynamic light scattering. In total, four formulations were generated using the NanoAssemblr Benchtop (N1, N2, N3, N4) and Hamilton MicroLab Star (H1, H2, H3, H4). Error bars represent standard deviation of diameter and polydispersity index as measured from three technical replicates. Figure is adapted from Cullis et al. (32).

FIGURE 2.2

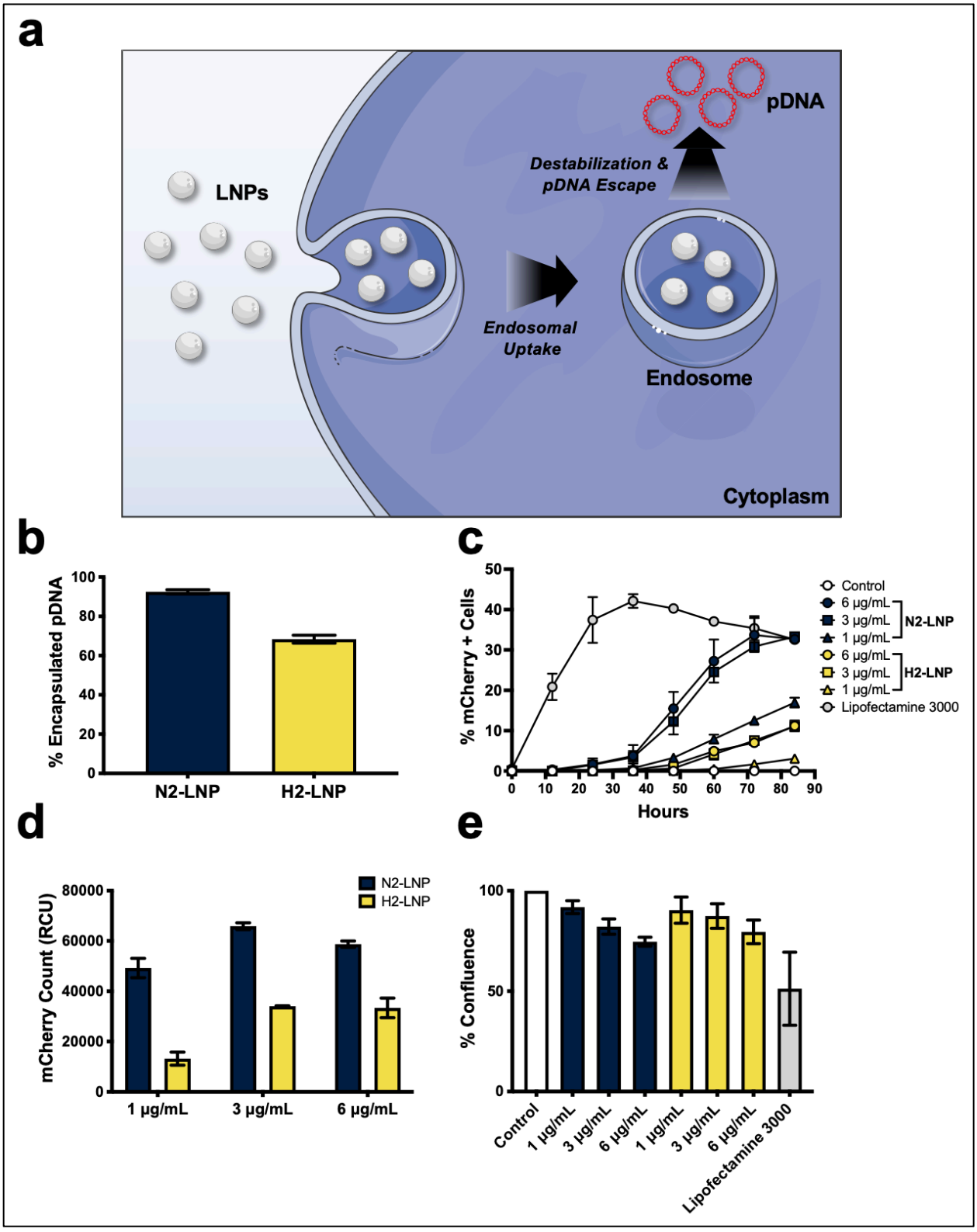
a
pDNA
Destabilization &
pDNA Escape
LNPs
Endosomal
Uptake
Endosome
Cytoplasm
b
% Encapsulated pDNA
100
80
60
40
20
0
N2-LNP
H2-LNP
c
% mCherry + Cells
50
40
30
20
10
0
0 10 20 30 40 50 60 70 80 90
Hours
Control
6 µg/mL
3 µg/mL
1 µg/mL
N2-LNP
6 µg/mL
3 µg/mL
1 µg/mL
H2-LNP
Lipofectamine 3000
d
mCherry Count (RCU)
80000
60000
40000
20000
0
N2-LNP
H2-LNP
1 µg/mL
3 µg/mL
6 µg/mL
e
% Confluence
100
50
0
Control
1 µg/mL
3 µg/mL
6 µg/mL
1 µg/mL
3 µg/mL
6 µg/mL
Lipofectamine 3000

Figure 2.2. LNPs transfect cells *in vitro* and are non-cytotoxic. (***a***) LNP cellular transfection proceeds by endosomal-mediated uptake, destabilization of the endosomal membrane, and release of pDNA. (***b***) Percent encapsulated pDNA in N2-LNPs and H2-LNPs. (***c***) Percent $mCherry^{+}$ B16-F10 cells over 84 hours. (***d***) mCherry count (red calibrated unit [RCU]) after 84 hours for N2-LNPs and H2-LNPs at increasing doses. (***e***) Percent confluence of B16-F10 cells after 84 hours of treatment with LNPs or Lipofectamine 3000; data is normalized to the control. Error bars represent standard deviation, and all experiments were run in triplicate.

FIGURE 2.3

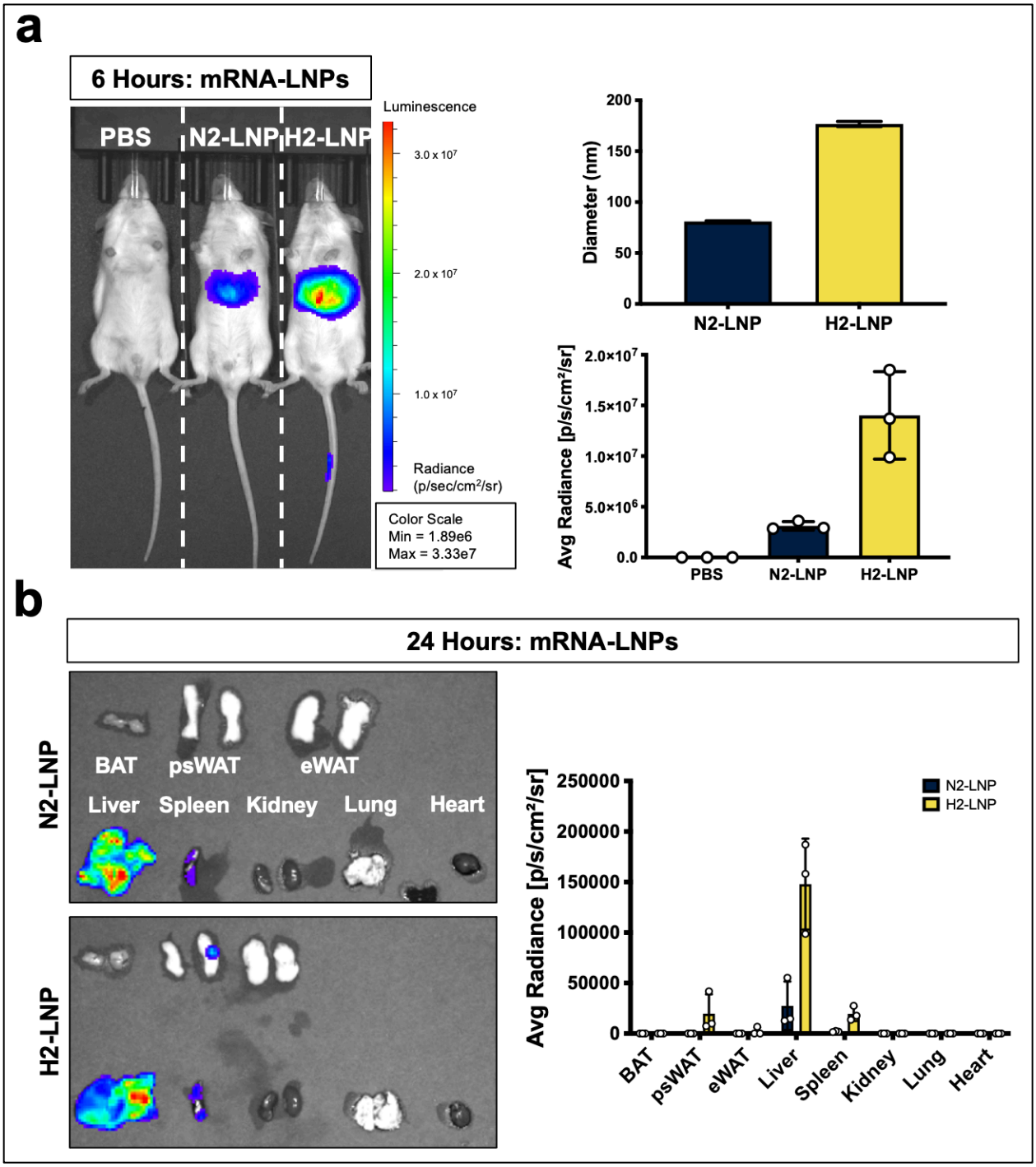

Figure 2.3. Systemic delivery of mRNA-LNPs primarily transfects liver but not adipose tissues. (***a***) Representative IVIS images of mice 6 hours post injection with PBS, N2-LNPs, or H2-LNPs (0.25 mg/kg) loaded with luciferase mRNA (n = 3). Average radiance taken at 6 hours post injection. Diameter of LNPs as measured by dynamic light scattering. (***b***) Average radiance in BAT, psWAT, eWAT, liver, spleen, kidney, lung, and

heart 24 hours after injection. All data are from male mice. Error bars represent standard deviation.

FIGURE 2.4

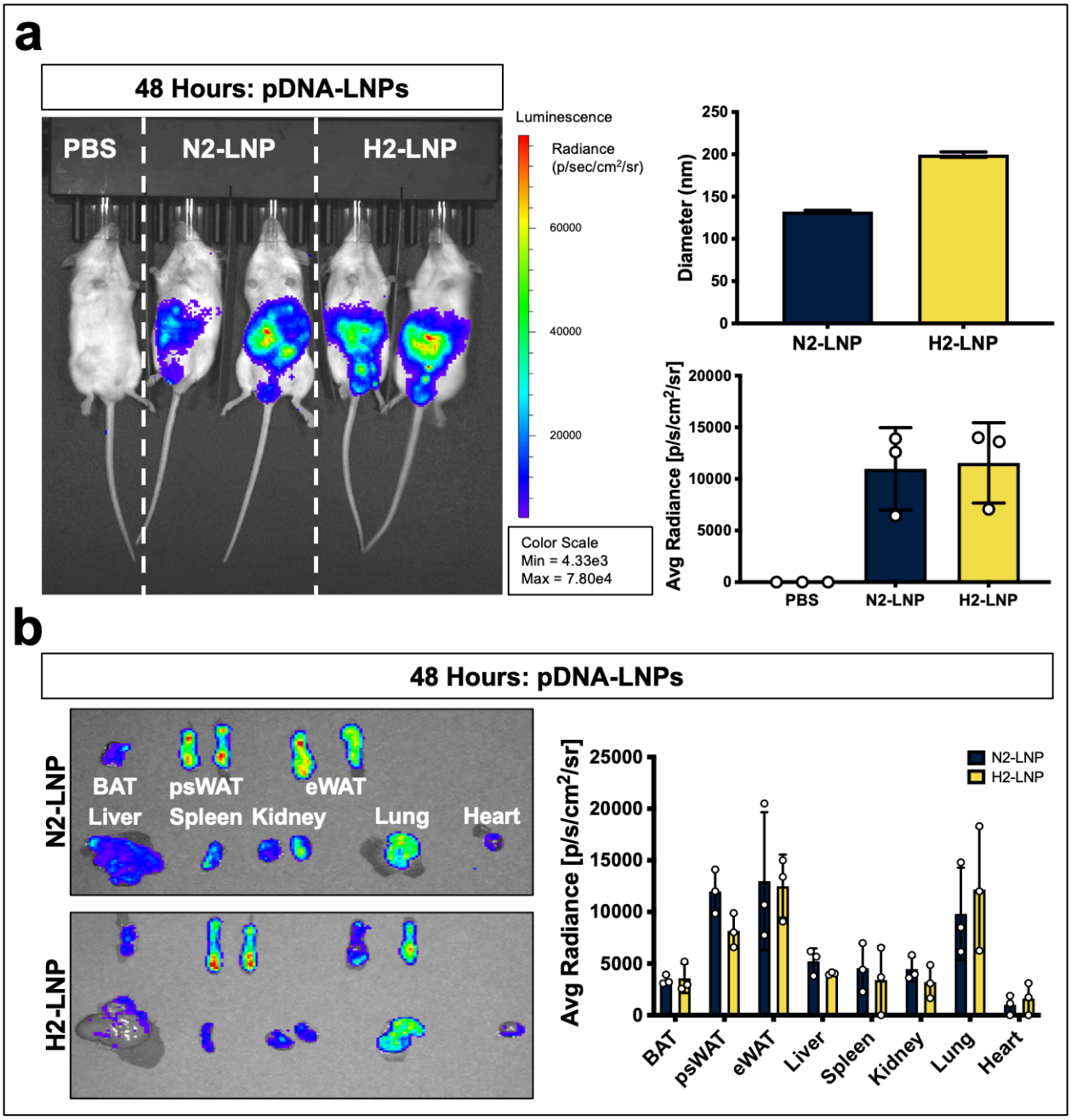

Figure 2.4. pDNA-LNPs localize to adipose tissues and reticuloendothelial organs following systemic delivery. (***a***) IVIS images of mice 48 hours post injection with LNPs (0.25 mg/kg) loaded with luciferase pDNA (n = 3). Average radiance at 48 hours post injection. LNP diameter was determined by dynamic light scattering. (***b***) Average radiance of various tissues taken at 48 hours after injection. All data are from male mice. Error bars represent standard deviation.

FIGURE 2.5

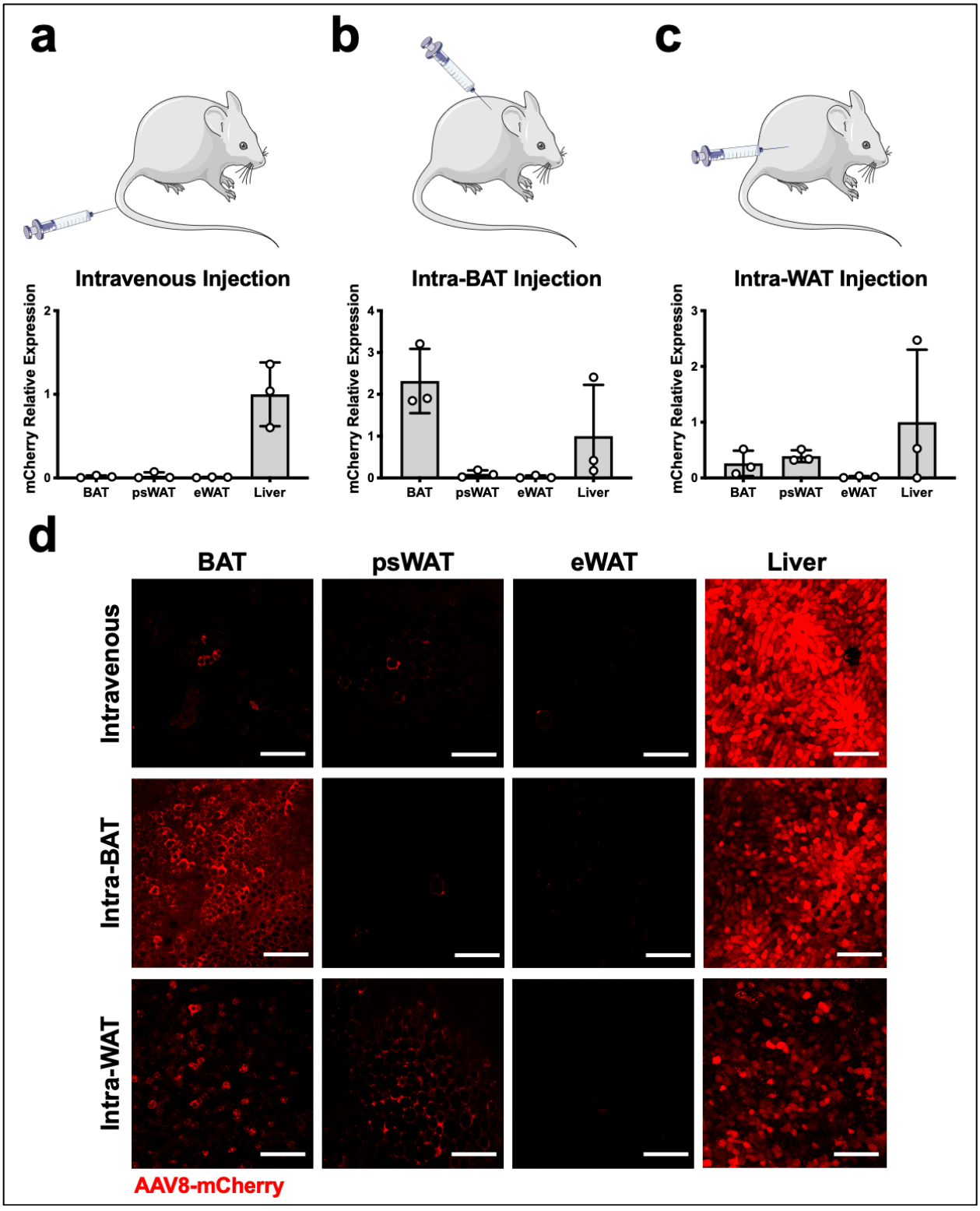
a
b
c
Intravenous Injection
Intra-BAT Injection
Intra-WAT Injection
mCherry Relative Expression
BAT
psWAT
eWAT
Liver
d
Intravenous
Intra-BAT
Intra-WAT
AAV8-mCherry

Figure 2.5. Route of administration strongly influences AAV8 transduction efficiency of adipose tissues. (***a***) Mice administered 100 µL 10^{12} vg/mL AAV8-mCherry by intravenous injection via the tail vein (n = 3). Relative *mCherry* mRNA expression; mRNA normalized to *Ppia*. (***b***) Mice 100 µL 10^{12} vg/mL AAV8-mCherry by intra-BAT injection (n = 3). Relative *mCherry* mRNA expression; mRNA normalized to *Ppia*. (***c***) Mice 100 µL 10^{12} vg/mL AAV8-mCherry by intra-WAT injection (n = 3). Relative *mCherry* mRNA expression; mRNA normalized to *Ppia*. (***d***) Confocal microscopy of freshly dissected BAT, psWAT, eWAT, and liver from mice 14 days post injection; 200x magnification, scale bar, 100 µm (n = 3). Data shown are from male mice. Error bars represent standard deviation.

REFERENCES

1. Tchkonia, T., Thomou, T., Zhu, Y., Karagiannides, I., Pothoulakis, C., Jensen, M. D., and Kirkland, J. L. (2013) Mechanisms and metabolic implications of regional differences among fat depots. *Cell Metab* **17**, 644-656
2. Bagchi, D. P., Forss, I., Mandrup, S., and MacDougald, O. A. (2018) SnapShot: Niche Determines Adipocyte Character I. *Cell Metab* **27**, 264-264 e261
3. Bagchi, D. P., Forss, I., Mandrup, S., and MacDougald, O. A. (2018) SnapShot: Niche Determines Adipocyte Character II. *Cell Metab* **27**, 266-266 e261
4. Parlee, S. D., Lentz, S. I., Mori, H., and MacDougald, O. A. (2014) Quantifying size and number of adipocytes in adipose tissue. *Methods Enzymol* **537**, 93-122
5. Meunier-Durmort, C., Ferry, N., Hainque, B., Delattre, J., and Forest, C. (1996) Efficient transfer of regulated genes in adipocytes and hepatoma cells by the combination of liposomes and replication-deficient adenovirus. *Eur J Biochem* **237**, 660-667
6. Kilroy, G., Burk, D. H., and Floyd, Z. E. (2009) High efficiency lipid-based siRNA transfection of adipocytes in suspension. *PLoS One* **4**, e6940
7. Enlund, E., Fischer, S., Handrick, R., Otte, K., Debatin, K. M., Wabitsch, M., and Fischer-Posovszky, P. (2014) Establishment of lipofection for studying miRNA function in human adipocytes. *PLoS One* **9**, e98023
8. Gomez-Banoy, N., and Lo, J. C. (2017) Genetic Manipulation with Viral Vectors to Assess Metabolism and Adipose Tissue Function. *Methods Mol Biol* **1566**, 109-124
9. Romanelli, S. M., and MacDougald, O. A. (2020) Viral and Nonviral Transfer of Genetic Materials to Adipose Tissues: Toward a Gold Standard Approach. *Diabetes* **69**, 2581-2588
10. Bates, R., Huang, W., and Cao, L. (2020) Adipose Tissue: An Emerging Target for Adeno-associated Viral Vectors. *Mol Ther Methods Clin Dev* **19**, 236-249
11. Mingozzi, F., and High, K. A. (2011) Therapeutic in vivo gene transfer for genetic disease using AAV: progress and challenges. *Nat Rev Genet* **12**, 341-355
12. Mizukami, H., Mimuro, J., Ogura, T., Okada, T., Urabe, M., Kume, A., Sakata, Y., and Ozawa, K. (2006) Adipose tissue as a novel target for in vivo gene transfer by adeno-associated viral vectors. *Hum Gene Ther* **17**, 921-928
13. Jimenez, V., Munoz, S., Casana, E., Mallol, C., Elias, I., Jambrina, C., Ribera, A., Ferre, T., Franckhauser, S., and Bosch, F. (2013) In vivo adeno-associated viral vector-mediated genetic engineering of white and brown adipose tissue in adult mice. *Diabetes* **62**, 4012-4022
14. O'Neill, S. M., Hinkle, C., Chen, S. J., Sandhu, A., Hovhannisyan, R., Stephan, S., Lagor, W. R., Ahima, R. S., Johnston, J. C., and Reilly, M. P. (2014) Targeting adipose tissue via systemic gene therapy. *Gene Ther* **21**, 653-661
15. Liu, X., Magee, D., Wang, C., McMurphy, T., Slater, A., During, M., and Cao, L. (2014) Adipose tissue insulin receptor knockdown via a new primate-derived hybrid recombinant AAV serotype. *Mol Ther Methods Clin Dev* **1**
16. Uhrig-Schmidt, S., Geiger, M., Luippold, G., Birk, G., Mennerich, D., Neubauer, H., Grimm, D., Wolfrum, C., and Kreuz, S. (2014) Gene delivery to adipose tissue using transcriptionally targeted rAAV8 vectors. *PLoS One* **9**, e116288

17. Huang, W., McMurphy, T., Liu, X., Wang, C., and Cao, L. (2016) Genetic Manipulation of Brown Fat Via Oral Administration of an Engineered Recombinant Adeno-associated Viral Serotype Vector. *Mol Ther* **24**, 1062-1069
18. Huang, W., Liu, X., Queen, N. J., and Cao, L. (2017) Targeting Visceral Fat by Intraperitoneal Delivery of Novel AAV Serotype Vector Restricting Off-Target Transduction in Liver. *Mol Ther Methods Clin Dev* **6**, 68-78
19. Jimenez, V., Jambrina, C., Casana, E., Sacristan, V., Munoz, S., Darriba, S., Rodo, J., Mallol, C., Garcia, M., Leon, X., Marco, S., Ribera, A., Elias, I., Casellas, A., Grass, I., Elias, G., Ferre, T., Motas, S., Franckhauser, S., Mulero, F., Navarro, M., Haurigot, V., Ruberte, J., and Bosch, F. (2018) FGF21 gene therapy as treatment for obesity and insulin resistance. *EMBO Mol Med* **10**
20. Huang, W., Queen, N. J., and Cao, L. (2019) rAAV-Mediated Gene Delivery to Adipose Tissue. *Methods Mol Biol* **1950**, 389-405
21. Jeevanandam, J., Barhoum, A., Chan, Y. S., Dufresne, A., and Danquah, M. K. (2018) Review on nanoparticles and nanostructured materials: history, sources, toxicity and regulations. *Beilstein J Nanotechnol* **9**, 1050-1074
22. Mitchell, M. J., Billingsley, M. M., Haley, R. M., Wechsler, M. E., Peppas, N. A., and Langer, R. (2021) Engineering precision nanoparticles for drug delivery. *Nat Rev Drug Discov* **20**, 101-124
23. Sibuyi, N. R. S., Moabelo, K. L., Meyer, M., Onani, M. O., Dube, A., and Madiehe, A. M. (2019) Nanotechnology advances towards development of targeted-treatment for obesity. *J Nanobiotechnology* **17**, 122
24. Xue, Y., Xu, X., Zhang, X. Q., Farokhzad, O. C., and Langer, R. (2016) Preventing diet-induced obesity in mice by adipose tissue transformation and angiogenesis using targeted nanoparticles. *Proc Natl Acad Sci U S A* **113**, 5552-5557
25. Jiang, C., Cano-Vega, M. A., Yue, F., Kuang, L., Narayanan, N., Uzunalli, G., Merkel, M. P., Kuang, S., and Deng, M. (2017) Dibenzazepine-Loaded Nanoparticles Induce Local Browning of White Adipose Tissue to Counteract Obesity. *Mol Ther* **25**, 1718-1729
26. Rho, J. G., Han, H. S., Han, J. H., Lee, H., Nguyen, V. Q., Lee, W. H., Kwon, S., Heo, S., Yoon, J., Shin, H. H., Lee, E. Y., Kang, H., Yang, S., Lee, E. K., Park, J. H., and Kim, W. (2018) Self-assembled hyaluronic acid nanoparticles: Implications as a nanomedicine for treatment of type 2 diabetes. *J Control Release* **279**, 89-98
27. Ma, L., Liu, T. W., Wallig, M. A., Dobrucki, I. T., Dobrucki, L. W., Nelson, E. R., Swanson, K. S., and Smith, A. M. (2016) Efficient Targeting of Adipose Tissue Macrophages in Obesity with Polysaccharide Nanocarriers. *ACS Nano* **10**, 6952-6962
28. Kolonin, M. G., Saha, P. K., Chan, L., Pasqualini, R., and Arap, W. (2004) Reversal of obesity by targeted ablation of adipose tissue. *Nat Med* **10**, 625-632
29. Hossen, M. N., Kajimoto, K., Akita, H., Hyodo, M., and Harashima, H. (2012) Vascular-targeted nanotherapy for obesity: unexpected passive targeting mechanism to obese fat for the enhancement of active drug delivery. *J Control Release* **163**, 101-110
30. Thovhogi, N., Sibuyi, N. R. S., Onani, M. O., Meyer, M., and Madiehe, A. M. (2018) Peptide-functionalized quantum dots for potential applications in the imaging and treatment of obesity. *Int J Nanomedicine* **13**, 2551-2559

31. Shin, M. D., Shukla, S., Chung, Y. H., Beiss, V., Chan, S. K., Ortega-Rivera, O. A., Wirth, D. M., Chen, A., Sack, M., Pokorski, J. K., and Steinmetz, N. F. (2020) COVID-19 vaccine development and a potential nanomaterial path forward. *Nat Nanotechnol* **15**, 646-655
32. Cullis, P. R., and Hope, M. J. (2017) Lipid Nanoparticle Systems for Enabling Gene Therapies. *Mol Ther* **25**, 1467-1475
33. Kulkarni, J. A., Myhre, J. L., Chen, S., Tam, Y. Y. C., Danescu, A., Richman, J. M., and Cullis, P. R. (2017) Design of lipid nanoparticles for in vitro and in vivo delivery of plasmid DNA. *Nanomedicine* **13**, 1377-1387
34. Hafez, I. M., Maurer, N., and Cullis, P. R. (2001) On the mechanism whereby cationic lipids promote intracellular delivery of polynucleic acids. *Gene Ther* **8**, 1188-1196
35. Yanez Arteta, M., Kjellman, T., Bartesaghi, S., Wallin, S., Wu, X., Kvist, A. J., Dabkowska, A., Szekely, N., Radulescu, A., Bergenholtz, J., and Lindfors, L. (2018) Successful reprogramming of cellular protein production through mRNA delivered by functionalized lipid nanoparticles. *Proc Natl Acad Sci U S A* **115**, E3351-E3360
36. Zhigaltsev, I. V., Belliveau, N., Hafez, I., Leung, A. K., Huft, J., Hansen, C., and Cullis, P. R. (2012) Bottom-up design and synthesis of limit size lipid nanoparticle systems with aqueous and triglyceride cores using millisecond microfluidic mixing. *Langmuir* **28**, 3633-3640
37. Belliveau, N. M., Huft, J., Lin, P. J., Chen, S., Leung, A. K., Leaver, T. J., Wild, A. W., Lee, J. B., Taylor, R. J., Tam, Y. K., Hansen, C. L., and Cullis, P. R. (2012) Microfluidic Synthesis of Highly Potent Limit-size Lipid Nanoparticles for In Vivo Delivery of siRNA. *Mol Ther Nucleic Acids* **1**, e37
38. Gary, D. J., Min, J., Kim, Y., Park, K., and Won, Y. Y. (2013) The effect of N/P ratio on the in vitro and in vivo interaction properties of PEGylated poly[2-(dimethylamino)ethyl methacrylate]-based siRNA complexes. *Macromol Biosci* **13**, 1059-1071
39. Frohlich, E. (2012) The role of surface charge in cellular uptake and cytotoxicity of medical nanoparticles. *Int J Nanomedicine* **7**, 5577-5591
40. Burchard, W., and Richtering, W. (1989) Dynamic Light-Scattering from Polymer-Solutions. *Prog Coll Pol Sci S* **80**, 151-163
41. Maeda, H., Wu, J., Sawa, T., Matsumura, Y., and Hori, K. (2000) Tumor vascular permeability and the EPR effect in macromolecular therapeutics: a review. *J Control Release* **65**, 271-284
42. Pardi, N., Tuyishime, S., Muramatsu, H., Kariko, K., Mui, B. L., Tam, Y. K., Madden, T. D., Hope, M. J., and Weissman, D. (2015) Expression kinetics of nucleoside-modified mRNA delivered in lipid nanoparticles to mice by various routes. *J Control Release* **217**, 345-351
43. Reichmuth, A. M., Oberli, M. A., Jaklenec, A., Langer, R., and Blankschtein, D. (2016) mRNA vaccine delivery using lipid nanoparticles. *Ther Deliv* **7**, 319-334
44. Nie, S. (2010) Understanding and overcoming major barriers in cancer nanomedicine. *Nanomedicine (Lond)* **5**, 523-528

45. Gessner, A., Lieske, A., Paulke, B., and Muller, R. (2002) Influence of surface charge density on protein adsorption on polymeric nanoparticles: analysis by two-dimensional electrophoresis. *Eur J Pharm Biopharm* **54**, 165-170
46. Vonarbourg, A., Passirani, C., Saulnier, P., and Benoit, J. P. (2006) Parameters influencing the stealthiness of colloidal drug delivery systems. *Biomaterials* **27**, 4356-4373
47. Lundqvist, M., Stigler, J., Elia, G., Lynch, I., Cedervall, T., and Dawson, K. A. (2008) Nanoparticle size and surface properties determine the protein corona with possible implications for biological impacts. *Proc Natl Acad Sci U S A* **105**, 14265-14270
48. Muzumdar, M. D., Tasic, B., Miyamichi, K., Li, L., and Luo, L. (2007) A global double-fluorescent Cre reporter mouse. *Genesis* **45**, 593-605
49. Balkow, A., Hoffmann, L. S., Klepac, K., Glode, A., Gnad, T., Zimmermann, K., and Pfeifer, A. (2016) Direct lentivirus injection for fast and efficient gene transfer into brown and beige adipose tissue. *J Biol Methods* **3**, e48
50. Cannon, B., and Nedergaard, J. (2004) Brown adipose tissue: function and physiological significance. *Physiol Rev* **84**, 277-359
51. Cypess, A. M., Lehman, S., Williams, G., Tal, I., Rodman, D., Goldfine, A. B., Kuo, F. C., Palmer, E. L., Tseng, Y. H., Doria, A., Kolodny, G. M., and Kahn, C. R. (2009) Identification and importance of brown adipose tissue in adult humans. *N Engl J Med* **360**, 1509-1517
52. Villarroya, F., Cereijo, R., Villarroya, J., and Giralt, M. (2017) Brown adipose tissue as a secretory organ. *Nat Rev Endocrinol* **13**, 26-35
53. Lin, J., Zhou, Y., Liu, J., Chen, J., Chen, W., Zhao, S., Wu, Z., and Wu, N. (2017) Progress and Application of CRISPR/Cas Technology in Biological and Biomedical Investigation. *J Cell Biochem* **118**, 3061-3071
54. Zafra, M. P., and Dow, L. E. (2016) Somatic Genome Editing Goes Viral. *Trends Mol Med* **22**, 831-833
55. Leung, A. K., Hafez, I. M., Baoukina, S., Belliveau, N. M., Zhigaltsev, I. V., Afshinmanesh, E., Tieleman, D. P., Hansen, C. L., Hope, M. J., and Cullis, P. R. (2012) Lipid Nanoparticles Containing siRNA Synthesized by Microfluidic Mixing Exhibit an Electron-Dense Nanostructured Core. *J Phys Chem C Nanomater Interfaces* **116**, 18440-18450
56. Thomas, A., S, M. G., De Souza, R. A. G., Ouellet, E., Tharmarajah, G., Reichert, D., Ordobadi, M., Ip, S., and Ramsay, E. C. (2018) Microfluidic Production and Application of Lipid Nanoparticles for Nucleic Acid Transfection. *Methods Mol Biol* **1792**, 193-203
57. Mohamed, M., Abu Lila, A. S., Shimizu, T., Alaaeldin, E., Hussein, A., Sarhan, H. A., Szebeni, J., and Ishida, T. (2019) PEGylated liposomes: immunological responses. *Sci Technol Adv Mater* **20**, 710-724
58. Kulkarni, J. A., Darjuan, M. M., Mercer, J. E., Chen, S., van der Meel, R., Thewalt, J. L., Tam, Y. Y. C., and Cullis, P. R. (2018) On the Formation and Morphology of Lipid Nanoparticles Containing Ionizable Cationic Lipids and siRNA. *ACS Nano* **12**, 4787-4795
59. Jayaraman, M., Ansell, S. M., Mui, B. L., Tam, Y. K., Chen, J., Du, X., Butler, D., Eltepu, L., Matsuda, S., Narayanannair, J. K., Rajeev, K. G., Hafez, I. M., Akinc,

A., Maier, M. A., Tracy, M. A., Cullis, P. R., Madden, T. D., Manoharan, M., and Hope, M. J. (2012) Maximizing the potency of siRNA lipid nanoparticles for hepatic gene silencing in vivo. *Angew Chem Int Ed Engl* **51**, 8529-8533

60. Bailey, A. L., and Cullis, P. R. (1994) Modulation of membrane fusion by asymmetric transbilayer distributions of amino lipids. *Biochemistry* **33**, 12573-12580
61. Heyes, J., Palmer, L., Bremner, K., and MacLachlan, I. (2005) Cationic lipid saturation influences intracellular delivery of encapsulated nucleic acids. *J Control Release* **107**, 276-287
62. Li, S. D., and Huang, L. (2009) Nanoparticles evading the reticuloendothelial system: role of the supported bilayer. *Biochim Biophys Acta* **1788**, 2259-2266
63. Whitehead, K. A., Matthews, J., Chang, P. H., Niroui, F., Dorkin, J. R., Severgnini, M., and Anderson, D. G. (2012) In vitro-in vivo translation of lipid nanoparticles for hepatocellular siRNA delivery. *ACS Nano* **6**, 6922-6929
64. Platt, R. J., Chen, S., Zhou, Y., Yim, M. J., Swiech, L., Kempton, H. R., Dahlman, J. E., Parnas, O., Eisenhaure, T. M., Jovanovic, M., Graham, D. B., Jhunjhunwala, S., Heidenreich, M., Xavier, R. J., Langer, R., Anderson, D. G., Hacohen, N., Regev, A., Feng, G., Sharp, P. A., and Zhang, F. (2014) CRISPR-Cas9 knockin mice for genome editing and cancer modeling. *Cell* **159**, 440-455

CHAPTER III

BAd-CRISPR: Inducible Gene Knockout in Brown Adipose Tissue of Adult Mice

Adapted from:

Romanelli, S.M., Nishii, A., Lewis, K.T., Rupp, A.C., Li, Z., Mori, H., Schill, R.L., Learman, B.S., Rhodes, C.J., and MacDougald, O.A. (2021). BAd-CRISPR: inducible gene knockout in brown adipose tissue of adult mice. *In Press*.

ABSTRACT

CRISPR/Cas9 has enabled inducible gene knockout in numerous tissues, however, its use has not been reported in brown adipose tissue (BAT). Therefore, we developed the brown adipocyte CRISPR (BAd-CRISPR) methodology in which an adeno-associated virus (AAV8) is used to administer a single guide RNA (sgRNA) directly to BAT of mice expressing Cas9 in brown adipocytes to enable rapid interrogation of one or multiple genes and streamline the paths to discovery compared to traditional transgenic approaches. We show that local administration of AAV8-sgRNA to the interscapular BAT of adult mice robustly transduces brown adipocytes and ablates expression of adiponectin (ADIPOQ), adipose triglyceride lipase (ATGL), fatty acid synthase (FASN), perilipin 1 (PLIN1), and stearoyl-CoA desaturase 1 (SCD1) by >90%. BAd-CRISPR induced frameshift mutations and suppressed target gene mRNA expression but did not lead to substantial accumulation of off-target mutations in BAT. We used BAd-CRISPR to create an inducible uncoupling protein 1 (UCP1) knockout mouse to assess effects of UCP1 loss on adaptive thermogenesis in adult mice. Interestingly, inducible UCP1 knockout did not impair adaptive thermogenesis when adult mice were housed at 5ºC. BAd-CRISPR Ucp1 mice had elevated circulating concentrations of fibroblast growth factor 21 (FGF21) and changes in BAT gene expression consistent with an increase in heat-producing peroxisomal lipid oxidation at the expense of mitochondrial metabolism, and energy wasting via an increase in both protein synthesis and turnover. Thus, we show that BAd-CRISPR is an efficient tool to speed discoveries in adipose tissue biology.

INTRODUCTION

Adipose tissues play important physiological roles in the maintenance of whole-body energy homeostasis and metabolism. Beyond simply storing excess energy in the form of triacylglycerols, adipose tissues are found throughout the body in distinct depots, each with unique functions. Classically, adipose tissues are classified as white (WAT), which are found in subcutaneous and visceral depots, or brown (BAT), which are found in the interscapular, periaortic, perirenal, and intercostal depots (1,2). Beige/BRITE adipocytes, a distinct adipocyte population induced with cold exposure and adrenergic agonists, are found within some WAT depots (3). Adipose tissue is also located in more specialized areas such as the bone marrow, intramuscular, periarticular, pericardial, epicardial, retro-orbital, and dermal depots (1,4,5). Collectively, these tissues comprise the largest endocrine organ in the body and regulate satiety, carbohydrate and lipid metabolism, bone homeostasis, blood pressure, and the immune response (6,7). Thus, understanding these dynamic adipose tissues is integral to our understanding of their roles in metabolic disorders such as obesity or lipodystrophy (8).

Our understanding of adipose tissues has fundamentally relied upon the use of transgenic mouse models. Conditional models using the Cre/LoxP system have enabled tissue-specific knockout to study a gene of interest. Several Cre-recombinase lines have been developed in which Cre expression is driven by promoters/enhancers for *Adipoq*, *Fabp4, PdgfRα*, *Prx1*, or *Ucp1* (9-11). Additionally, inducible transgenic models including Adipoq-Cre^{ERT}, Ucp1-Cre^{ERT}, and “AdipoChaser” have afforded control over the timing of gene knockout (9,10,12,13). Whilst these transgenic mouse models have undoubtedly led to advances in adipose tissue research, they are not without limitations. For example, Adipoq-Cre causes recombination in some osteoblasts, whereas Fabp4-Cre causes widespread recombination due to expression early in development (9,11,14,15). Moreover, tamoxifen administration to Cre^{ERT} mice has been shown to decrease adipose mass, particularly when combined with gene knockout (16). Cre expression can also change generation-to-generation in mouse colonies (14). Another critical limitation is that Cre mice must be bred to mice harboring a floxed allele, which in certain circumstances, necessitates the generation of a new mouse strain. Generating a novel transgenic strain

can require labs to commit years and significant investment to developing and breeding before performing any experiments (17). Therefore, more efficient strategies are required to improve how adipose tissues are studied *in vivo*.

An efficient strategy to modulate gene expression *in vivo* has centered upon the use of CRISPR/Cas9 delivery for inducible knockout in somatic tissues. CRISPR/Cas9 is comprised of the Cas9 endonuclease, which creates double-strand DNA breaks, and a single guide RNA (sgRNA), which is a programmable RNA molecule that directs Cas9 to its target site for mutagenesis (18). Both the Cas9 endonuclease and a sgRNA can therefore be genetically encoded and packaged into a virus for somatic knockout in adult tissues (17). Viral delivery of the CRISPR/Cas9 machinery for inducible knockout offers several advantages over conventional germline knockouts as the timing, tissue, and target can be closely controlled (17). Moreover, embryonically lethal genes can be studied in this context. Several iterations of viral CRISPR/Cas9 delivery have been developed (19). For example, both Cas9 and sgRNA have been packaged into viral vectors and administered to the lung epithelium, liver, and hippocampus (20-22). Additionally, transgenic approaches have created inducible- and tissue-specific Cas9-expressing mouse models to which sgRNAs are delivered using adeno-associated viruses (AAVs) (19). Platt et al. developed the Cre-dependent Cas9 knockin mouse which when bred to a tissue-specific promoter-driven Cre, enables somatic genome editing in adult tissues (23). As proof of concept, AAVs encoding a sgRNA to *Kras*, *p53*, or *Lkb1* were delivered to the lung to accurately model adenocarcinoma disease progression. This Cas9 model has been further adapted for inducible somatic gene knockout in heart, skin, intestine, and thymus, thereby demonstrating its broad versatility across different tissues (24,25).

Whereas AAV-mediated CRISPR/Cas9 gene transfer has proven useful for modeling disease in numerous tissues, its use in adipose tissues has not been reported. This is largely due to the fact that adipose tissues are located throughout the body in distinct locations, making transduction difficult (26-28). Moreover, mature adipocytes only comprise 11-40% of the total cell population of adipose tissues and lack unique cell surface receptors, which makes it challenging for a vector to navigate specifically to the adipocytes (26-28). Currently, CRISPR/Cas9 has only been accomplished in preadipocyte culture models. For example, Shen and colleagues transduced primary

preadipocytes using a nonviral vector to administer CRISPR/Cas9 and disrupt expression of the *Nrip1* gene (29). In another study, Kamble et al. electroporated CRISPR/Cas9 into human preadipocytes and demonstrated efficient knockout of *Pparg* and *Fkbp5* (30). Yet while these studies show that CRISPR/Cas9 can function in preadipocyte models, the field has yet to unlock the full potential of CRISPR/Cas9 for somatic gene editing *in vivo*. Thus, we developed a method for CRISPR/Cas9 inducible gene knockout in adipose tissues. We optimized this method for knocking out genes in BAT, as it is found predominantly in the interscapular depot in rodents and is easily accessible. BAT is the main site of adaptive thermogenesis and uncouples oxidative phosphorylation to generate heat in response to cold stress (31). BAT also has important endocrine functions, secreting molecules required for the thermogenic response that stimulate hypertrophy, vascularization, innervation, and blood flow to BAT (32). In humans, active BAT is inversely associated with body mass index, making it a potentially attractive candidate for combatting obesity (33).

Herein we report that CRISPR/Cas9 can induce gene knockout in BAT. Our methodology, termed brown adipocyte CRISPR (BAd-CRISPR), integrates viral delivery with the established Cre/LoxP approach to significantly decrease the time and investment required to knockout genes in BAT of adult mice. We accomplished this by administering AAV8-sgRNA to brown adipocyte-specific Cas9 expressing mice. BAd-CRISPR efficiently targeted *Adipoq*, *Atgl*, *Fasn*, *Plin1*, *Scd1*, and *Ucp1* in BAT, decreasing expression by 80-99%. We also showed that BAd-CRISPR inducible gene knockout recapitulates previously reported phenotypes for ATGL and PLIN1 knockout mice. Importantly, we show that BAd-CRISPR streamlines the path to generation of transgenic mice and affords the ability to target multiple genes in BAT simultaneously. Lastly, we used BAd-CRISPR to create inducible UCP1 knockout mice and found that loss of UCP1 expression in adult mice did not impair adaptive thermogenesis when mice were cold stressed at 5ºC. Interestingly, we observed an increase in *Fgf21* expression in BAT as well as dramatic changes to the transcriptome predicted to increase heat production through peroxisomal lipid oxidation and futile cycling through elevated protein synthesis and degradation. Thus, BAd-CRISPR serves as a more efficient alternative approach to generate BAT-specific knockouts and affords the ability to study gene function in adult mice.

RESULTS

Transfection of adipocyte precursors with sgRNAs predominantly causes frameshift mutations in the target gene

To induce gene knockout in adult mice, we devised the BAd-CRISPR method, in which AAV-sgRNAs are administered to mice expressing Cas9. We created a cloning strategy that facilitates incorporation of a U6 promoter-driven sgRNA into an AAV expression vector (**Supplement 3.1a**). The AAV expression vector also contains a CMV-driven mCherry fluorescent marker and 5' and 3' inverted terminal repeats (**Figure 3.1a**). We designed sgRNAs using the CRISPOR design tool and selected sgRNAs that targeted early coding regions, lacked 0- or 1-base mismatch off-target sites, and had high Cutting Frequency Determination (CFD) scores (34). The CFD score, developed by Doench and Fusi, calculates the off-target potential of a sgRNA by considering the position and identities of mismatched nucleotides in the sgRNA sequence (35). As a general rule, sgRNAs should have a CFD score ≥0.2 (35). All of the sgRNAs designed had a CFD score >0.4 (**Supplement 3.1b**).

To test each sgRNA, AAV expression vectors were transfected into primary adipocyte progenitor cells isolated from Rosa26-Cas9 knockin mice (23). Transfected cells were sorted for mCherry expression using flow cytometry and DNA was analyzed by Sanger sequencing. Primers flanking sgRNA cut sites were used to sequence *Adipoq*, *Atgl*, and *Plin1*, and traces were analyzed using the Tracking of Indels by Decomposition (TIDE) and Synthego ICE Analysis tools (36). Corresponding sgRNA efficiencies were observed in both the forward (data not shown) and reverse sequence traces (**Figure 3.1b-d**). Synthego ICE analysis identified 1-base deletions as the predominant indel contribution across all sgRNAs tested. To calculate the total mutations resulting in a frameshift, we divided the number of frameshift mutations by the total number of predicted mutations. Frameshift mutations accounted for 97.5%, 92.5%, and 95.5% of the total mutations for sgRNAs targeting *Adipoq*, *Atgl*, and *Plin1*, respectively (**Figure 3.1b-d**). Analyzing CRISPR/Cas9-induced mutations using decomposition of Sanger sequence traces is an easy to use and cost-effective method for assessing a small number of samples (37). TIDE and next generation sequencing analyses have been shown to be

highly correlated; however, frequencies calculated using TIDE often underrepresent the true editing efficiency when compared to next generation sequencing (38). Thus, the true editing efficiency for each sgRNA is likely higher. After validating sgRNA efficiencies *in vitro*, AAV expression vectors were used to generate AAVs encoding the sgRNA and mCherry fluorescent marker. For transducing adipose tissues, AAV serotype 8 (AAV8) has been used most extensively owing to its favorable tropism for brown and white adipocytes (26-28,39-44).

BAd-CRISPR mice express Cas9 exclusively in BAT

Although AAV8 is the gold standard for transducing adipose tissues, its relatively small genome size (~4.7 kb) limits packaging *S. pyogenes* Cas9 with the sgRNA and mCherry transgene (26-28). Therefore, we developed a mouse line that expresses Cas9 specifically in brown adipocytes (BAd-CRISPR) by breeding two existing mouse lines: *Ucp1* promoter-Cre recombinase (B6.FVB-Tg(Ucp1-cre)1Evdr/J) and Cre-dependent Cas9-GFP (Rosa26-LSL-Cas9) (**Supplement 3.2a**) (10,23). As expected, Cas9 is detected by immunoblot analyses in lysates from BAT of BAd-CRISPR mice but not from posterior subcutaneous WAT (psWAT), parametrial WAT (pmWAT), or liver, nor is it found in any tissues in mice lacking Ucp1-Cre expression (**Supplement 3.2b**). Confocal microscopy of freshly dissected tissues showed Cas9-GFP expression exclusively in BAT but not in psWAT, pmWAT, nor liver (**Supplement 3.2c**). Thus, these mice are a suitable model to assess the effectiveness of CRISPR/Cas9 for inducible gene knockout in brown adipocytes.

Local injection of AAV8-mCherry to the interscapular BAT robustly transduces BAT with minimal leak to other tissues

Next, we optimized a delivery strategy using AAV8 to administer sgRNAs for BAd-CRISPR inducible gene knockout. Initially, we attempted tail vein injection as well as intraperitoneal injection of 100 µL 10^{12} vg/mL AAV8-mCherry to transduce all adipose tissues, both of which were unsuccessful and led to substantial transduction of liver (data not shown). By contrast, direct injection of AAV8 into an adipose tissue has been shown to significantly improve transduction efficiency and reduce vector accumulation in liver,

heart, and lung (26-28,39). To test this, we directly injected 100 µL 10^{12} vg/mL AAV8-mCherry into interscapular BAT or psWAT and sacrificed mice after 14 days in accordance with previously established protocols (39,45). Although direct injection into psWAT transduced only a minority of white adipocytes (data not shown), direct injection to interscapular BAT showed widespread and robust mCherry expression throughout BAT (**Supplement 3.3a-b**). With direct injection to BAT, a small number of cells in liver were also mCherry positive but mCherry signal was not observed in WAT depots examined (**Supplement 3.3a-b**). Using quantitative PCR (qPCR), we found that *mCherry* mRNA expression was enriched in the interscapular BAT following local injection, with small or undetectable expression in psWAT, pmWAT, liver, spleen, heart, lung, or kidney (**Supplement 3.3b**).

BAd-CRISPR induces knockout of Adipoq, ATGL, FASN, PLIN1, and SCD1 in brown adipocytes of adult mice

After validating robust BAT transduction using AAV8 direct injection, we next sought to apply the BAd-CRISPR method for inducible gene knockout. We targeted genes highly expressed in brown adipocytes and administered 100 µL 10^{12} vg/mL AAV8-sgRNAs targeting *Adipoq*, *Atgl*, *Fasn*, *Plin1*, *Scd1*, or a Control sgRNA, directly into the interscapular BAT of BAd-CRISPR mice (n = 3 or 4 mice). BAd-CRISPR mice were sacrificed 14 days post-injection and BAT was homogenized to isolate mRNA and protein. Impressively, mRNA and protein expression for each target were reduced by 80-99% (**Figure 3.2a-e**). It should be noted, that despite performing a thorough transcardial perfusion, we detected albumin in BAT homogenate (data not shown), suggesting that blood was not completely cleared from the tissue. Thus, cellular ADIPOQ protein levels are likely reduced more than what is observed in the immunoblot (**Figure 3.2a**). To further assess AAV8 transduction efficiency in BAT, we performed immunofluorescence for ATGL expression in BAd-CRISPR Atgl mice (**Figure 3.2f**). ATGL was only detected in a few brown adipocytes (white arrows), indicating that direct injection of AAV8 transduces the vast majority of brown adipocytes, and that expression of sgRNA efficiently targets ATGL expression.

BAd-CRISPR Atgl, BAd-CRISPR Plin1, and BAd-CRISPR Fasn inducible knockouts recapitulate previously described BAT phenotypes

To investigate whether BAd-CRISPR can be used to recapitulate known knockout phenotypes in BAT, we further characterized BAd-CRISPR Atgl, BAd-CRISPR Plin1, and BAd-CRISPR Fasn inducible knockouts described in **Figure 3.2** and compared our results to phenotypes identified using traditional transgenic approaches (46-50). BAd-CRISPR Atgl inducible knockout caused significant BAT hypertrophy compared to BAd-CRISPR Control mice and histological sectioning revealed a striking whitening of BAT (**Figure 3.3a-b**). These results mirror the observed phenotypes reported using the global and BAT-specific inducible ATGL knockout mice, which also have marked hypertrophy and whitening (46,47). By contrast, BAd-CRISPR Plin1 inducible knockout led to a decrease in BAT weight coupled with the loss of multilocular brown adipocyte morphology and the emergence of distinct, but rare unilocular lipid droplets dispersed throughout BAT (**Figure 3.3a-b**). These data bear similarity to the global PLIN1 knockout mouse models, which had smaller or complete loss of lipid droplets in BAT (48,49). Interestingly, BAT weight was not altered in the two reported PLIN1 knockout models (48,49). This difference may be explained by the fact that in the BAd-CRISPR inducible knockout model, mice lose PLIN1 expression as adults compared to the global knockout mice that lack PLIN1 from birth. Second, both reported PLIN1 knockout models are whole-body deletion, whereas BAd-CRISPR Plin1 inducible knockout is brown adipocyte specific. Lastly, BAd-CRISPR Fasn mice showed a decrease in total lipid droplet size and BAT tissue weight relative to BAd-CRISPR Control mice (**Figure 3.3a-b**). These data replicate the phenotype observed in the brown adipocyte Ucp1-Cre FASN$^{flox/flox}$ mice, which had a reduction in lipid droplet size (50). Thus, our method can be used to inducibly knockout genes of interest in brown adipocytes of adult mice, and we have validated its effects on several genes by phenocopying previous loss of function models.

BAd-CRISPR enables simultaneous knockout of ATGL and PLIN1 in brown adipocytes

To test whether BAd-CRISPR can be used to knockout multiple genes in BAT concurrently, we targeted *Atgl* and *Plin1* using two separate AAV8 vectors. We chose *Atgl*

and *Plin1* as targets because they have opposing functions; ATGL hydrolyzes triacylglycerols whereas PLIN1 protects against this hydrolysis (51,52). Moreover, it has been established that ATGL knockout in BAT causes hypertrophy and whitening whereas PLIN1 knockout in BAT decreases tissue size and causes a darker morphology, therefore we would have a visual phenotype with which to evaluate the feasibility of a double knockout (**Figure 3.3a-b**) (46-49). BAd-CRISPR mice and Rosa26-LSL-Cas9 mice lacking functional Cas9 (BAd-CRISPR Control) were administered 100 µL 10^{10} vg/mL AAV8-sgRNA targeting *Atgl* alone, *Plin1* alone, or *Atgl* and *Plin1* in combination. BAd-CRISPR Atgl mice had profound whitening and BAT hypertrophy whereas BAd-CRISPR Plin1 mice had a darker BAT morphology and decreased tissue size (**Figure 3.4a-c**). By contrast, BAd-CRISPR Atgl + Plin1 mice displayed a "hybrid" morphology characterized by a mild increase in BAT weight compared to BAd-CRISPR Control mice, which were also administered both sgRNAs but lacked Cas9 expression (**Figure 3.4a-c**). Collectively, these data demonstrate that BAd-CRISPR is scalable for inducible knockout of multiple genes in brown adipocytes.

BAd-CRISPR ablates UCP1 expression in brown adipose tissue

The *Ucp*1 knockout mouse has been extensively studied since the mice were first generated by Enerbäck and colleagues in 1997 (53). Thus, it is well known that UCP1-deficient mice (Ucp1-/-) rely on compensatory mechanisms such as increased shivering, activation of futile cycles, or recruitment of beige/BRITE adipocytes to maintain body temperature when cold stressed (54). These adaptations allow Ucp1-/- mice to tolerate a stepwise reduction in ambient temperature from thermoneutrality (~30ºC) to extreme cold (-10ºC), however, immediate cold exposure at 4ºC can prove lethal for mice lacking functional UCP1 (54-57). After canvassing the literature, we were intrigued to find that whilst a plethora of papers have reported on the consequences of constitutive global UCP1 knockout, no studies have reported the effect of inducible UCP1 knockout on adaptive thermogenesis in adult mice. Thus, we sought to characterize inducible UCP1 knockout using BAd-CRISPR.

To show that BAd-CRISPR could be used to inducibly knockout UCP1 in adult mice, we administered 100 µL 10^{12} vg/mL AAV8-UCP1 sgRNA directly into interscapular

BAT. Mice were sacrificed at 0 (no virus), 2, 7, or 14 days post-injection to assess degree of knockout (n = 3 mice per timepoint). As expected, confocal microscopy of freshly dissected tissue at 14 days revealed robust mCherry expression in BAT, with no mCherry detected in psWAT or pmWAT, and a low signal detected in liver compared to BAT (**Figure 3.5a**). Importantly, Cas9-GFP expression was exclusive to BAT and was not detected in any other tissues examined (**Figure 3.5a**). We also observed an increase in *mCherry* mRNA expression between 0 and 14 days (**Figure 3.5b**). To assess for mutations in BAd-CRISPR Ucp1 mice, we performed a genomic cleavage assay on cDNA since *Ucp1* mRNA is expressed specifically in brown adipocytes (**Figure 3.5c**). We observed aberrant PCR product bands at 7 and 14 days post injection but only the WT band at 0 and 2 days (**Figure 3.5c**). Interestingly, we observed multiple PCR products with or without addition of T7 endonuclease at 7 and 14 days, suggesting amplification of mutations causing substantial deletions at the target site. To further confirm mutations, we performed Sanger sequencing on cDNA at the *Ucp1* sgRNA cut site and observed aberrant traces in mice at 14 days (**Figure 3.5d**). Impressively, *Ucp1* mRNA expression was decreased by ~90% 2-days post injection and by ~99% at 7 and 14 days (**Figure 3.5e**). These results were further confirmed by immunoblot analyses, which showed a dramatic reduction in UCP1 protein expression at 7 days and near total loss by 14 days without loss of ADIPOQ expression (**Figure 3.5f**). Increased lipid accumulation, observed as a whitening of BAT on histological evaluation, has been reported previously for Ucp1-/- mice, and we also observe a slight whitening in histological sections of BAT at 2, 7, and 14 days post-injection, relative to mice that were not administered AAV8-UCP1 sgRNA (day 0) (**Supplement 3.4a**) (53). UCP1 protein turnover in the basal state occurs by ~4 days and parallels the proteolytic rates of other mitochondrial proteins (58,59).

To show that BAd-CRISPR Ucp1 inducible knockout occurs as a result of CRISPR/Cas9 mutagenesis, we administered AAV8-UCP1 sgRNA to Rosa26-LSL-Cas9 mice that were bred to Ucp1-Cre mice (Ucp1-Cre^{+}) or not (Ucp1-Cre^{-}). UCP1 knockout occurred only when Rosa26-LSL-Cas9 mice were bred to the Ucp1-Cre background and therefore had functional Cas9 expression (**Supplement 3.4b-c**). We also showed that UCP1 knockout only occurs when BAd-CRISPR mice are administered AAV8-UCP1 sgRNA and not when administered AAV8-Control sgRNA (**Supplement 3.4d-e**). To

quantify transduction efficiency, we performed immunofluorescent analyses on fixed BAT from BAd-CRISPR Ucp1 or BAd-CRISPR Control mice. BAd-CRISPR Ucp1 caused a near total loss of UCP1 expression in brown adipocytes, suggesting that viral transduction is nearly 100% (**Supplement 3.4f**). We did observe very few UCP1 positive cells dispersed throughout BAT (**Supplement 3.4f**). It should be noted that the anti-UCP1 antibody cross-reacted with endomucin positive cells of the vasculature, however, there is a clear difference in UCP1 expression between BAd-CRISPR Control and BAd-CRISPR Ucp1 mice (**Supplement 3.4f**). Collectively, these data provide strong evidence that CRISPR/Cas9 induces knockout of *Ucp1* in brown adipocytes of adult mice *in vivo*.

BAd-CRISPR Ucp1 inducible knockout mice defend core body temperature and have elevated FGF21

Next, we used BAd-CRISPR Ucp1 mice to determine if adult mice could maintain body temperature when cold stressed at 5ºC following inducible UCP1 knockout in BAT. Female 8-10 week old mice were implanted with an intraperitoneal telemeter to monitor core body temperature one-week prior to AAV8 administration. All mice were single housed at room temperature (20-21ºC) and nest building materials were withheld throughout the study. We administered 100 µL 10^{12} vg/mL AAV8-UCP1 sgRNA or AAV8-Control sgRNA to the interscapular BAT (n = 4 or 5 mice) and mice were allowed to recover for 14 days (**Figure 3.6a**). Mice were then cold stressed at 5ºC for 24 hours. BAd-CRISPR induced complete loss of UCP1 expression at both the mRNA and protein levels (**Figure 3.6b-c**). Despite an apparent total knockout of UCP1 in BAT, there was no difference in body temperature when mice were housed at room temperature (20-21ºC) or cold stressed (5ºC) (**Figure 3.6d-e, Supplement 3.5a**). The same is true for the aforementioned Ucp1-/- mice, which, when pre-acclimated to mild cold stress, are cold tolerant (57). We did not observe changes to body weight, BAT weight, or average daily food intake between BAd-CRISPR Control and BAd-CRISPR Ucp1 mice (**Supplement 3.5b-d**). Moreover, UCP1 protein expression was undetected in inguinal WAT in these mice, suggesting that thermogenic mechanisms besides beige/BRITE adipogenesis are operative in BAd-CRISPR Ucp1 mice (**Supplement 3.5e**). Interestingly, we did observe a significant increase in *Fgf21* expression in BAT (**Figure 3.6f**). It has been reported that

circulating FGF21 is increased in response to cold stress as a compensatory mechanism for adaptive thermogenesis (32,60,61). Thus, we repeated this experiment using BAd-CRISPR Ucp1 inducible knockout mice, Ucp1-/- mice, and Rosa26-LSL-Cas9 (BAd-CRISPR Control) mice. Interestingly, we observed an "intermediate" increase in serum FGF21 levels in BAd-CRISPR Ucp1 inducible knockout mice compared to Ucp1-/- and BAd-CRISPR Control mice after being cold stressed at 5ºC for 24 hours (**Figure 3.6g**). These data further support the role of FGF21 in adaptive thermogenesis (32,60,61).

Gene profiling of BAT from BAd-CRISPR Ucp1 mice suggests peroxisomal lipid oxidation and increased protein synthesis/turnover as a compensatory thermogenic process

Thermoneutrality in mice is approximately 30ºC whereas mice are typically housed between 20-22ºC and are therefore under a chronic mild cold stress (62,63). To explore potential mechanisms by which BAd-CRISPR Ucp1 mice adapt to a mild cold stress in the absence of UCP1, we performed RNA sequencing (RNAseq) on BAT from mice administered 100 µL 10^{12} vg/mL AAV8-UCP1 sgRNA or AAV8-Control sgRNA. Of the >20,000 genes identified from RNAseq, 1,056 were found to be differentially expressed. As expected, the most statistically significant difference was the ~90% suppression of *Ucp1* mRNA in BAT of BAd-CRISPR Ucp1 mice (**Figure 3.7a**). We then used gene set enrichment analysis (GSEA) to identify significantly up- and down-regulated pathways in response to inducible UCP1 knockout. GSEA indicated up-regulation of pathways involved in fatty acid metabolism, the peroxisome, unfolded protein response, protein secretion, and mTORC signaling (**Figure 3.7b**). Pathways related to the mitochondrial electron transport chain and heat production by uncoupling proteins were down-regulated, as was the citric acid cycle (**Figure 3.7b**). Next, we mined GSEA pathways for genes that were significantly up- or down-regulated. We clustered genes based on pathways to generate a heat map and found that BAd-CRISPR Ucp1 inducible knockout mice have elevation of peroxisome and lipid metabolism genes, which strongly suggests reliance on peroxisomal β-oxidation of fatty acids to generate heat (**Figure 3.7c**) (64). We also observed a down-regulation of mitochondrial genes, particularly those involved in the electron transport chain and coupled respiration (*mt-Nd1*, *mt-Nd3*, *mt-Nd4*, *mt-Nd6*, *mt-*

Co1, and *mt-Atp6*) (**Figure 3.7c**). Interestingly, we observed elevated expression of tRNA synthetase genes– *Cars*, *Nars*, *Yars*, *Wars*, *Tars*, *Sars*, *Gars*, *Iars*, and *Eprs*– which is predicted to increase the rate of translation (65,66). We also see up-regulation of many genes coding for subunits of the proteasome, suggesting a futile cycle involving both increased synthesis and turnover of proteins (**Figure 3.7c**). These data may also indicate dynamic *de novo* synthesis of proteins required for adaptive thermogenesis as well as for protection against cellular stress in BAd-CRISPR Ucp1 mice (67,68). Lastly, we compared differentially expressed genes in BAd-CRISPR Ucp1 mice to Ucp1-/- mice on a normal chow diet at 20ºC (**Figure 3.7d**) (69). In total, 256 genes were found to overlap. Interestingly, these overlapping genes cluster to pathways involved in the peroxisome, lipid metabolism, and the proteasome, further supporting a compensatory mechanism for maintaining adaptive thermogenesis.

CRISPR/Cas9 does not lead to observable off-target mutations in BAT of BAd-CRISPR Ucp1 mice

CRISPR/Cas9 mutagenesis has been shown to have off-target effects at loci that bear similarity to the sgRNA sequence (70). These off-target mutations can impact genome integrity and cause unwanted phenotypic changes that obscure results. Using CRISPOR and the Synthego CRISPR Design tool, we identified 7 off-target loci for the *Ucp1* sgRNA (**Figure 3.8a**). Off-target loci had 3 or 4-base mismatches; no off-targets contained fewer than 3 base mismatches. We focused on the highest predicted off-target identified by both tools–which occurred in an intergenic space on chromosome 18– in addition to off-target sites that were found within exons or introns of genes (**Figure 3.8a**). To check for mutations at off-target sites, we performed unbiased whole genome sequencing on BAT from two BAd-CRISPR Ucp1 mice. Whole genome sequencing data was analyzed using the Integrative Genome Viewer (IGV) and CRISPResso2 (71,72). We observed mutations in 36.1% of reads on average at the *Ucp1* locus compared to 1.8% at the intergenic space and 0.0% at all other sites, respectively (**Figure 3.8a**). To probe the intergenic off-target in more detail, we analyzed whole genome sequencing data from both BAd-CRISPR Ucp1 mice using CRISPResso2 and found a single substitution at position 1 of the sgRNA sequence in 1 out of 51 total reads at this locus (**Figure 3.8b**). CRISPResso2 did not

identify any insertions or deletions in reads at this off-target site. Next, we performed a genomic cleavage assay on genomic DNA from BAd-CRISPR Ucp1 mice sacrificed at different timepoints and did not observe aberrant mutant PCR or T7 cleavage products at the intergenic off-target site (**Figure 3.8c**). Therefore, mutations at this off-target site are likely very rare or are background mutations in this mouse line that are different from the reference. Additionally, we probed RNAseq data from BAd-CRISPR Ucp1 mice to determine if gene expression at the coding regions was disrupted. We did not observe any indication that gene expression was altered at off-target loci (**Figure 3.8d**). Although one off-target site located within an intron of *Rftn1* had decreased mRNA expression in the BAd-CRISPR Ucp1 mice, this locus has three mismatches proximal to the PAM and we did not detect mutations in whole genome sequencing data (**Figure 3.8a, 3.8d**). Thus, it is likely that reduction in *Rftn1* expression is secondary to UCP1-knockout rather than the result of off-target mutagenesis. Taken together, these data suggest that BAd-CRISPR knockout does not lead to substantial off-target mutations.

DISCUSSION

Although viral CRISPR/Cas9 delivery has proved a powerful tool for manipulating the somatic genome in liver, lung, heart, skeletal muscle, small intestine, thymus, and the central nervous system, it has not been reported in white or brown adipose tissues (17,19-25). The adipose field is thus heavily reliant upon the use of transgenic mice which require significant time and investment. With nearly 40% of adults in the United States considered obese, more efficient strategies to study adipose tissues are required to improve our understanding of how these tissues contribute to obesity and to identify potential therapies (73). BAd-CRISPR inducible gene knockout distills the laborious process of generating a transgenic mouse into two basic steps: constructing an AAV8-sgRNA and administering it to the interscapular BAT of Cas9-expressing mice. Our method couples the novelty of CRISPR/Cas9 with the established Cre/LoxP system to enable highly efficient inducible gene knockout in BAT. While we implemented this model for BAT using BAd-CRISPR mice, it is easily amendable to any cell or tissue by crossing the Cre-dependent Rosa26-LSL-Cas9 mice with a tissue specific promoter-driven Cre line (23). Using our cloning strategy, a sgRNA can be incorporated into the AAV expression vector,

validated *in vitro*, used to generate any AAV serotype, and delivered to a tissue of interest. Our work has thus shown for the first time that CRISPR/Cas9 can be harnessed to significantly improve our understanding of BAT. We anticipate that with further optimization it should be applicable to white and marrow adipose tissues too.

We designed and validated highly efficient sgRNAs (53-88%) that caused frameshift mutations in cultured cells in >92% of the total sequences. In general, we prioritized sgRNAs that targeted early coding regions of the gene to introduce a frameshift mutation and disrupt translation of the mRNA. We also observed profound suppression of mRNA expression for each targeted allele, suggesting a mechanism for inhibiting gene transcription. Rational design and validation of sgRNAs *in vitro* allowed us to select highly efficient sgRNAs for gene knockout *in vivo*. We showed that a single administration of AAV8-sgRNA to the interscapular BAT resulted in near total knockout of *Adipoq*, *Atgl*, *Fasn*, *Plin1*, *Scd1*, and *Ucp1* specifically in brown adipocytes. We also showed that multiple sgRNAs could be administered simultaneously using different AAV8 vectors. Morphologically, we observed striking differences between the BAT of mice administered AAV8-ATGL sgRNA, AAV8-PLIN1 sgRNA or a combination of the two. Ideally, future iterations of BAd-CRISPR will entail multiple sgRNAs cloned into a single AAV expression vector. In our model, we were limited by packaging restrictions from the mCherry fluorescent marker, which we included to quantify transduction efficiency. However, based on our data, it is apparent local AAV8 administration to the interscapular BAT leads to robust transduction and subsequent gene knockout. As such, the mCherry marker could be replaced with multiple U6 promoter-driven sgRNAs to different genomic targets. Packaging multiple sgRNAs into a single AAV is advantageous over multiple AAVs to deliver single sgRNAs as only one viral particle needs to transduce a brown adipocyte for gene knockout. Moreover, packaging the sgRNA along with Cas9 into one AAV could provide an all-in-one system for inducible gene knockout. Novel Cas9 orthologs smaller than *S. pyogenes* Cas9 (~1300 amino acids [aa]) such as *N. meningitidis* Cas9 (1082 aa), *S. aureus* Cas9 (1053 aa), *C. jejuni* Cas9 (984 aa), and *G. stearothermophilus* Cas9 (1089 aa) have all been identified for potential use to permanently modify the genome (74). Thus, future iterations may include more compact, highly efficient Cas9 orthologs, for an all-in-one AAV system.

BAd-CRISPR enabled us to generate the first inducible UCP1 knockout mouse model and determine that adult mice can defend core body temperature when cold stressed at 5ºC. We observed elevation of FGF21, which is known be upregulated in response to cold stress for adaptive thermogenesis (32,60,61). RNAseq identified dramatic changes to the transcriptome of BAT in BAd-CRISPR Ucp1 knockout mice. We observed an increase in peroxisomal β-oxidation and lipid metabolism genes along with a decrease in mitochondrial electron transport chain genes suggesting alternative adaptive thermogenesis mechanisms are activated in response to inducible UCP1 loss in adult mice. Gene profiling also suggests that thermogenesis in the absence of UCP1 may be accomplished by a futile cycle of increased protein synthesis and turnover. It is important to note that UCP1 loss was exclusive to the interscapular BAT, which in rodents is the largest BAT depot. However, mice also have smaller BAT depots located in the periaortic, perirenal, and intercostal depots which also express UCP1 (75,76). Therefore, it is likely classical UCP1-mediated adaptive thermogenesis also plays an ancillary role to help maintain body temperature in BAd-CRISPR Ucp1 knockout mice.

Importantly, we did not detect evidence of substantial off-target mutations *in vivo* using unbiased whole genome sequencing and RNAseq. It is known that the total number of mismatched base pairs is a determinant for *S. pyogenes* Cas9 efficiency, and that PAM-proximal mismatches are less tolerated than more distal mismatches (70). Hsu et al. reported that 3 or more mismatches eliminated Cas9 cleavage activity at most genomic loci (70). In the example of *Ucp1* sgRNA, we did not observe significant mutations at 7 off-target loci. Each of these loci contained 3-4 base mismatches. Although CRISPResso2 detected mutations in 1.8% of the reads at the intergenic off-target site in chromosome 18, we did not detect any obvious signs of mutations at this locus using a genomic cleavage assay. While we cannot for certain rule out off-target mutations at this site, the data suggests off-target mutations are quite rare and thus non-substantial.

While we have shown BAd-CRISPR is an efficient and versatile tool for generating inducible gene knockout in BAT, it is not without its limitations. For instance, BAd-CRISPR permanently alters the genome of brown adipocytes only, and thus gene expression is not altered in stromal vascular cells even if infected with AAV8-sgRNA. Moreover, precursor cells that subsequently differentiate into brown adipocytes are also not mutated,

and although adipocyte turnover in humans is estimated to be ~10% per year, long-term studies may necessitate additional injections for sustained knockout (77,78). For broader application of BAd-CRISPR to brown adipocytes, stromal vascular cells, and precursor cells, the Rosa26-Cas9 knockin mouse can be used. In this model, all cells express Cas9-GFP, therefore, gene knockout is enabled in all cell types within a tissue. Indeed, we have shown that local injection of AAV8 to the interscapular BAT also leads to detectable transduction in liver, where expression of sgRNAs would be expected to cause mutations in Rosa26-Cas9 knockin mice. However, incorporating microRNAs into the AAV vector can limit transgene expression in off-target tissues. For example, Jimenez et al. added liver and heart specific microRNAs to AAV8 which significantly reduced transgene expression in each tissue, respectively (39). Thus, several strategies can be employed to modify BAd-CRISPR for targeted gene knockout in whole tissues.

We have thus shown for the first time that CRISPR/Cas9 can be used for inducible gene knockout in BAT *in vivo*. Further optimization of AAV design and Cas9 technologies can improve BAd-CRISPR to target white or marrow adipose tissues for gene knockout, inactivation, or overexpression. Importantly, we have shown that BAd-CRISPR enables generation of transgenic animals with relative ease, less financial investment, and in significantly less time (1-2 months) compared to traditional approaches. We note, however, that our main objective was to provide ample evidence through multiple knockout models to show the efficiency of BAd-CRISPR. Thus, future work sufficiently characterizing the biological consequences of each inducible knockout in BAT of adult mice will be required. Therefore, we hope that BAd-CRISPR will prove useful to the field of adipose tissue and beyond for CRISPR/Cas9 inducible knockout in somatic tissues.

MATERIALS AND METHODS

sgRNA Design and Cloning

sgRNAs were designed using CRISPOR or the Synthego CRISPR Design tool (34). We selected sgRNAs that targeted early coding regions, did not have 0 or 1-base mismatch off-target sites, and had cutting frequency determination (CFD) scores >0.2. The 20-base sgRNA sequence was then used to synthesize a gBlocks Gene fragment that contained a U6 promoter and the sgRNA scaffold as well as the restriction sites PmlI and KpnI (**Supplement 1**) (IDT, Coralville, IA, USA). The AAV expression vector plasmid was generously provided by the University of Michigan Vector Core. We inserted PmlI and KpnI restriction sites into the AAV expression vector plasmid to enable cloning the U6-sgRNA gBlocks (NEB, Ipswich, MA, USA). Digested AAV expression vector plasmid and sgRNA gBlocks were separated using gel electrophoresis and purified using the Wizard SV Gel and PCR Clean-Up System (Promega Corporation, Madison, WI, USA). sgRNA gBlocks were ligated into the AAV expression vector using T4 DNA ligase according to the manufacturer's protocol (NEB, Ipswich, MA, USA).

AAV Production

AAV-sgRNA expression plasmids were transformed into competent DH5α *E. coli* (Thermo Fisher Scientific, Waltham, MA, USA). Plasmids were then isolated using the Qiagen Plasmid Maxi Kit (Qiagen, Hilden, Germany). Plasmids were sequenced prior to being used to generate AAVs (Eurofins Genomics, Louisville, KY, USA). All AAV8-sgRNAs were prepared by the University of Michigan Vector Core.

Cell Culture

Primary adipocyte progenitor cells were isolated from the ears of Rosa26-Cas9 knockin mice (#024858, Jackson Lab, Ellsworth, ME, USA) as previously described and cultured at 5% CO_2 (23,79). Sub-confluent cells were maintained in DMEM:F12 medium (Thermo Fisher Scientific, Waltham, MA, USA) containing 10% fetal bovine serum (FBS; Sigma-Aldrich, St. Louis, MO, USA) and supplemented with 10 ng/mL recombinant basic fibroblast growth factor (PeproTech Inc., Rocky Hill, NJ, USA). AAV-sgRNA expression plasmids were transfected to Cas9 cells using Lipofectamine 3000 according to the

manufacturer's protocol (Thermo Fisher Scientific, Waltham, MA, USA). Cells were collected 4 days after transfection and sorted using the Sony MA900 Cell Sorter operated by the University of Michigan Flow Cytometry Core. Cells were lysed and DNA isolated using the Genomic Cleavage Detection Kit (Thermo Fisher Scientific, Waltham, MA, USA).

Assessment of Mutations

Mutations were assessed using TIDE (https://tide.nki.nl/), the Synthego ICE Analysis tool (www.ice.synthego.com), and the Genomic Cleavage Detection Kit (Thermo Fisher Scientific, Waltham, MA, USA). For each of these assays, we designed primers that flanked the cut site and were >100 bp upstream and downstream from the sgRNA binding site. DNA was amplified using Platinum SuperFi II DNA Polymerase (Thermo Fisher Scientific, Waltham, MA, USA). For TIDE and the Synthego ICE Analysis, amplicons were sequenced (Eurofins Genomics, Louisville, KY, USA), and traces were uploaded to the servers for analysis. The Genomic Cleavage Detection Kit was used according to the manufacturer's protocol. Sequencing primers are listed in **Supplement Table 3.1**.

Animals

All mouse strains for this study originated at Jackson Labs (Bar Harbor, ME, USA). Cre-dependent Cas9-GFP mice (Rosa26-LSL-Cas9, #026175), were bred with *Ucp1* promoter-Cre recombinase (B6.FVB-Tg(Ucp1-cre)1Evdr/J, #024670) to generate BAd-CRISPR mice. Rosa26-Cas9 knockin mice (#024858) were also used. UCP1-deficient mice (Ucp1-/-, #003124) were generously provided by Dr. Liangyou Rui at the University of Michigan. Mice were housed in 12-hour light/12-hour dark cycles with free access to food and water. Temperature was set at 20-21ºC, and room humidity at 28-38%. For cold stress studies, mice were single housed without nesting materials in thermal chambers for 24 hours at 5ºC. Telemeters were implanted into the abdominal cavity to measure core body temperature and surgeries were performed by the Michigan Mouse Phenotyping Center. All animal studies were approved by and conducted in compliance with the policies of the University of Michigan Institutional Animal Care and Usage Committee.

Daily care of mice was overseen by the Unit for Laboratory Animal Medicine at the University of Michigan. Genotyping Primers are listed in **Supplement Table 3.1**.

AAV8 Injection

AAV8 injections were performed as previously described (26,45). In brief, female or male 8-10-week-old BAd-CRISPR, Rosa26-LSL-Cas9, or Rosa26-Cas9 knockin mice were singled-housed 24-hours prior to injection. Mice were anesthetized with 2-4% inhaled isoflurane in O_2 and a small area in the interscapular region was shaved to access BAT. A 1-2 cm incision was made, and the skin was peeled back to visualize the interscapular BAT. AAV8-sgRNAs were diluted in PBS (10^{12} vg/mL or 10^{10} vg/mL as indicated) to a final volume of 100 µL and injected into the interscapular BAT by carefully inserting the needle into each lobe at 2-3 distinct spots and dispensing the virus (~50 µL per BAT lobe). Body weight and food intake were monitored daily to ensure mice were healthy.

Quantitative PCR

Total RNA was purified from frozen tissue using RNA STAT-60 (Tel Test, Alvin, TX, USA) according to the manufacturer's instructions. One µg of total RNA was reverse-transcribed to cDNA using M-MLV Reverse Transcriptase (Invitrogen, Carlsbad, CA, USA). qPCR was performed using a StepOnePlus System (Applied Biosystems, Beverly Hills, MI, USA). All qPCR primers were validated with a cDNA titration curve and product specificity was evaluated by melting curve analysis and gel electrophoresis of the qPCR products. Gene expression was calculated using a cDNA titration curve within each plate and then normalized to the expression of peptidylprolyl isomerase A (*Ppia*) mRNA. qPCR primers are listed in **Supplement Table 3.2**.

RNAseq

Total RNA was isolated as described using RNA STAT-60 (Tel Test, Alvin, TX, USA) and treated with DNAse. Samples were submitted to Beijing Genomics Institute (BGI, Beijing, China) for quality control, library preparation, and paired-end sequencing to generate 101 base pair reads using DNB-SEQ-G400 platform. FASTQ files were downloaded for each sample. The quality of raw read data was checked using FastQC (version v0.11.9) to

identify features of the data that may indicate quality problems (low-quality scores, over-represented sequences, inappropriate GC content) and filtered using fastp (version 0.21.0). Reads were aligned to the GRCm39 reference genome (Ensembl version 104) and quantified using STAR (version 2.7.7a). Quality control was performed on the read tables to ensure adequate depth, knockout of *Ucp1*, and to identify outlier samples. Differential expression analysis was done using DESeq2 (version 1.30.1). Plots were generated using variations or alternative representations of native DESeq2 plotting functions, ggplot2, plotly, and other packages within the R environment (version 4.0.3). To compare BAd-CRISPR Ucp1 and Ucp1-/- mice, RPKM values were taken from GEO entry GSE127251. The expression levels of genes between BAd-CRISPR Ucp1 and UCP1-/- mice were compared using DESeq2. The resulting data was filtered for genes with significant differential expression (adjusted p-value < 0.05). FASTQ files, along with count tables and metadata, can be accessed at GSE176453. All analysis code can be found at github.com/alanrupp/romanelli-jbiolchem-2021.

Immunoblot Analysis

Frozen tissues were homogenized in 1% NP-40, 120 mM NaCl, 50 mM Tris-HCl; pH 7.4, 50 mM NaF, 1x protease inhibitor cocktail (Sigma Aldrich, St. Louis, MO, USA) as previously described (80,81). Homogenate was centrifuged at 18,000 x *g* for 10 minutes at 4ºC. Protein concentration was determined using the BCA protein assay (Thermo Fisher Scientific, Waltham, MA, USA). Samples were diluted to equal protein concentrations in lysis buffer and SDS sample buffer (20 mM Tris; pH 6.8, 2% SDS, 0.01% bromophenol blue, 10% glycerol, 5% 2-mercaptoethanol) and heated at 95ºC for 5 minutes. Proteins were separated by SDS-PAGE on 4-12% gradient polyacrylamide gels (Invitrogen, Carlsbad, CA, USA) and transferred to Immobilon PVDF membranes (Millipore, Billerica, MA, USA). Membranes were blocked in 5% non-fat dried milk in Tris-buffered saline (pH 7.4) containing 0.05% Tween-20 (TTBS) for 30 minutes at room temperature and then immunoblotted with the indicated primary antibodies (1:1000) in 5% BSA in TTBS overnight at 4ºC. Blots were probed with horseradish peroxidase-conjugated secondary antibodies (1:5000) diluted in 5% non-fat dried milk in TTBS for 2.5

hours at room temperature and visualized with Clarity Western ECL Substrate (Bio-Rad, Hercules, CA, USA). Antibodies are listed in **Supplement Table 3.3**.

Histology

Soft tissues were harvested and fixed in 10% neutral buffered formalin overnight at 4ºC. Tissues were then dehydrated in an ethanol gradient (30% for 30 minutes, 50% for 30 minutes, 70% indefinitely) and prepared for paraffin embedding. Paraffin-embedded tissues were sectioned at 5 μm thickness and stained with hematoxylin and eosin (H&E) as previously described (82). Stained sections were imaged using a Zeiss inverted microscope at 100x or 200x magnification.

ELISA

Serum collected from mice was analyzed for circulating FGF21 using the Mouse/Rat FGF-21 Quantikine ELISA Kit (R&D Systems, Minneapolis, MN, USA) by following the manufacturer's protocol.

Immunofluorescence Analysis

Blocks of paraffin-embedded BAT from AAV8-sgRNA ATGL, AAV8-sgRNA PLIN1, and AAV8-Control sgRNA injected mice (n =3 mice) were sectioned at 5 μm and floated onto microscope slides in a 39˚C water bath. Paraffin was removed from sections by 3 sequential 5 minute washes in 100% xylene. Sections were next rehydrated in a series of ethanol washes from 100%, 95%, 70%, and 50% with each concentration consisting of two 10 minute washes, followed by two 5 minute washes in deionized water. Antigen retrieval was achieved by a 20-minute incubation in sodium citrate buffer (10 mM sodium citrate, 0.05% Tween-20, pH 6.0) at 95˚C. Sections were cooled to room temperature, circled by a hydrophobic barrier, then washed twice in deionized water for 5 minutes. Sections were permeabilized with 0.2% Triton X-100, 1X PBS for 10 minutes and blocked in 10% normal donkey serum prepared in TNT buffer (0.1 M Tris-HCl pH 7.4, 0.15 M NaCl, 0.05% Tween 20) for 1 hour. Primary antibodies against ATGL (1:200), UCP-1 (1:100), endomucin (1:250), and PLIN1 (1:100), were prepared in 2.5% normal donkey serum in TNT buffer then centrifuged at 15,000 x *g* for 10 minutes to remove aggregates.

Sections were incubated in primary antibody dilutions for 16 hours at 4˚C. Sections were washed three times in TNT buffer for 5, 10, then 15 minutes. Conjugated secondary antibodies against rabbit, goat, and rat were diluted 1:100 in TNT buffer then centrifuged at 15,000 x *g* for 10 minutes to remove aggregates. Sections were incubated in secondary antibody dilutions for 1.5 hours at room temperature then washed twice for 5 then 10 minutes. Nuclei were stained with 14.3 μM DAPI in PBS for 5 minutes then washed twice in 1X PBS for 5 minutes. No. 1.5 coverslips were mounted to the slides with ProLong Gold mountant (Thermo Fisher Scientific, Waltham, MA, USA) and cured for 2 days at room temperature prior to imaging. Immunofluorescent microscopy was performed using a Nikon A1 laser scanning confocal with Plan Apo VC 60x oil DIC N2 objective. Antibodies are listed in **Supplement Table 3.3**.

Whole Genome Sequencing

Whole genome sequencing was performed by the University of Michigan Advanced Genomics Core using a NovaSeq 6000 system (Illumina, Inc., San Diego, CA, USA). Genomic DNA quality control and NGS library prep services were all performed by the University of Michigan Advanced Genomics Core. FASTQ files were aligned using the mouse genome (Ensembl GRCm38) with bowtie2 (version 2.3.5.1). Indels were identified with CRISPResso2 (version 2.0.45) and visual inspection within the Integrative Genomics Viewer (71).

Statistics

All data are presented as mean ± SD. When comparing two groups, significance was determined using Student's two-tailed t-test. When comparing multiple experimental groups, an analysis of variance (ANOVA) was followed by post hoc analysis with Dunnett's or Sidak's test as appropriate. Differences were considered significant at $p < 0.05$ and are indicated with asterisks.

TABLE 3.1

Sequencing & Genotyping Primers

Primer Name	Sequence
Adipoq F	CCTGATTGGATGTGCCATGT
Adipoq R	CCCCAAATTCAGGACTCTTC
Atgl F	GGGAAATACCAGGCACAGGG
Atgl R	ACACAGGGTAGTAGACAAGG
Fasn F	GGGAGCAGGCAGAGGGTCTC
Fasn R	ATTGGGGAGTGAGGAAACTA
Plin1 F	GACACATGACATATGCTTGT
Plin1 R	CTGTGAGACGATCAGACAGA
Scd1 F	TTTGTGTGTTACTGAGGCTA
Scd1 R	TTCTCTTGGGTCAGGTGGGG
Ucp1 F	GGGGAAATTATAAAAAAGAT
Ucp1 R	CTGGGACCGTGCTGTTTGGG
Ucp1 Off Target #1 F	ATCTGTGGGTGCCAATCTGG
Ucp1 Off Target #1 R	AAGGAAGGTGGGCCATTCTG
Cas9 Genotype F	ACACCAGCACCAAAGAGGTG
Cas9 Genotype R	GTAGGTCAGGGTGGTCACGA
Ucp1-Cre Genotype F	CCTCTGCACTGGCACTACCT
Ucp1-Cre Genotype R	CAGGTTCTTGCGAACCTCAT
Ucp1-/- Genotype F	GGGGTAGTATGCAAGAGAGGTG
Ucp1-/- Genotype R	CCTACCCGCTTCCATTGCTCA

Table 3.1. Sequencing & Genotyping Primers.

TABLE 3.2

qPCR Primers

Primer Name	Sequence
mCherry qPCR F	GAGGCTGAAGCTGAAGGAC
mCherry qPCR R	GATGGTGTAGTCCTCGTTGTG
Ppia qPCR F	CACCGTGTTCTTCGACATCA
Ppia qPCR R	CAGTGCTCAGAGCTCGAAAGT
Adipoq qPCR F	CCCCATGAGTACCAGACTAA
Adipoq qPCR R	TTTCTCTCCCTTCTCTCCAG
Atgl qPCR F	CCTCCTGCCTCCGTGAGCAC
Atgl qPCR R	AAACACGAGTCAGGGAGATG
Fasn qPCR F	GGCTCTATGGATTACCCAAG
Fasn qPCR R	CTCGGGATCTCTGCTAAGGG
Plin1 qPCR F	GAGACTGAGGTGGCGGTCTG
Plin1 qPCR R	GGTGGACAGCCGACGGACCA
Scd1 qPCR F	GTTCTTACACGACCACCACC
Scd1 qPCR R	ATATCTTCTTTCATTTCAGG
Ucp1 qPCR F	GGACACTGCCAAAGTCCGCC
Ucp1 qPCR R	TTCTGACCTTCACGACCTCT
Cidea qPCR F	TAAGAGACGCGGCTTTGGG
Cidea qPCR F	GGGCGAGCTGGATGTATGAG
Dio2 qPCR F	CAGTGTGGTGCACTCCAATC
Dio2 qPCR R	TGAACCAAAGTTGACCACCAG
Fgf21 qPCR F	CTGGGGGTCTACCAAGCAT
Fgf21 qPCR R	CACCCAGGATTTGAATGACC
Ucp2 qPCR F	TACCAGAGCACTGTCGAAGCC
Ucp2 qPCR R	AGTCCCTTTCCAGAGGCCC

Table 3.2. qPCR Primers.

TABLE 3.3

Antibodies

Antibody	Source	Company	Catalog #
ADIPOQ- IB	Rabbit	Sigma Aldrich	A6354
ATGL- IB	Rabbit	Cell Signaling Technology	2138S
ATGL- IF	Rabbit	Abcam	ab207799
FASN- IB	Rabbit	Abcam	ab22759
FLAG (Cas9)- IB	Mouse	Sigma Aldrich	F1804
Endomucin- IF	Rat	Santa Cruz Biotechnology	sc-65495
ERK2- IB	Goat	Santa Cruz Biotechnology	sc-1647
PLIN1- IB	Rabbit	Cell Signaling Technology	9349S
PLIN1- IF	Goat	Abcam	ab61682
SCD1- IB	Rabbit	Cell Signaling Technology	2438S
UCP1- IB & IF	Rabbit	Alpha Diagnostic International	UCP11-A

* IB = Immunoblot, IF = Immunofluorescence

Table 3.3. Antibodies.

SUPPLEMENT 3.1

a

PmlI

CACACACACACGCAGATGCTGCCCTATC**CACGTG**GAGGGCCTATT
TCCCATGATTCCTTCATATTTGCATATACGATACAAGGCTGTTAGAG
AGATAATTGGAATTAATTTGACTGTAAACACAAAGATATTAGTACAA
AATACGTGACGTAGAAAGTAATAATTTCTTGGGTAGTTTGCAGTTTT
AAAATTATGTTTTAAAATGGACTATCATATGCTTACCGTAACTTGAAA
GTATTTCGATTTCTTGGCTTTATATATCTTGTGGAAAGGACGAAACA
CCGNNNNNNNNNNNNNNNNNNGTTTTAGAGCTAGAAATAGCA
AGTTAAAATAAGGCTAGTCCGTTATCAACTTGAAAAAGTGGCACCG
AGTCGGTGCTTTTTT**GGTACC**CAAGGTTCAAACCACCAGGCTG

KpnI

b

Gene	sgRNA Sequence	PAM	CFD Score
Adipoq	TGGGCAGGATTAAGAGGAAC	AGG	0.404
Atgl	CTTGGACACCTCAATAATGT	TGG	0.569
Fasn	GGCTCTATGGATTACCCAAG	CGG	0.687
Plin1	TCACAGGTCCCGCTCACCAC	AGG	0.533
Scd1	GGTGGTGGTCGTGTAAGAAC	TGG	0.513
Ucp1	ATTTGCCTCTGAATGCCCGC	AGG	0.492
Control	TTTGCCCCGAGGCGAGATTG	GGG	0.605

Supplement 3.1. sgRNA cloning sequences. (***a***) U6 promoter-driven sgRNA gBlocks template. The template contains the U6 promoter (green), a 20-bp sgRNA without the PAM (red), the sgRNA scaffold (blue), and a termination sequence (orange). The restriction sites for PmlI and KpnI flank the template and are bolded. The entire sequence (414-bp) is used to create a gBlocks Gene Fragment, digested using PmlI and KpnI, and ligated into the AAV expression vector. (***b***) sgRNA sequences, PAM sites, and CFD scores as calculated by the Synthego sgRNA Design Tool.

FIGURE 3.1

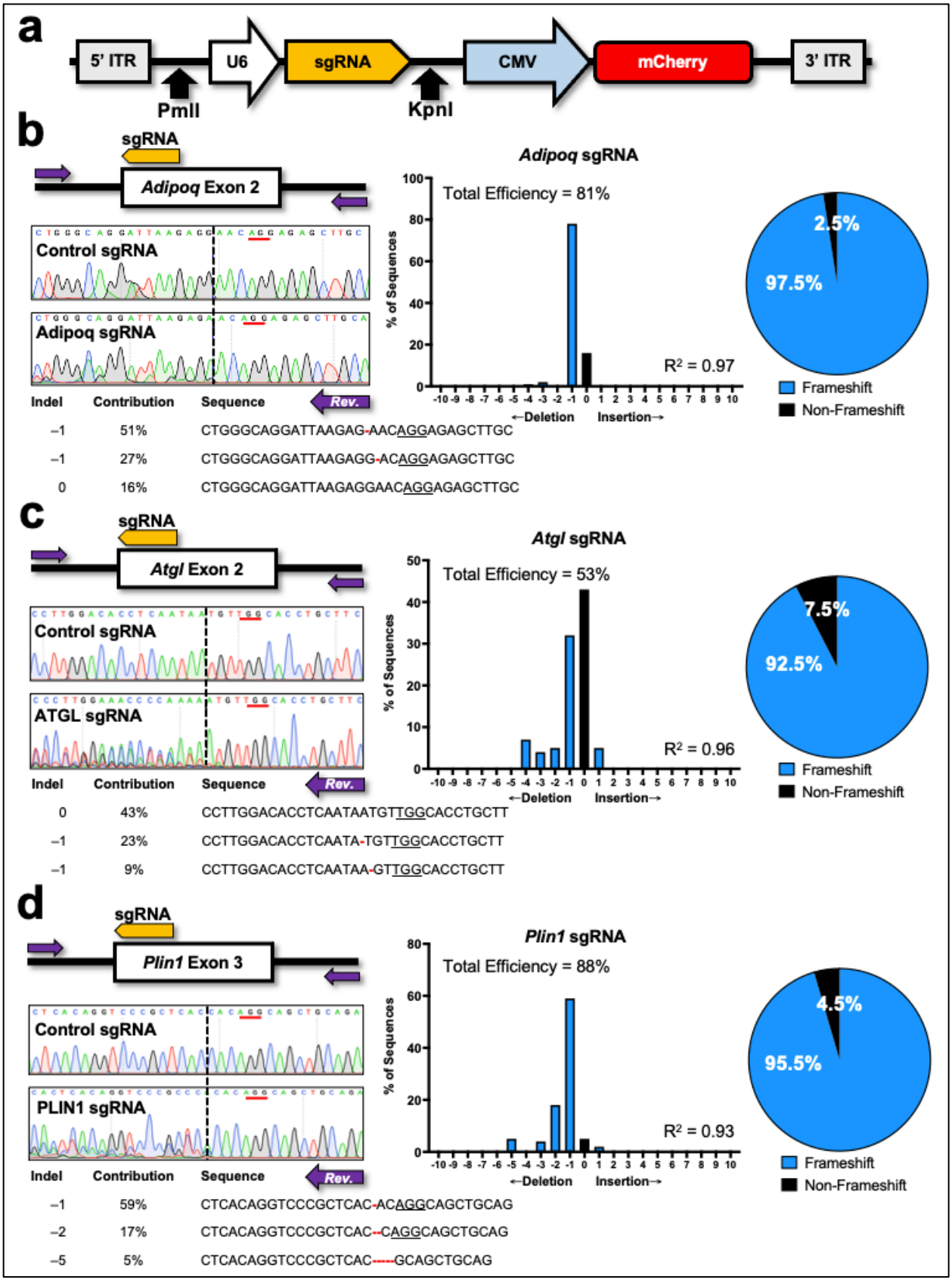
a
5' ITR
U6
sgRNA
CMV
mCherry
3' ITR
PmlI
KpnI
b
sgRNA
Adipoq Exon 2
Control sgRNA
Adipoq sgRNA
Rev.
Adipoq sgRNA
Total Efficiency = 81%
% of Sequences
R² = 0.97
←Deletion Insertion→
2.5%
97.5%
Frameshift
Non-Frameshift
Indel Contribution Sequence
–1 51% CTGGGCAGGATTAAGAG-AACAGGAGAGCTTGC
–1 27% CTGGGCAGGATTAAGAGG-ACAGGAGAGCTTGC
0 16% CTGGGCAGGATTAAGAGGAACAGGAGAGCTTGC
c
sgRNA
Atgl Exon 2
Control sgRNA
ATGL sgRNA
Rev.
Atgl sgRNA
Total Efficiency = 53%
% of Sequences
R² = 0.96
←Deletion Insertion→
7.5%
92.5%
Frameshift
Non-Frameshift
Indel Contribution Sequence
0 43% CCTTGGACACCTCAATAATGTTGGCACCTGCTT
–1 23% CCTTGGACACCTCAATA-TGTTGGCACCTGCTT
–1 9% CCTTGGACACCTCAATAA-GTTGGCACCTGCTT
d
sgRNA
Plin1 Exon 3
Control sgRNA
PLIN1 sgRNA
Rev.
Plin1 sgRNA
Total Efficiency = 88%
% of Sequences
R² = 0.93
←Deletion Insertion→
4.5%
95.5%
Frameshift
Non-Frameshift
Indel Contribution Sequence
–1 59% CTCACAGGTCCCGCTCAC-ACAGGCAGCTGCAG
–2 17% CTCACAGGTCCCGCTCAC--CAGGCAGCTGCAG
–5 5% CTCACAGGTCCCGCTCAC-----GCAGCTGCAG

Figure 3.1. Transfection of adipocyte precursors with sgRNAs predominantly causes frameshift mutations in the target gene. (***a***) U6 promoter-driven sgRNAs were cloned into an AAV expression vector using PmlI and KpnI. The expression vector also contained CMV promoter-driven mCherry and 5' and 3' ITRs to facilitate packaging of the cassette into AAV8. (***b-d***) Sanger sequencing traces from Cas9-expressing adipocyte precursors transfected with AAV8-sgRNAs targeted to *Adipoq*, *Atgl*, and *Plin1*. For each target, primers (purple arrows) were designed upstream and downstream of the sgRNA cut site (yellow arrow). Chromatograms of the reverse strand are shown, and the cut site (black dotted line) and PAM (red underline) are displayed for each sgRNA. The highest frequency indels for each sgRNA and percent contribution as determined by TIDE and the Synthego ICE Analysis tool are shown. Frameshift mutations were calculated by dividing the number of frameshifts over the total number of mutations as estimated by the Synthego ICE Analysis tool.

SUPPLEMENT 3.2

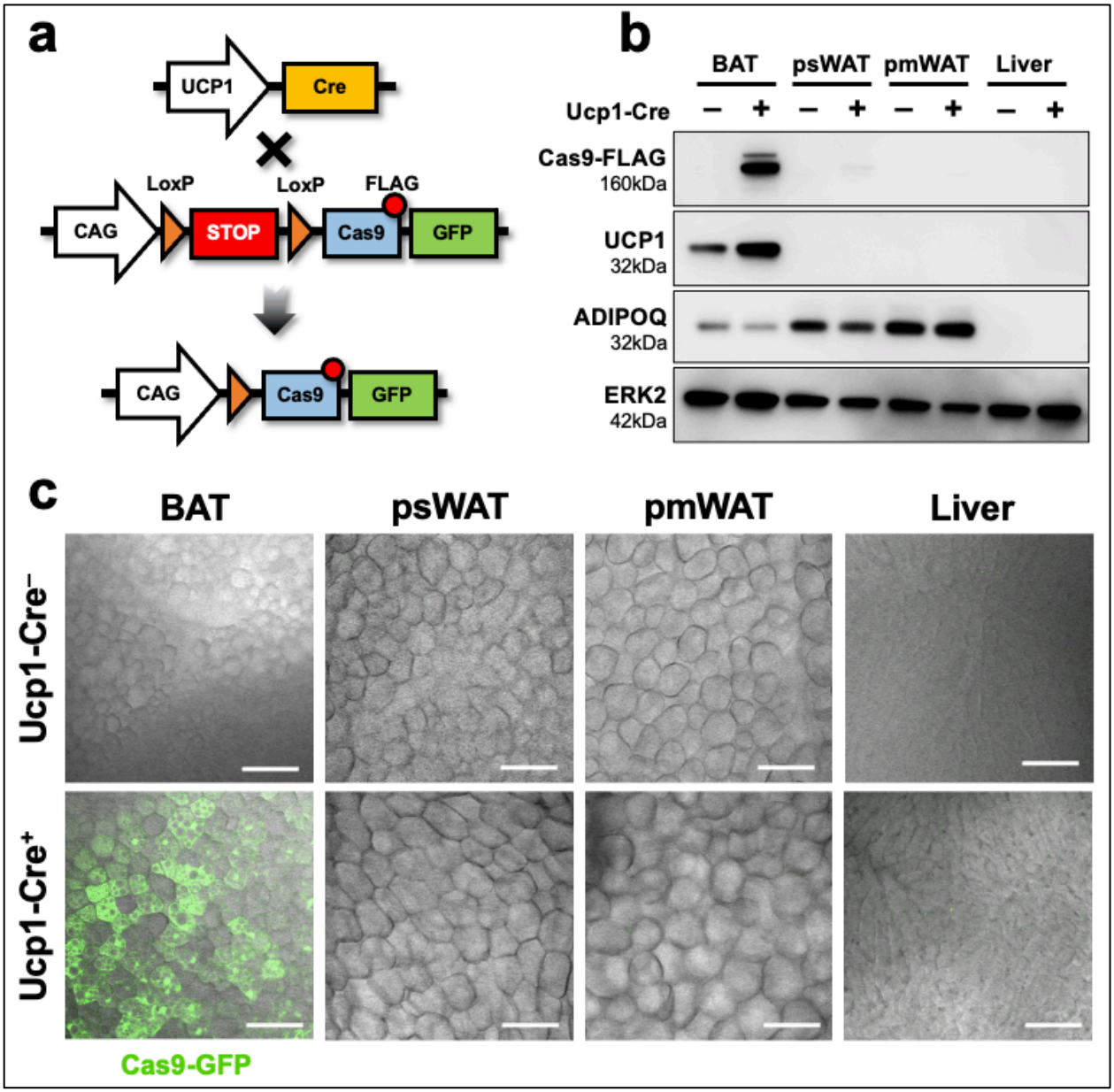

Supplement 3.2. BAd-CRISPR mice express Cas9 exclusively in BAT. (***a***) BAd-CRISPR mice were generated by breeding *Ucp1* promoter-Cre recombinase and Cre-dependent Cas9-GFP mice (Rosa26-LSL-Cas9). (***b***) Immunoblot analyses showing Cas9, UCP1, ADIPOQ, and ERK2 expression with or without Ucp1-Cre. (***c***) Confocal microscopy of freshly dissected BAT, psWAT, pmWAT, and liver from Ucp1-Cre^{-} or Ucp1-Cre^{+} mice; 200x magnification, scale bar, 100 μm (n = 3). Data shown are from female mice.

SUPPLEMENT 3.3

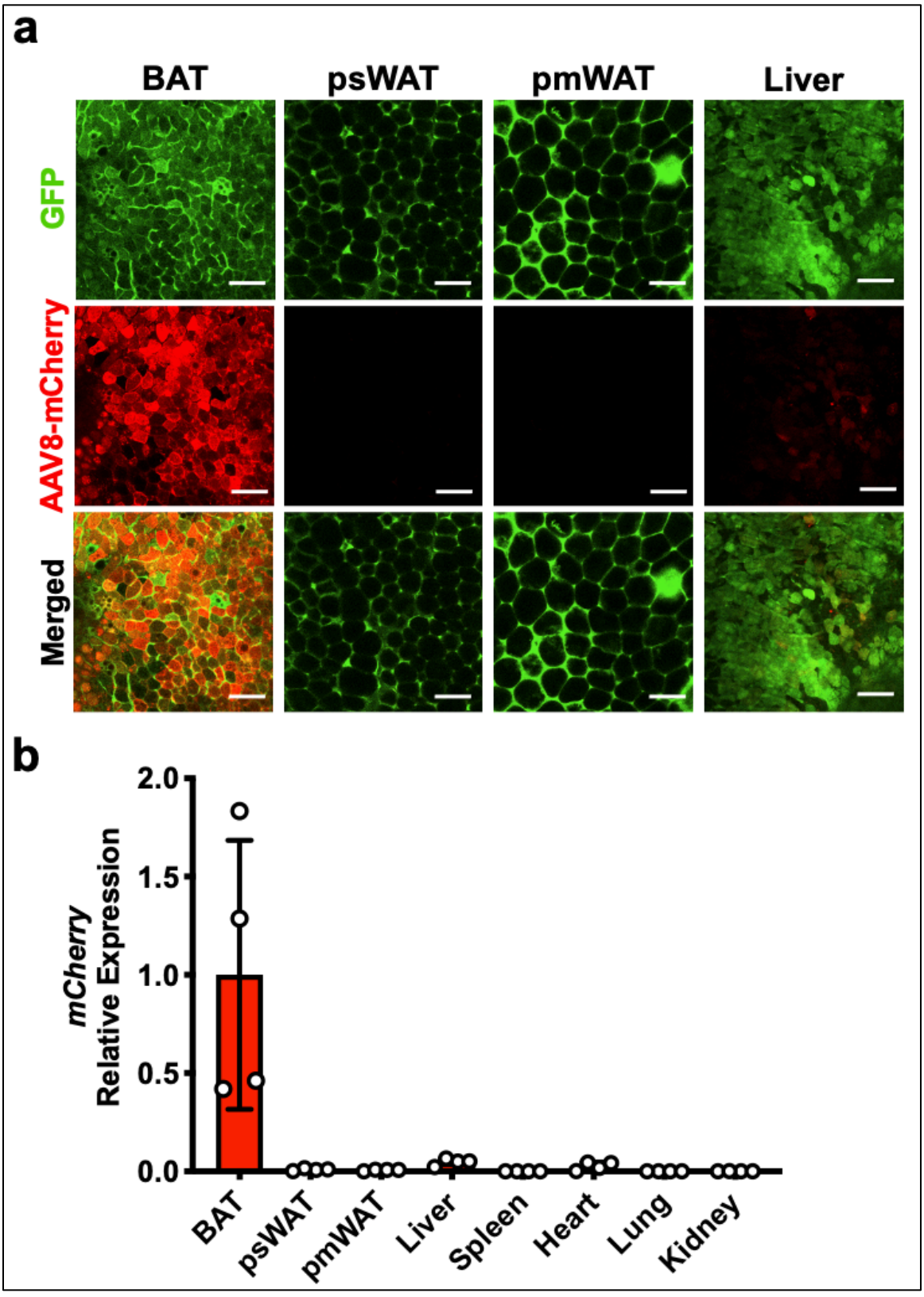

Supplement 3.3. AAV8 direct injection robustly transduces interscapular BAT. (***a***) Confocal micrographs of freshly dissected tissue from Rosa26-Cas9 knockin mice administered 100 µL 10^{12} vg/mL AAV8-mCherry; 200x magnification; scale bar, 100 µm (n = 4). (***b***) *mCherry* mRNA expression; mRNA normalized to PPIA. Data shown are from female mice. Brown adipose tissue (BAT), posterior subcutaneous white adipose tissue (psWAT), parametrial WAT (pmWAT) (n = 4).

FIGURE 3.2

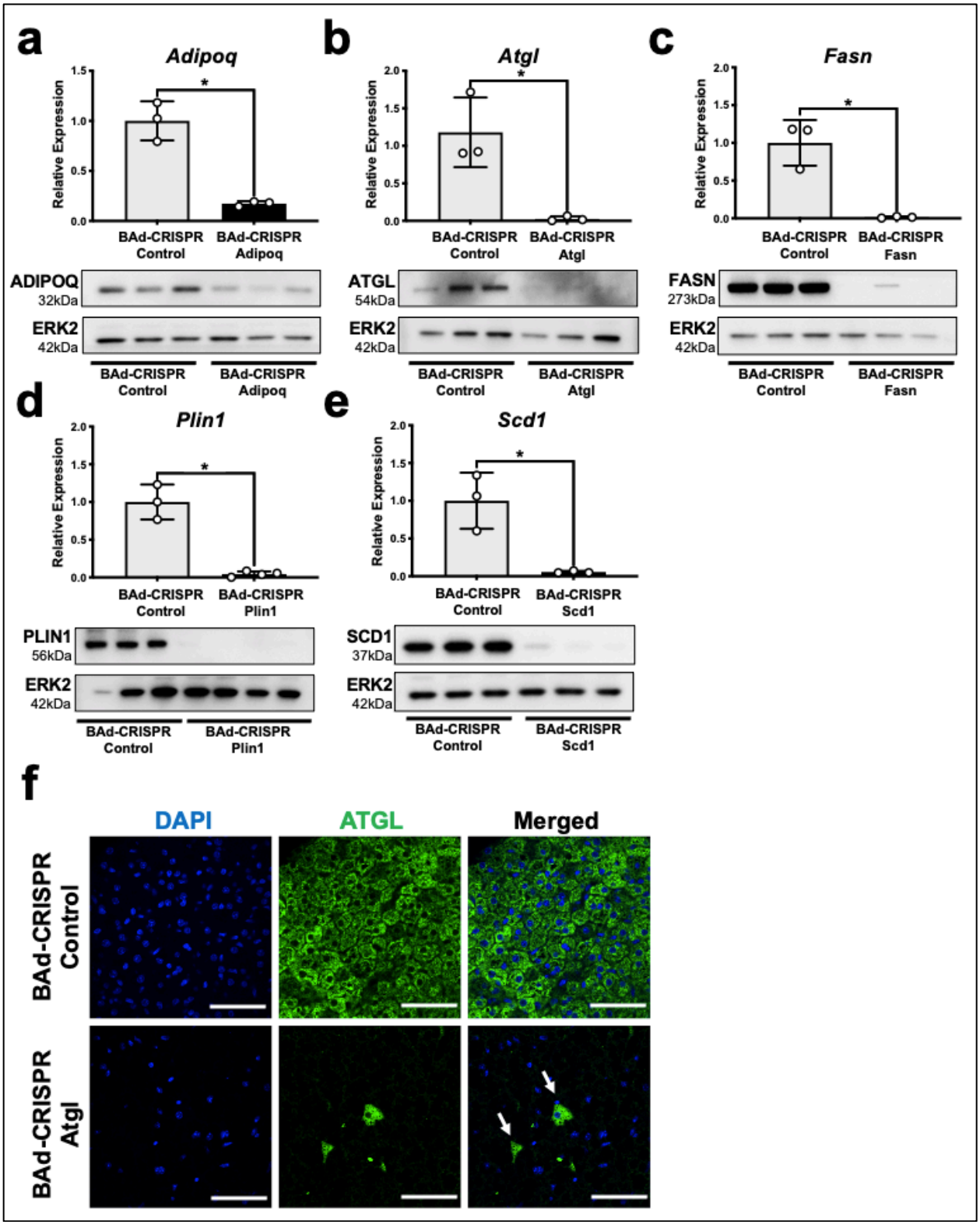
a
Adipoq
Relative Expression
BAd-CRISPR Control
BAd-CRISPR Adipoq
ADIPOQ
32kDa
ERK2
42kDa
b
Atgl
BAd-CRISPR Control
BAd-CRISPR Atgl
ATGL
54kDa
c
Fasn
BAd-CRISPR Fasn
FASN
273kDa
d
Plin1
BAd-CRISPR Plin1
PLIN1
56kDa
e
Scd1
BAd-CRISPR Scd1
SCD1
37kDa
f
DAPI
ATGL
Merged
BAd-CRISPR Control
BAd-CRISPR Atgl

Figure 3.2. BAd-CRISPR induces knockout of Adipoq, ATGL, FASN, PLIN1, and SCD1 in brown adipocytes of adult mice. (***a-e***) BAT mRNA and protein expression of BAd-CRISPR mice administered 100 µL 10^{12} vg/mL AAV8-sgRNA to *Adipoq*, *Atgl*, *Fasn*, *Plin1*, *Scd1*, or Control; mRNA expression was normalized to *Ppia* (n = 3-4). (***f***) Immunofluorescence analysis of paraffin-sectioned BAT from BAd-CRISPR Atgl mice stained for DAPI and immunolabeled against ATGL; 600x magnification, scale bar, 50 µm. White arrows indicate brown adipocytes that were not mutated. Data shown are from male (*Adipoq*, *Atgl*, *Fasn*, *Plin1*, and Control) and female (*Scd1* and Control) mice. Data are presented as mean ± SD. * indicates significance at $p < 0.05$.

FIGURE 3.3

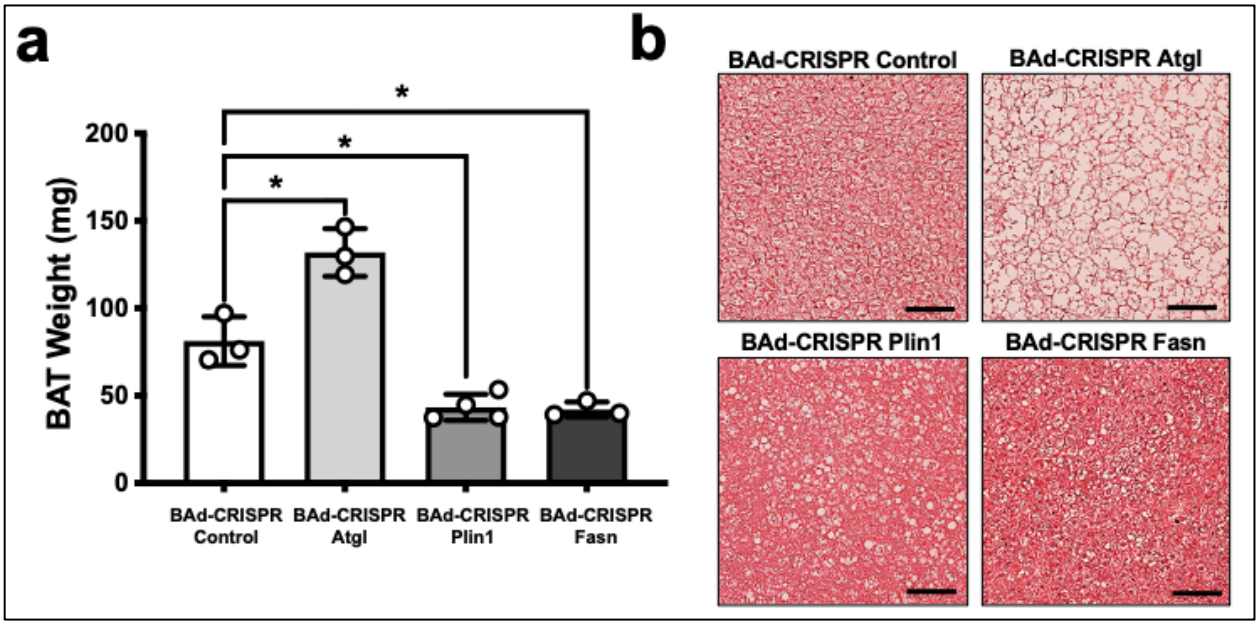

Figure 3.3. BAd-CRISPR Atgl, BAd-CRISPR Plin1, and BAd-CRISPR Fasn inducible knockouts recapitulate previously described BAT phenotypes. (***a***) BAT weight (mg) of BAd-CRISPR mice administered 100 µL 10^{12} vg/mL AAV8-sgRNAs for Control, *Atgl*, *Plin1*, or *Fasn* (n = 3-4). (***b***) H&E staining of BAT; 200x magnification, scale bar, 50 µm. Data shown are from male mice and are presented as mean ± SD. * indicates significance at $p < 0.05$.

FIGURE 3.4

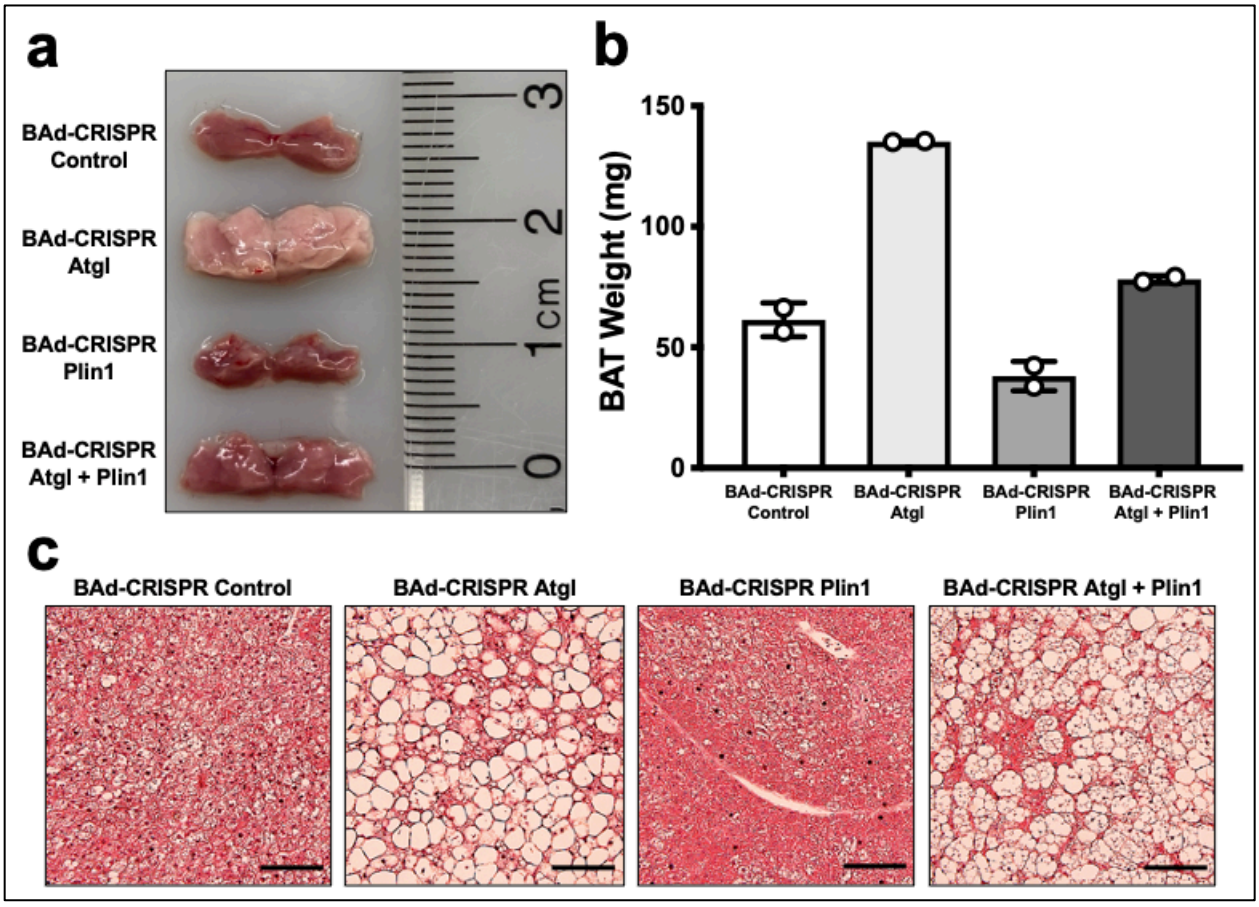

Figure 3.4. BAd-CRISPR enables simultaneous knockout of ATGL and PLIN1 in brown adipocytes. (***a***) Freshly dissected BAT from Rosa26-LSL-Cas9 + AAV8-ATGL sgRNA and AAV8-PLIN1 sgRNA (BAd-CRISPR Control), BAd-CRISPR Atgl, BAd-CRISPR Plin1, and BAd-CRISPR Atlg + Plin1 mice administered 100 µL 10^{10} vg/mL of the designated AAV8 (n = 2). (***b***) BAT weight (mg) of Control, BAd-CRISPR Atgl, BAd-CRISPR Plin1, and BAd-CRISPR Atgl + Plin1 mice. (***c***) H&E staining of BAT; 200x magnification, scale bar, 50 µm. Data shown are from male mice. Data are presented as mean ± SD.

FIGURE 3.5

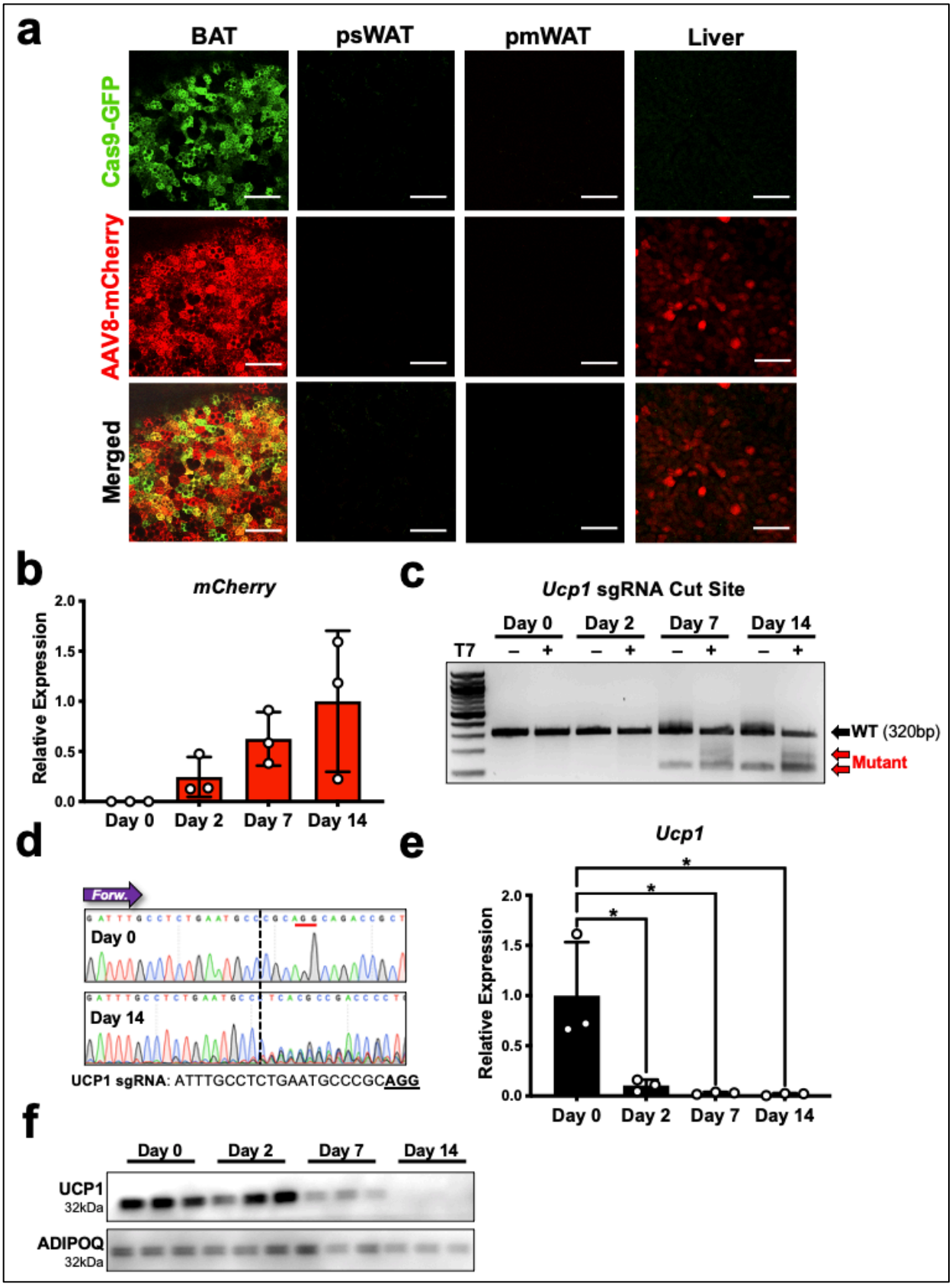
a
BAT
psWAT
pmWAT
Liver
Cas9-GFP
AAV8-mCherry
Merged
b
mCherry
Relative Expression
2.0
1.5
1.0
0.5
0.0
Day 0
Day 2
Day 7
Day 14
c
Ucp1 sgRNA Cut Site
Day 0
Day 2
Day 7
Day 14
T7
– + – + – + – +
WT (320bp)
Mutant
d
Forw.
Day 0
Day 14
UCP1 sgRNA: ATTTGCCTCTGAATGCCCGCAGG
e
Ucp1
Relative Expression
2.0
1.5
1.0
0.5
0.0
*
*
*
Day 0
Day 2
Day 7
Day 14
f
Day 0
Day 2
Day 7
Day 14
UCP1
32kDa
ADIPOQ
32kDa

Figure 3.5. BAd-CRISPR ablates UCP1 expression in brown adipose tissue. (***a***) Confocal micrographs of freshly dissected tissues from BAd-CRISPR Ucp1 mice 14 days after 100 µL 10^{12} vg/mL AAV8-UCP1 sgRNA injection; 200x magnification; scale bar, 50 µm (n = 3). (***b***) *mCherry* mRNA expression at each timepoint, RNA expression normalized to *Ppia* (n = 3 mice per timepoint). (***c***) Genomic Cleavage assay of cDNA isolated from BAT. Red arrows indicate aberrant mutant PCR products. WT band = 320 bp. + or – indicates addition of the T7 endonuclease. (***d***) Sanger sequencing traces of cDNA from 0 or 14 days post injection. The expected cut site is indicated with a dashed line and the PAM is underlined in red. Below, the sgRNA sequence is shown and the PAM is underlined and bolded. The purple arrow indicates the forward primer and sequencing direction. (***e***) mRNA expression of *Ucp1* at each time point, RNA expression normalized to *Ppia* (n = 3 mice per timepoint). (***f***) UCP1 and adiponectin protein expression at 0, 2, 7, or 14 days post AAV8-UCP1 sgRNA injection. Data shown are from female mice and are presented as mean ± SD. * indicates significance at $p < 0.05$.

SUPPLEMENT 3.4

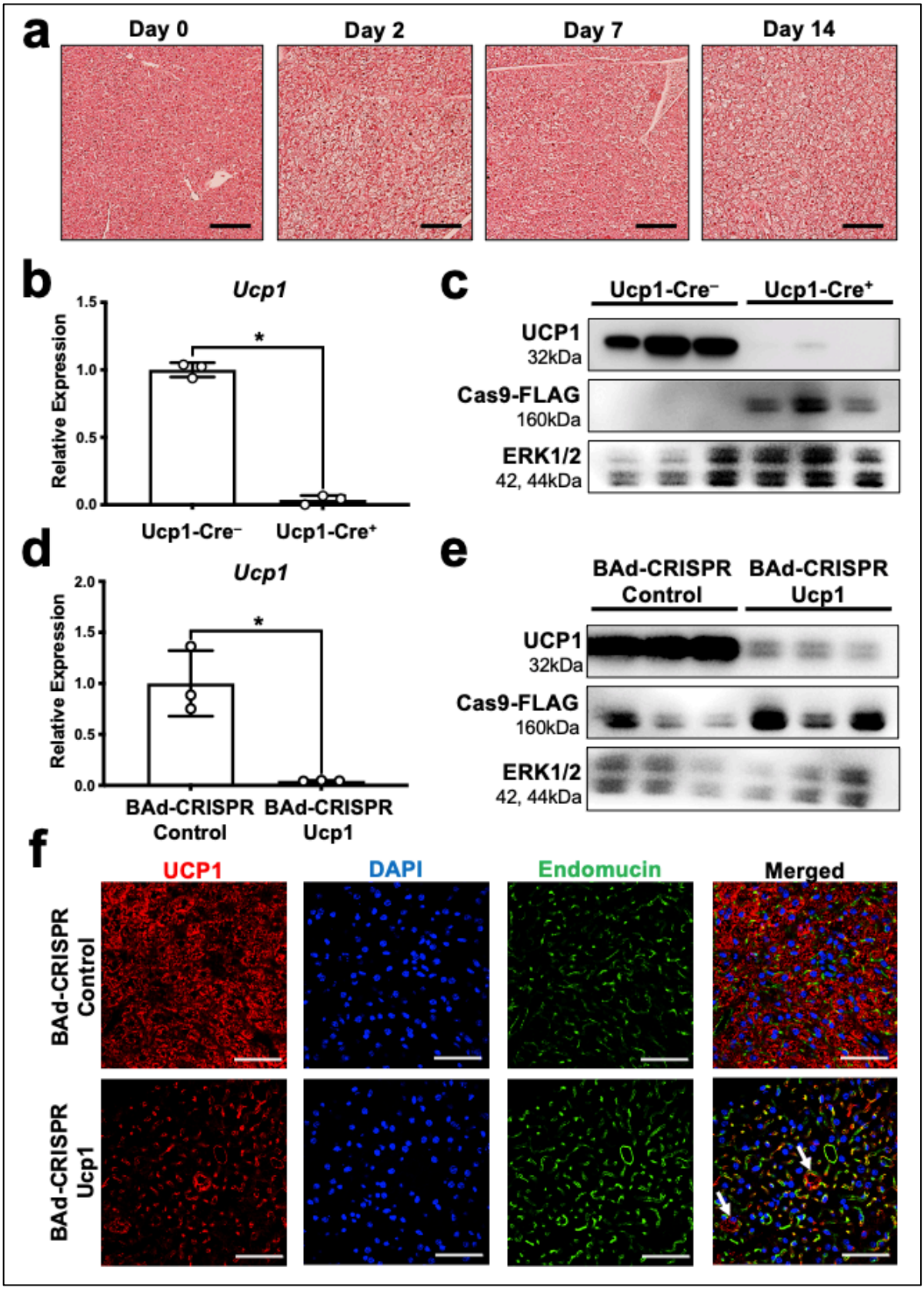

Supplement 3.4. BAd-CRISPR Ucp1 ablates *Ucp1* expression in adult mice. (***a***) H&E staining of BAT from 0, 2, 7, and 14-days post injection with AAV8-UCP1 sgRNA injection (100 µL 10^{12} vg/mL); 200x magnification; scale bar 50 µm (n = 3 mice per timepoint). (***b-c***) UCP1 expression in Rosa26-LSL-Cas9 or BAd-CRISPR Ucp1 mice administered AAV8-UCP1 sgRNA. (***d-e***) UCP1 expression in BAd-CRISPR Control or BAd-CRISPR Ucp1 mice, mRNA normalized to PPIA. (***f***) Immunofluorescence of BAT from BAd-CRISPR Control or BAd-CRISPR Ucp1 mice immunolabeled against UCP1 and endomucin, nuclei stained with DAPI; 600x magnification, scale bar 100 µm. White arrows indicate brown adipocytes that were not mutated. Data shown are from female mice. Data are presented as mean ± SD. * indicates significance at $p < 0.05$.

FIGURE 3.6

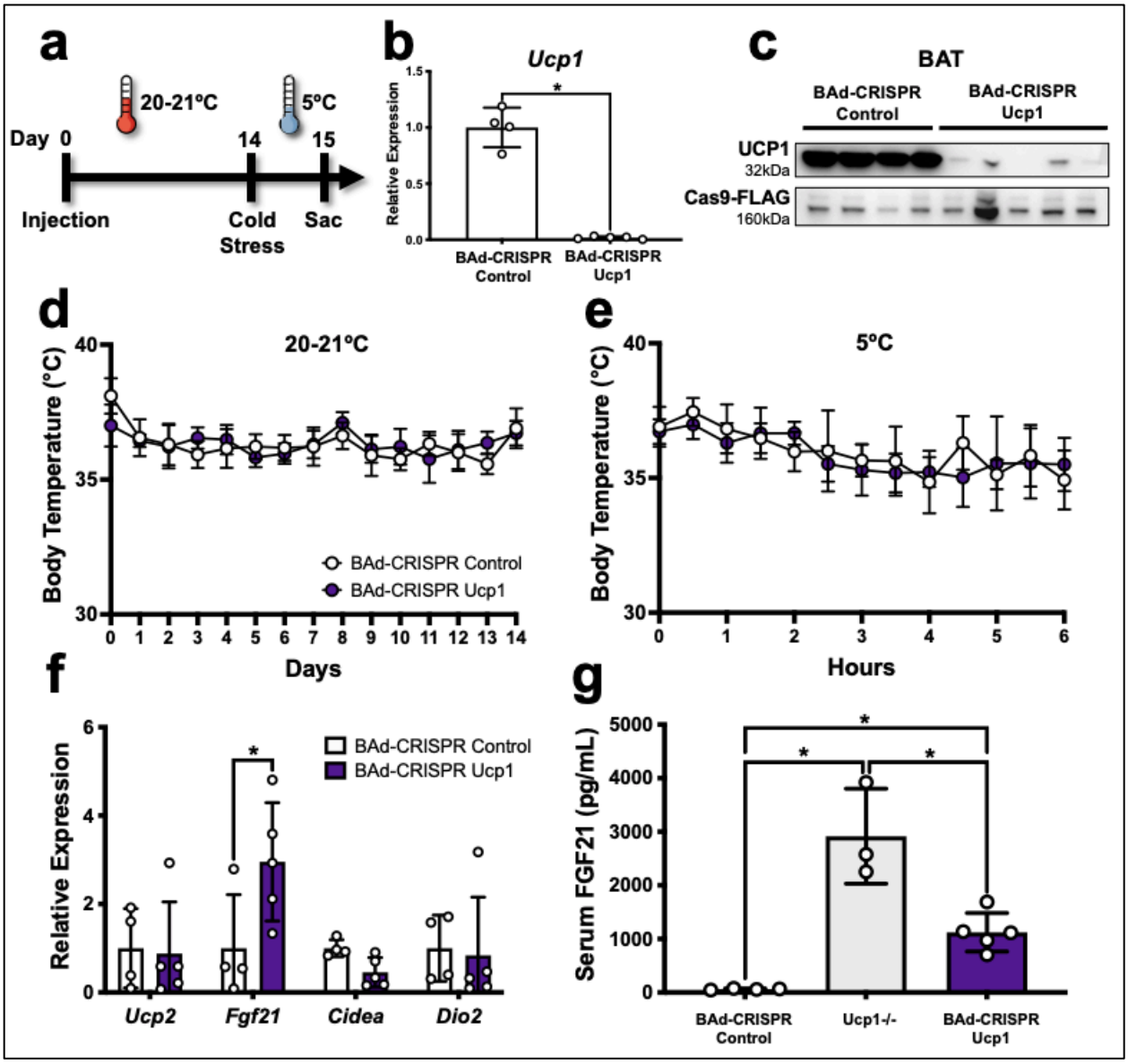

Figure 3.6. BAd-CRISPR Ucp1 inducible knockout mice defend core body temperature and have elevated FGF21. (***a***) 8-10 week old Rosa26-Cas9 knockin mice were implanted with a telemeter 7-days before injection with 100 µL 10^{12} vg/mL AAV8-Control sgRNA or AAV8-UCP1 sgRNA and single housed at 20-21ºC with no enrichment for 14 days after injection. Mice were cold stressed at 5ºC for 24 hours and then sacrificed. (***b***) *Ucp1* mRNA expression, mRNA normalized to *Ppia* (n = 4 or 5 mice). (***c***) Immunoblot showing UCP1 and Cas9 expression. (***d-e***) Body temperature at 20-21ºC and 5ºC. (***f***) Relative expression of thermogenic markers in BAT, mRNA normalized to *Ppia*. (***g***) Serum FGF21 concentrations in Rosa26-LSL-Cas9 (Control), Ucp1-/-, or BAd-CRISPR Ucp1 mice (n = 3, 4, or 5 mice). Data shown are from female mice. Data are presented as mean ± SD. * indicates significance at $p < 0.05$.

SUPPLEMENT 3.5

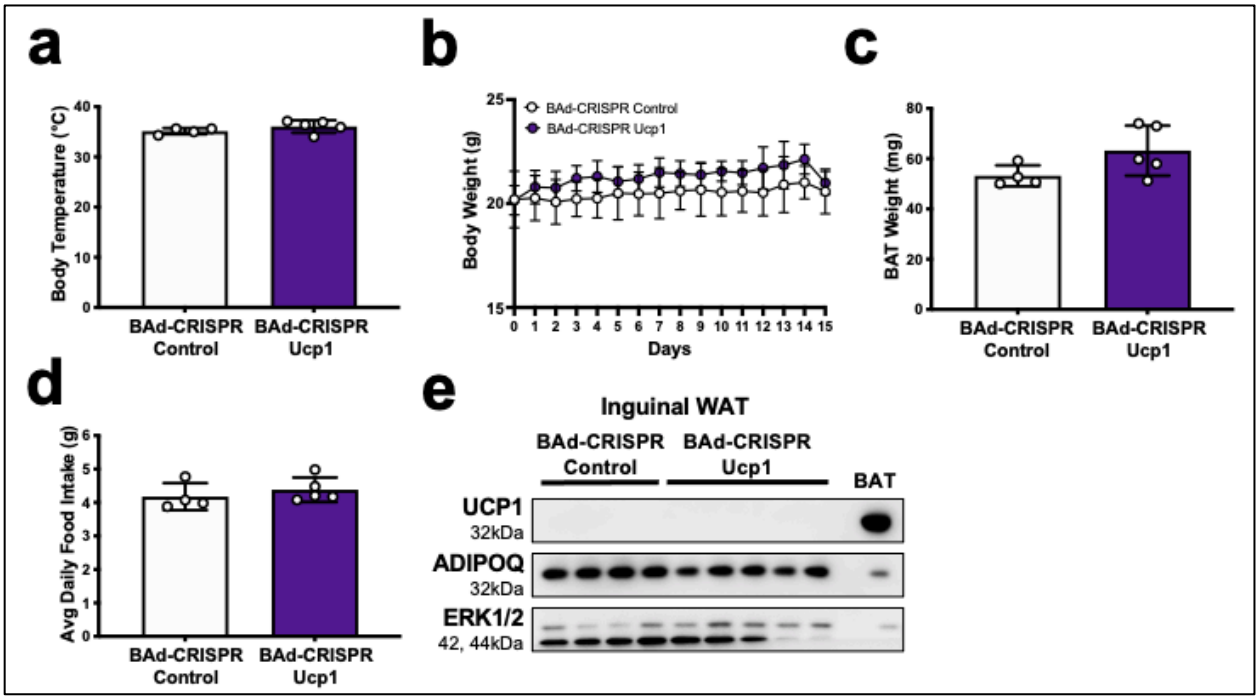

Supplement 3.5. Body temperature, body weight, BAT weight, and food intake are not altered in BAd-CRISPR Ucp1 mice after 24 hour cold stress. (***a***) Body temperature after 24-hours at 5ºC. (***b***) Body weight (g) during 14 day recovery from AAV8 injection to the interscapular BAT. (***c***) Dissected BAT weight (mg). (***d***) Average daily food intake of normal chow diet (g). (***c***) psWAT immunoblot of UCP1 (n = 4-5). Data shown are from female mice.

FIGURE 3.7

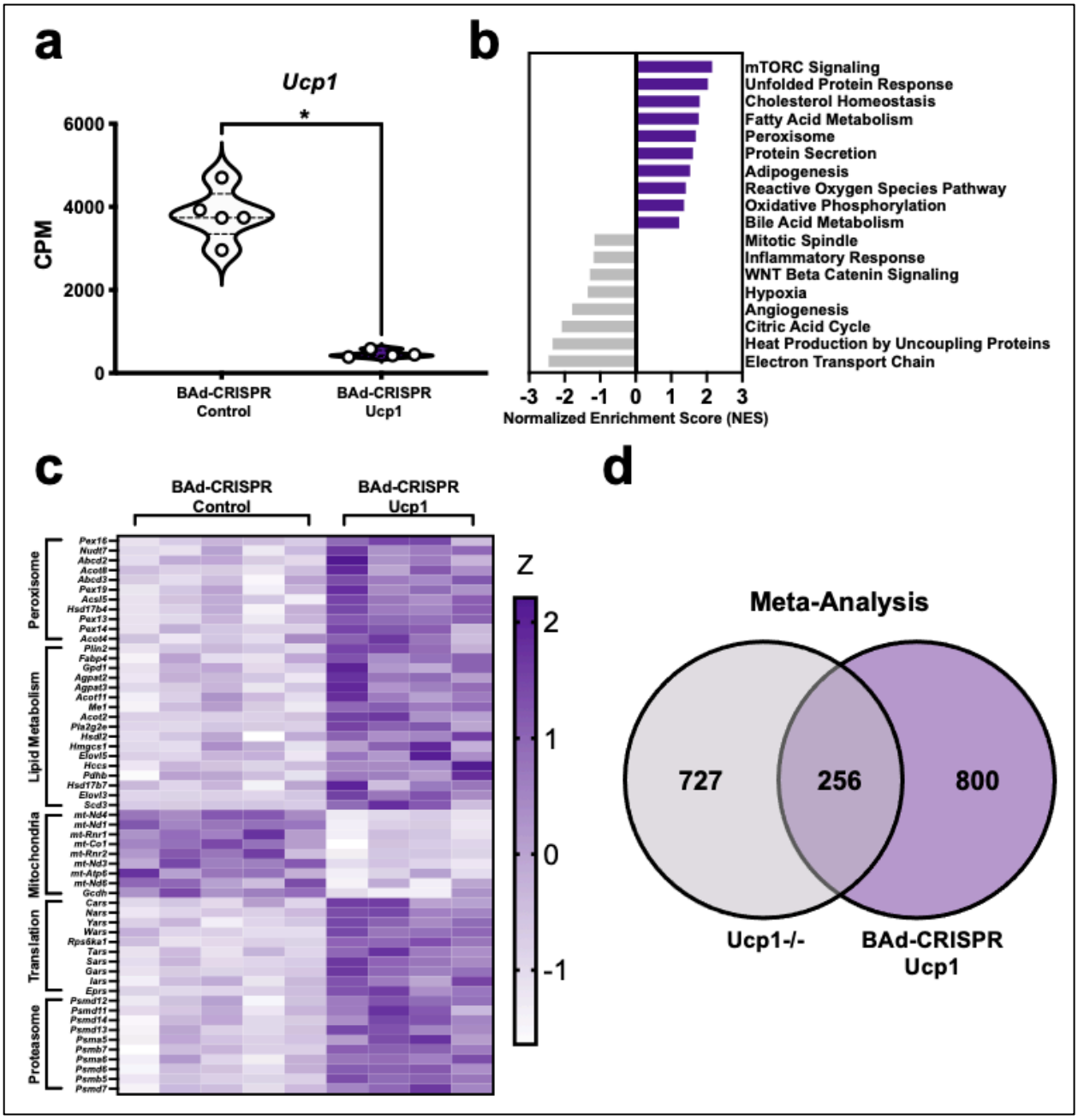

Figure 3.7. Gene profiling of BAT from BAd-CRISPR Ucp1 mice suggests peroxisomal lipid oxidation and increased protein synthesis/turnover as a compensatory thermogenic process. (***a***) Violin plot of *Ucp1* normalized transcript counts per million (CPM) (n = 4 or 5 mice). (***b***) Gene set enrichment analysis (GSEA) of the most up- and down-regulated pathways. (***c***) Heatmap showing the top coordinate regulated expression of genes whose proteins are associated with the peroxisome, lipid metabolism, mitochondrial metabolism, protein translation, and the proteasome. (***d***) Venn diagram depicting overlap of significant differential gene expression of Ucp1-/- and BAd-CRISPR Ucp1 mice taken from GEO entry GSE127251.

FIGURE 3.8

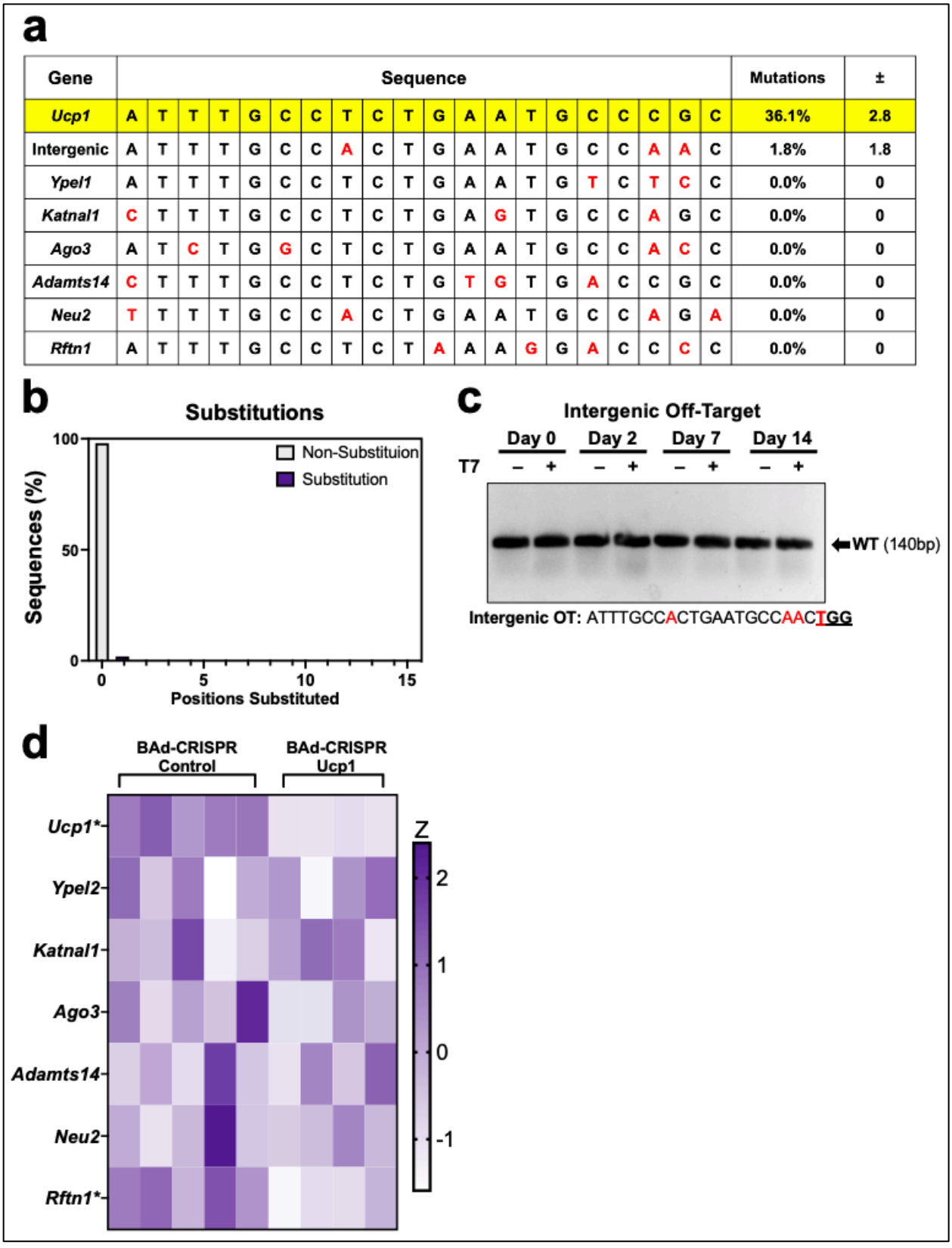

Gene	Sequence																				Mutations	±
Ucp1	A	T	T	T	G	C	C	T	C	T	G	A	A	T	G	C	C	C	G	C	36.1%	2.8
Intergenic	A	T	T	T	G	C	C	A	C	T	G	A	A	T	G	C	C	A	A	C	1.8%	1.8
Ypel1	A	T	T	T	G	C	C	T	C	T	G	A	A	T	G	T	C	T	C	C	0.0%	0
Katnal1	C	T	T	T	G	C	C	T	C	T	G	A	G	T	G	C	C	A	G	C	0.0%	0
Ago3	A	T	C	T	G	G	C	T	C	T	G	A	A	T	G	C	C	A	C	C	0.0%	0
Adamts14	C	T	T	T	G	C	C	T	C	T	G	T	G	T	G	A	C	C	G	C	0.0%	0
Neu2	T	T	T	T	G	C	C	A	C	T	G	A	A	T	G	C	C	A	G	A	0.0%	0
Rftn1	A	T	T	T	G	C	C	T	C	T	A	A	A	G	G	A	C	C	C	C	0.0%	0

Figure 3.8. CRISPR/Cas9 does not lead to observable off-target mutations in BAT of BAd-CRISPR Ucp1 mice. (***a***) Off-target sequence mismatches for UCP1 sgRNA predicted by CRISPOR and the Synthego sgRNA Design tool. The UCP1 sgRNA sequence is highlighted in yellow and base mismatches are colored red. Percent mutations were calculated using whole genome sequencing data visualized by the Integrative Genome Viewer (IGV) and CRISPResso2. (***b***) Indel characterization at the intergenic off-target determined by CRISPResso2. (***c***) Genomic cleavage assay at the intergenic off-target. WT band = 140 bp. (***d***) Heatmap of BAT gene expression for each off-target gene locus represented in the RNAseq dataset for BAd-CRISPR Ucp1 mice.

REFERENCES

1. Bagchi, D. P., Forss, I., Mandrup, S., and MacDougald, O. A. (2018) SnapShot: Niche Determines Adipocyte Character I. *Cell Metab* **27**, 264-264 e261
2. Bagchi, D. P., and MacDougald, O. A. (2019) Identification and Dissection of Diverse Mouse Adipose Depots. *J Vis Exp*
3. Wu, J., Bostrom, P., Sparks, L. M., Ye, L., Choi, J. H., Giang, A. H., Khandekar, M., Virtanen, K. A., Nuutila, P., Schaart, G., Huang, K., Tu, H., van Marken Lichtenbelt, W. D., Hoeks, J., Enerback, S., Schrauwen, P., and Spiegelman, B. M. (2012) Beige adipocytes are a distinct type of thermogenic fat cell in mouse and human. *Cell* **150**, 366-376
4. Li, Z., and MacDougald, O. A. (2021) Preclinical models for investigating how bone marrow adipocytes influence bone and hematopoietic cellularity. *Best Pract Res Clin Endocrinol Metab*, 101547
5. Alexander, C. M., Kasza, I., Yen, C. L., Reeder, S. B., Hernando, D., Gallo, R. L., Jahoda, C. A., Horsley, V., and MacDougald, O. A. (2015) Dermal white adipose tissue: a new component of the thermogenic response. *J Lipid Res* **56**, 2061-2069
6. Trayhurn, P. (2005) Endocrine and signalling role of adipose tissue: new perspectives on fat. *Acta Physiol Scand* **184**, 285-293
7. Rosen, E. D., and Spiegelman, B. M. (2006) Adipocytes as regulators of energy balance and glucose homeostasis. *Nature* **444**, 847-853
8. Corsa, C. A. S., Walsh, C. M., Bagchi, D. P., Foss Freitas, M. C., Li, Z., Hardij, J., Granger, K., Mori, H., Schill, R. L., Lewis, K. T., Maung, J. N., Azaria, R. D., Rothberg, A. E., Oral, E. A., and MacDougald, O. A. (2021) Adipocyte-specific deletion of lamin A/C largely models human familial partial lipodystrophy type 2. *Diabetes*
9. Lee, K. Y., Russell, S. J., Ussar, S., Boucher, J., Vernochet, C., Mori, M. A., Smyth, G., Rourk, M., Cederquist, C., Rosen, E. D., Kahn, B. B., and Kahn, C. R. (2013) Lessons on conditional gene targeting in mouse adipose tissue. *Diabetes* **62**, 864-874
10. Kong, X., Banks, A., Liu, T., Kazak, L., Rao, R. R., Cohen, P., Wang, X., Yu, S., Lo, J. C., Tseng, Y. H., Cypess, A. M., Xue, R., Kleiner, S., Kang, S., Spiegelman, B. M., and Rosen, E. D. (2014) IRF4 is a key thermogenic transcriptional partner of PGC-1alpha. *Cell* **158**, 69-83
11. Krueger, K. C., Costa, M. J., Du, H., and Feldman, B. J. (2014) Characterization of Cre recombinase activity for in vivo targeting of adipocyte precursor cells. *Stem Cell Reports* **3**, 1147-1158
12. Rosenwald, M., Perdikari, A., Rulicke, T., and Wolfrum, C. (2013) Bi-directional interconversion of brite and white adipocytes. *Nat Cell Biol* **15**, 659-667
13. Wang, Q. A., and Scherer, P. E. (2014) The AdipoChaser mouse: A model tracking adipogenesis in vivo. *Adipocyte* **3**, 146-150
14. Jeffery, E., Berry, R., Church, C. D., Yu, S., Shook, B. A., Horsley, V., Rosen, E. D., and Rodeheffer, M. S. (2014) Characterization of Cre recombinase models for the study of adipose tissue. *Adipocyte* **3**, 206-211
15. Bozec, A., Bakiri, L., Jimenez, M., Rosen, E. D., Catala-Lehnen, P., Schinke, T., Schett, G., Amling, M., and Wagner, E. F. (2013) Osteoblast-specific expression

of Fra-2/AP-1 controls adiponectin and osteocalcin expression and affects metabolism. *J Cell Sci* **126**, 5432-5440
16. Ye, R., Wang, Q. A., Tao, C., Vishvanath, L., Shao, M., McDonald, J. G., Gupta, R. K., and Scherer, P. E. (2015) Impact of tamoxifen on adipocyte lineage tracing: Inducer of adipogenesis and prolonged nuclear translocation of Cre recombinase. *Mol Metab* **4**, 771-778
17. Zafra, M. P., and Dow, L. E. (2016) Somatic Genome Editing Goes Viral. *Trends Mol Med* **22**, 831-833
18. Doudna, J. A., and Charpentier, E. (2014) Genome editing. The new frontier of genome engineering with CRISPR-Cas9. *Science* **346**, 1258096
19. Dow, L. E. (2015) Modeling Disease In Vivo With CRISPR/Cas9. *Trends Mol Med* **21**, 609-621
20. Sanchez-Rivera, F. J., Papagiannakopoulos, T., Romero, R., Tammela, T., Bauer, M. R., Bhutkar, A., Joshi, N. S., Subbaraj, L., Bronson, R. T., Xue, W., and Jacks, T. (2014) Rapid modelling of cooperating genetic events in cancer through somatic genome editing. *Nature* **516**, 428-431
21. Cheng, R., Peng, J., Yan, Y., Cao, P., Wang, J., Qiu, C., Tang, L., Liu, D., Tang, L., Jin, J., Huang, X., He, F., and Zhang, P. (2014) Efficient gene editing in adult mouse livers via adenoviral delivery of CRISPR/Cas9. *FEBS Lett* **588**, 3954-3958
22. Swiech, L., Heidenreich, M., Banerjee, A., Habib, N., Li, Y., Trombetta, J., Sur, M., and Zhang, F. (2015) In vivo interrogation of gene function in the mammalian brain using CRISPR-Cas9. *Nat Biotechnol* **33**, 102-106
23. Platt, R. J., Chen, S., Zhou, Y., Yim, M. J., Swiech, L., Kempton, H. R., Dahlman, J. E., Parnas, O., Eisenhaure, T. M., Jovanovic, M., Graham, D. B., Jhunjhunwala, S., Heidenreich, M., Xavier, R. J., Langer, R., Anderson, D. G., Hacohen, N., Regev, A., Feng, G., Sharp, P. A., and Zhang, F. (2014) CRISPR-Cas9 knockin mice for genome editing and cancer modeling. *Cell* **159**, 440-455
24. Dow, L. E., Fisher, J., O'Rourke, K. P., Muley, A., Kastenhuber, E. R., Livshits, G., Tschaharganeh, D. F., Socci, N. D., and Lowe, S. W. (2015) Inducible in vivo genome editing with CRISPR-Cas9. *Nat Biotechnol* **33**, 390-394
25. Guo, Y., VanDusen, N. J., Zhang, L., Gu, W., Sethi, I., Guatimosim, S., Ma, Q., Jardin, B. D., Ai, Y., Zhang, D., Chen, B., Guo, A., Yuan, G. C., Song, L. S., and Pu, W. T. (2017) Analysis of Cardiac Myocyte Maturation Using CASAAV, a Platform for Rapid Dissection of Cardiac Myocyte Gene Function In Vivo. *Circ Res* **120**, 1874-1888
26. Gomez-Banoy, N., and Lo, J. C. (2017) Genetic Manipulation with Viral Vectors to Assess Metabolism and Adipose Tissue Function. *Methods Mol Biol* **1566**, 109-124
27. Romanelli, S. M., and MacDougald, O. A. (2020) Viral and Nonviral Transfer of Genetic Materials to Adipose Tissues: Toward a Gold Standard Approach. *Diabetes* **69**, 2581-2588
28. Bates, R., Huang, W., and Cao, L. (2020) Adipose Tissue: An Emerging Target for Adeno-associated Viral Vectors. *Mol Ther Methods Clin Dev* **19**, 236-249
29. Shen, Y., Cohen, J. L., Nicoloro, S. M., Kelly, M., Yenilmez, B., Henriques, F., Tsagkaraki, E., Edwards, Y. J. K., Hu, X., Friedline, R. H., Kim, J. K., and Czech, M. P. (2018) CRISPR-delivery particles targeting nuclear receptor-interacting

protein 1 (Nrip1) in adipose cells to enhance energy expenditure. *J Biol Chem* **293**, 17291-17305
30. Kamble, P. G., Hetty, S., Vranic, M., Almby, K., Castillejo-Lopez, C., Abalo, X. M., Pereira, M. J., and Eriksson, J. W. (2020) Proof-of-concept for CRISPR/Cas9 gene editing in human preadipocytes: Deletion of FKBP5 and PPARG and effects on adipocyte differentiation and metabolism. *Sci Rep* **10**, 10565
31. Cannon, B., and Nedergaard, J. (2004) Brown adipose tissue: function and physiological significance. *Physiol Rev* **84**, 277-359
32. Villarroya, F., Cereijo, R., Villarroya, J., and Giralt, M. (2017) Brown adipose tissue as a secretory organ. *Nat Rev Endocrinol* **13**, 26-35
33. Cypess, A. M., Lehman, S., Williams, G., Tal, I., Rodman, D., Goldfine, A. B., Kuo, F. C., Palmer, E. L., Tseng, Y. H., Doria, A., Kolodny, G. M., and Kahn, C. R. (2009) Identification and importance of brown adipose tissue in adult humans. *N Engl J Med* **360**, 1509-1517
34. Concordet, J. P., and Haeussler, M. (2018) CRISPOR: intuitive guide selection for CRISPR/Cas9 genome editing experiments and screens. *Nucleic Acids Res* **46**, W242-W245
35. Doench, J. G., Fusi, N., Sullender, M., Hegde, M., Vaimberg, E. W., Donovan, K. F., Smith, I., Tothova, Z., Wilen, C., Orchard, R., Virgin, H. W., Listgarten, J., and Root, D. E. (2016) Optimized sgRNA design to maximize activity and minimize off-target effects of CRISPR-Cas9. *Nat Biotechnol* **34**, 184-191
36. Brinkman, E. K., Chen, T., Amendola, M., and van Steensel, B. (2014) Easy quantitative assessment of genome editing by sequence trace decomposition. *Nucleic Acids Res* **42**, e168
37. Shapiro, J., Iancu, O., Jacobi, A. M., McNeill, M. S., Turk, R., Rettig, G. R., Amit, I., Tovin-Recht, A., Yakhini, Z., Behlke, M. A., and Hendel, A. (2020) Increasing CRISPR Efficiency and Measuring Its Specificity in HSPCs Using a Clinically Relevant System. *Mol Ther Methods Clin Dev* **17**, 1097-1107
38. Sentmanat, M. F., Peters, S. T., Florian, C. P., Connelly, J. P., and Pruett-Miller, S. M. (2018) A Survey of Validation Strategies for CRISPR-Cas9 Editing. *Sci Rep* **8**, 888
39. Jimenez, V., Munoz, S., Casana, E., Mallol, C., Elias, I., Jambrina, C., Ribera, A., Ferre, T., Franckhauser, S., and Bosch, F. (2013) In vivo adeno-associated viral vector-mediated genetic engineering of white and brown adipose tissue in adult mice. *Diabetes* **62**, 4012-4022
40. O'Neill, S. M., Hinkle, C., Chen, S. J., Sandhu, A., Hovhannisyan, R., Stephan, S., Lagor, W. R., Ahima, R. S., Johnston, J. C., and Reilly, M. P. (2014) Targeting adipose tissue via systemic gene therapy. *Gene Ther* **21**, 653-661
41. Liu, X., Magee, D., Wang, C., McMurphy, T., Slater, A., During, M., and Cao, L. (2014) Adipose tissue insulin receptor knockdown via a new primate-derived hybrid recombinant AAV serotype. *Mol Ther Methods Clin Dev* **1**
42. Huang, W., McMurphy, T., Liu, X., Wang, C., and Cao, L. (2016) Genetic Manipulation of Brown Fat Via Oral Administration of an Engineered Recombinant Adeno-associated Viral Serotype Vector. *Mol Ther* **24**, 1062-1069

43. Huang, W., Liu, X., Queen, N. J., and Cao, L. (2017) Targeting Visceral Fat by Intraperitoneal Delivery of Novel AAV Serotype Vector Restricting Off-Target Transduction in Liver. *Mol Ther Methods Clin Dev* **6**, 68-78
44. Huang, W., Queen, N. J., and Cao, L. (2019) rAAV-Mediated Gene Delivery to Adipose Tissue. *Methods Mol Biol* **1950**, 389-405
45. Balkow, A., Hoffmann, L. S., Klepac, K., Glode, A., Gnad, T., Zimmermann, K., and Pfeifer, A. (2016) Direct lentivirus injection for fast and efficient gene transfer into brown and beige adipose tissue. *J Biol Methods* **3**, e48
46. Haemmerle, G., Lass, A., Zimmermann, R., Gorkiewicz, G., Meyer, C., Rozman, J., Heldmaier, G., Maier, R., Theussl, C., Eder, S., Kratky, D., Wagner, E. F., Klingenspor, M., Hoefler, G., and Zechner, R. (2006) Defective lipolysis and altered energy metabolism in mice lacking adipose triglyceride lipase. *Science* **312**, 734-737
47. Schreiber, R., Diwoky, C., Schoiswohl, G., Feiler, U., Wongsiriroj, N., Abdellatif, M., Kolb, D., Hoeks, J., Kershaw, E. E., Sedej, S., Schrauwen, P., Haemmerle, G., and Zechner, R. (2017) Cold-Induced Thermogenesis Depends on ATGL-Mediated Lipolysis in Cardiac Muscle, but Not Brown Adipose Tissue. *Cell Metab* **26**, 753-763 e757
48. Tansey, J. T., Sztalryd, C., Gruia-Gray, J., Roush, D. L., Zee, J. V., Gavrilova, O., Reitman, M. L., Deng, C. X., Li, C., Kimmel, A. R., and Londos, C. (2001) Perilipin ablation results in a lean mouse with aberrant adipocyte lipolysis, enhanced leptin production, and resistance to diet-induced obesity. *Proc Natl Acad Sci U S A* **98**, 6494-6499
49. Souza, S. C., Christoffolete, M. A., Ribeiro, M. O., Miyoshi, H., Strissel, K. J., Stancheva, Z. S., Rogers, N. H., D'Eon, T. M., Perfield, J. W., 2nd, Imachi, H., Obin, M. S., Bianco, A. C., and Greenberg, A. S. (2007) Perilipin regulates the thermogenic actions of norepinephrine in brown adipose tissue. *J Lipid Res* **48**, 1273-1279
50. Guilherme, A., Pedersen, D. J., Henchey, E., Henriques, F. S., Danai, L. V., Shen, Y., Yenilmez, B., Jung, D., Kim, J. K., Lodhi, I. J., Semenkovich, C. F., and Czech, M. P. (2017) Adipocyte lipid synthesis coupled to neuronal control of thermogenic programming. *Mol Metab* **6**, 781-796
51. Zechner, R., Zimmermann, R., Eichmann, T. O., Kohlwein, S. D., Haemmerle, G., Lass, A., and Madeo, F. (2012) FAT SIGNALS--lipases and lipolysis in lipid metabolism and signaling. *Cell Metab* **15**, 279-291
52. Miyoshi, H., Perfield, J. W., 2nd, Souza, S. C., Shen, W. J., Zhang, H. H., Stancheva, Z. S., Kraemer, F. B., Obin, M. S., and Greenberg, A. S. (2007) Control of adipose triglyceride lipase action by serine 517 of perilipin A globally regulates protein kinase A-stimulated lipolysis in adipocytes. *J Biol Chem* **282**, 996-1002
53. Enerback, S., Jacobsson, A., Simpson, E. M., Guerra, C., Yamashita, H., Harper, M. E., and Kozak, L. P. (1997) Mice lacking mitochondrial uncoupling protein are cold-sensitive but not obese. *Nature* **387**, 90-94
54. Grimpo, K., Volker, M. N., Heppe, E. N., Braun, S., Heverhagen, J. T., and Heldmaier, G. (2014) Brown adipose tissue dynamics in wild-type and UCP1-knockout mice: in vivo insights with magnetic resonance. *J Lipid Res* **55**, 398-409

55. Meyer, C. W., Willershauser, M., Jastroch, M., Rourke, B. C., Fromme, T., Oelkrug, R., Heldmaier, G., and Klingenspor, M. (2010) Adaptive thermogenesis and thermal conductance in wild-type and UCP1-KO mice. *Am J Physiol Regul Integr Comp Physiol* **299**, R1396-1406
56. Golozoubova, V., Hohtola, E., Matthias, A., Jacobsson, A., Cannon, B., and Nedergaard, J. (2001) Only UCP1 can mediate adaptive nonshivering thermogenesis in the cold. *FASEB J* **15**, 2048-2050
57. Meyer, C. W., Ootsuka, Y., and Romanovsky, A. A. (2017) Body Temperature Measurements for Metabolic Phenotyping in Mice. *Front Physiol* **8**, 520
58. Moazed, B., and Desautels, M. (2002) Differentiation-dependent expression of cathepsin D and importance of lysosomal proteolysis in the degradation of UCP1 in brown adipocytes. *Can J Physiol Pharmacol* **80**, 515-525
59. Azzu, V., Jastroch, M., Divakaruni, A. S., and Brand, M. D. (2010) The regulation and turnover of mitochondrial uncoupling proteins. *Biochim Biophys Acta* **1797**, 785-791
60. Keipert, S., Kutschke, M., Lamp, D., Brachthauser, L., Neff, F., Meyer, C. W., Oelkrug, R., Kharitonenkov, A., and Jastroch, M. (2015) Genetic disruption of uncoupling protein 1 in mice renders brown adipose tissue a significant source of FGF21 secretion. *Mol Metab* **4**, 537-542
61. Keipert, S., Kutschke, M., Ost, M., Schwarzmayr, T., van Schothorst, E. M., Lamp, D., Brachthauser, L., Hamp, I., Mazibuko, S. E., Hartwig, S., Lehr, S., Graf, E., Plettenburg, O., Neff, F., Tschop, M. H., and Jastroch, M. (2017) Long-Term Cold Adaptation Does Not Require FGF21 or UCP1. *Cell Metab* **26**, 437-446 e435
62. Lodhi, I. J., and Semenkovich, C. F. (2009) Why we should put clothes on mice. *Cell Metab* **9**, 111-112
63. Seeley, R. J., and MacDougald, O. A. (2021) Mice as experimental models for human physiology: when several degrees in housing temperature matter. *Nat Metab* **3**, 443-445
64. Lodhi, I. J., and Semenkovich, C. F. (2014) Peroxisomes: a nexus for lipid metabolism and cellular signaling. *Cell Metab* **19**, 380-392
65. Torrent, M., Chalancon, G., de Groot, N. S., Wuster, A., and Madan Babu, M. (2018) Cells alter their tRNA abundance to selectively regulate protein synthesis during stress conditions. *Sci Signal* **11**
66. Pollo-Oliveira, L., and de Crecy-Lagard, V. (2019) Can Protein Expression Be Regulated by Modulation of tRNA Modification Profiles? *Biochemistry* **58**, 355-362
67. Livneh, I., Cohen-Kaplan, V., Cohen-Rosenzweig, C., Avni, N., and Ciechanover, A. (2016) The life cycle of the 26S proteasome: from birth, through regulation and function, and onto its death. *Cell Res* **26**, 869-885
68. Bartelt, A., Widenmaier, S. B., Schlein, C., Johann, K., Goncalves, R. L. S., Eguchi, K., Fischer, A. W., Parlakgul, G., Snyder, N. A., Nguyen, T. B., Bruns, O. T., Franke, D., Bawendi, M. G., Lynes, M. D., Leiria, L. O., Tseng, Y. H., Inouye, K. E., Arruda, A. P., and Hotamisligil, G. S. (2018) Brown adipose tissue thermogenic adaptation requires Nrf1-mediated proteasomal activity. *Nat Med* **24**, 292-303

69. Maurer, S. F., Fromme, T., Mocek, S., Zimmermann, A., and Klingenspor, M. (2020) Uncoupling protein 1 and the capacity for nonshivering thermogenesis are components of the glucose homeostatic system. *Am J Physiol Endocrinol Metab* **318**, E198-E215
70. Hsu, P. D., Scott, D. A., Weinstein, J. A., Ran, F. A., Konermann, S., Agarwala, V., Li, Y., Fine, E. J., Wu, X., Shalem, O., Cradick, T. J., Marraffini, L. A., Bao, G., and Zhang, F. (2013) DNA targeting specificity of RNA-guided Cas9 nucleases. *Nat Biotechnol* **31**, 827-832
71. Pinello, L., Canver, M. C., Hoban, M. D., Orkin, S. H., Kohn, D. B., Bauer, D. E., and Yuan, G. C. (2016) Analyzing CRISPR genome-editing experiments with CRISPResso. *Nat Biotechnol* **34**, 695-697
72. Clement, K., Rees, H., Canver, M. C., Gehrke, J. M., Farouni, R., Hsu, J. Y., Cole, M. A., Liu, D. R., Joung, J. K., Bauer, D. E., and Pinello, L. (2019) CRISPResso2 provides accurate and rapid genome editing sequence analysis. *Nat Biotechnol* **37**, 224-226
73. Bluher, M. (2019) Obesity: global epidemiology and pathogenesis. *Nat Rev Endocrinol* **15**, 288-298
74. Edraki, A., Mir, A., Ibraheim, R., Gainetdinov, I., Yoon, Y., Song, C. Q., Cao, Y., Gallant, J., Xue, W., Rivera-Perez, J. A., and Sontheimer, E. J. (2019) A Compact, High-Accuracy Cas9 with a Dinucleotide PAM for In Vivo Genome Editing. *Mol Cell* **73**, 714-726 e714
75. Cinti, S. (2001) The adipose organ: morphological perspectives of adipose tissues. *Proc Nutr Soc* **60**, 319-328
76. Poher, A. L., Altirriba, J., Veyrat-Durebex, C., and Rohner-Jeanrenaud, F. (2015) Brown adipose tissue activity as a target for the treatment of obesity/insulin resistance. *Front Physiol* **6**, 4
77. Arner, P., Bernard, S., Salehpour, M., Possnert, G., Liebl, J., Steier, P., Buchholz, B. A., Eriksson, M., Arner, E., Hauner, H., Skurk, T., Ryden, M., Frayn, K. N., and Spalding, K. L. (2011) Dynamics of human adipose lipid turnover in health and metabolic disease. *Nature* **478**, 110-113
78. Sakaguchi, M., Fujisaka, S., Cai, W., Winnay, J. N., Konishi, M., O'Neill, B. T., Li, M., Garcia-Martin, R., Takahashi, H., Hu, J., Kulkarni, R. N., and Kahn, C. R. (2017) Adipocyte Dynamics and Reversible Metabolic Syndrome in Mice with an Inducible Adipocyte-Specific Deletion of the Insulin Receptor. *Cell Metab* **25**, 448-462
79. Mori, H., Prestwich, T. C., Reid, M. A., Longo, K. A., Gerin, I., Cawthorn, W. P., Susulic, V. S., Krishnan, V., Greenfield, A., and Macdougald, O. A. (2012) Secreted frizzled-related protein 5 suppresses adipocyte mitochondrial metabolism through WNT inhibition. *J Clin Invest* **122**, 2405-2416
80. Mori, H., Dugan, C. E., Nishii, A., Benchamana, A., Li, Z., Cadenhead, T. S. t., Das, A. K., Evans, C. R., Overmyer, K. A., Romanelli, S. M., Peterson, S. K., Bagchi, D. P., Corsa, C. A., Hardij, J., Learman, B. S., El Azzouny, M., Coon, J. J., Inoki, K., and MacDougald, O. A. (2021) The molecular and metabolic program by which white adipocytes adapt to cool physiologic temperatures. *PLoS Biol* **19**, e3000988

81. Bagchi, D. P., Nishii, A., Li, Z., DelProposto, J. B., Corsa, C. A., Mori, H., Hardij, J., Learman, B. S., Lumeng, C. N., and MacDougald, O. A. (2020) Wnt/beta-catenin signaling regulates adipose tissue lipogenesis and adipocyte-specific loss is rigorously defended by neighboring stromal-vascular cells. *Mol Metab* **42**, 101078
82. Parlee, S. D., Lentz, S. I., Mori, H., and MacDougald, O. A. (2014) Quantifying size and number of adipocytes in adipose tissue. *Methods Enzymol* **537**, 93-122

CHAPTER IV

Discussion and Future Perspectives

Viral and nonviral strategies to administer CRISPR/Cas9 for inducible gene knockout have proved revolutionary for modeling disease in a variety of tissues (1-10). While CRISPR/Cas9 has been applied to cultured preadipocytes and adipocytes, its use to inducibly knockout genes in adipose tissues of adult mice has not been reported (11-15). Indeed, targeting adipose tissues *in vivo* has remained elusive owing to their distribution across the body in unique depots and efforts to efficiently target adipocytes using AAVs or nonviral vectors have reported mixed results (16-18). Therefore, time consuming and resource costly transgenic mice are predominately used to model disease and study gene function *in vivo*. However, with the growing obesity epidemic, strategies to improve the way in which adipose tissues are studied are required. Thus, my doctoral work has developed the BAd-CRISPR method to enable rapid and efficient genome editing in BAT of adult mice and show for the first time that CRISPR/Cas9 can be applied to adipose tissue *in vivo*.

BAd-CRISPR resulted in knockout of *Adipoq*, *Atgl*, *Fasn*, *Plin1*, *Scd1*, and *Ucp1* and recapitulated known BAT phenotypes, thereby demonstrating its scalability and utility. Importantly, it distilled the process of generating a transgenic mouse from 6-12 months to ≤2 months. Inducible knockout of UCP1 revealed striking changes to the transcriptome and suggested a combination of peroxisomal β-oxidation and protein synthesis/turnover as a compensatory mechanism to maintain body temperature in response to cold stress. These data show that BAd-CRISPR can be applied to further our understanding of BAT. However, they also highlight important questions that remain to be answered.

What is the mechanism by which BAd-CRISPR Ucp1 inducible knockout mice defend core body temperature?

Interestingly, BAd-CRISPR Ucp1 inducible knockout mice maintain body temperature at both room temperature (20-21ºC) and during a cold stress (5ºC) via an upregulation of pathways involved in fatty acid metabolism, the peroxisome, and protein synthesis/turnover and a decrease in pathways related to the mitochondrial electron transport chain and heat production by uncoupling proteins. We observed a similar phenomenon in RNAseq data from Ucp1-/- mice on a normal chow diet housed at 20ºC, which also had an upregulation of pathways involved in the peroxisome and lipid metabolism (19). These results suggest a reliance on peroxisomal β-oxidation of fatty acids to generate heat. β-oxidation of fatty acids occurs in both the mitochondria and peroxisomes of eukaryotic cells; however, oxidation of long chain fatty acids ≥26 carbon chain length occurs exclusively in peroxisomes (20,21). Both mitochondrial and peroxisomal β-oxidation follow the same enzymatic steps: removal of two hydrogens to produce a *trans* double bond between the α and β carbons, formation of 3-L-hydroxyacyl-CoA, dehydrogenation of 3-L-hydroxyacyl-CoA to form 3-ketoacyl-CoA, and cleavage of the terminal acetyl CoA group to form a new acyl CoA molecule that is two carbons shorter (20). However, peroxisomal β-oxidation differs from mitochondrial β-oxidation in that peroxisomes lack a respiratory chain, and thus electrons from $FADH_2$ are transferred to O_2 to form H_2O_2 and energy is released as heat (20). These data thus provide evidence to support that peroxisomes may be involved in adaptive thermogenesis independently of UCP1 (20,22).

Coupled with this, we also observed elevated expression of tRNA synthetase genes (*Cars*, *Nars*, *Yars*, *Wars*, *Tars*, *Sars*, *Gars*, *Iars*, and *Eprs)* in addition to genes coding for subunits of the proteasome. Collectively, this suggests a futile cycle in which *de novo* protein synthesis is required for adaptive thermogenesis and protection from cellular stress (23,24). Interestingly, we also see an upregulation of genes related to the proteasome in Ucp1-/- mice (19). Thus, dynamic changes to the transcriptome account for a compensatory thermogenic process in response to inducible loss of UCP1. However, the mechanism by which these contribute to the maintenance of body temperature remains to be elucidated.

Future work will thus seek to understand how peroxisomal β-oxidation and protein synthesis/turnover promote adaptive thermogenesis. Lipidomics analyses can identify how peroxisomal β-oxidation and/or α-oxidation contribute to heat production and further an understanding of how the peroxisome contributes to adaptive thermogenesis independently of UCP1. Additionally, proteomics analyses can shed insight into the nature of protein synthesis/turnover and help to identify how these counteractive processes defend body temperature. Comparing mitochondrial respiration of BAd-CRISPR Ucp1, Ucp1-/-, and control mice can also indicate if metabolism is altered (25). Collectively, these experiments will further elucidate mechanisms by which inducible UCP1 knockout mice maintain adaptive thermogenesis.

Can BAd-CRISPR be modified to target white and bone marrow adipose tissues?

As we have demonstrated, BAd-CRISPR is an efficient method to inducibly knockout gene expression in BAT of adult mice. While we anticipate that BAd-CRISPR will positively impact the field of BAT research, we ultimately hope that this method will be broadly applied to the field of adipose tissue. To this point, significant progress must be made in transducing white and bone marrow adipose tissues. In preliminary studies, we were unable to demonstrate uniform transduction of psWAT following direct injection of AAV8 and AAV2. Additionally, our efforts to transduce bone marrow adipocytes via intra-tibial injection of AAV8 have been unsuccessful. Thus, strategies to improve AAV transduction efficiency are required. Such strategies may involve capsid engineering to produce novel recombinant AAV serotypes that show affinity for white and bone marrow adipose tissues (17,18).

The Bosch laboratory was the first group to comprehensively screen AAVs for adipocyte affinity by administering AAV1, AAV6, AAV7, AAV8, and AAV9 (26). Since this paper was first published in 2013, significant advances in AAV capsid engineering have been made to improve transduction efficiency (18,27-29). For example, directed evolution has generated libraries of capsid variants by random shuffling of capsid gene fragments, peptide display, or PCR-based mutagenesis (27,29,30). While these strategies have been used to tailor capsid variants for a wide array of cell types, few efforts have been made to engineer capsid variants for adipocytes (18). Of these, the hybrid serotype Rec2, which

was generated by engineering capsid fragments from AAV8, cynomolgus macaque-variant 5, rhesus macaque-variant 20, and rhesus macaque-variant 39, has been shown to effectively transduce adipose tissue (18,31). Using Rec2, the Cao laboratory has demonstrated robust transduction of BAT and WATs (32-35). Thus, future work should seek to package sgRNAs into Rec2 and assess transduction efficiency in WATs as well as in bone marrow adipose tissue. Considering the bone marrow adipose niche is much less understood, screening the known AAV serotypes (AAV1-AAV11) should be attempted as well.

Beyond screening AAV serotypes and novel capsid variants, adjusting the viral dosage may improve transduction efficiency in WATs as well. To transduce adipose tissues, AAVs are generally dosed between 10^9 to 10^{12} vg/mL depending on the route of administration and depot (16-18). For BAd-CRISPR, 100 µL of 10^{12} vg/mL AAV8-mCherry was directly injected into the interscapular BAT (50 µL per BAT lobe). While this worked effectively for BAT, transducing WAT and bone marrow adipose tissues may require further dose optimization. Thus, performing a dose-response experiment in which AAV8-mCherry is administered to white and bone marrow adipose depots at increasing dosages may help to optimize transduction on a depot-by-depot basis. Additionally, administering AAVs with nonionic surfactants such as Pluronic F88 has shown promise in transducing adipocytes as it has a low toxicity profile and can stabilize the cell membrane for improved uptake (36,37). Significant work is still required to apply BAd-CRISPR to additional adipose depots; however, through rational vector design and optimization of dosage, this method can significantly improve the field of adipose tissue research.

What is the mechanism by which BAd-CRISPR suppresses gene expression?

CRISPR/Cas systems can be broadly classified into two groups: Class I, in which multi-subunit Cas proteins complex to facilitate cleavage, and Class II, in which a single Cas protein causes genomic cleavage (38-40). As such, the majority of studies employing CRISPR/Cas systems have utilized Class II, as it requires one Cas protein and can be packaged into viral vectors. BAd-CRISPR capitalizes on the Class II system and uses *S. pyogenes* Cas9 to generate frameshift mutations in genomic DNA and ablate gene expression. This process first occurs by the pairing of sgRNA to Cas9 to form a

ribonucleoprotein complex (41). The ribonucleoprotein complex then binds to the PAM sequence and unwinds the double-stranded genomic DNA, forming an RNA-DNA heteroduplex starting at the PAM-proximal region and extending distally down the sgRNA (42). Concomitantly, the non-target DNA strand forms a single-stranded DNA “R-loop” that causes Cas9 to undergo a conformational change and activates its two nuclease domains, HNH, and RuvC (43). HNH hydrolyzes the phosphodiester DNA backbone on the sgRNA-bound target DNA strand and RuvC hydrolyzes the PAM-containing non-target DNA strand to cause a double-stranded break (44). The non-homologous end joining (NHEJ) repair pathway is then activated to fix the double-stranded break but is error prone and results in the formation of indels that cause frameshift mutations to disrupt gene expression (38).

As we have shown, the BAd-CRISPR method resulted in complete knockout of *Adipoq*, *Atgl*, *Fasn*, *Plin1*, *Scd1*, and *Ucp1*. For each target, one sgRNA was used to target an early coding region of the gene. We demonstrated that sgRNAs primarily caused frameshift mutations in >90% of the mutated sequences and the majority of these were deletions of 1 base pair. Surprisingly, however, mRNA was virtually undetectable for each target gene knocked out using BAd-CRISPR. We performed quantitative PCR (qPCR) in exons upstream, downstream, or flanking the sgRNA cut site and consistently observed >80% reduction in mRNA expression regardless of the site amplified. These observations were perplexing, especially considering that whole genome sequencing of BAd-CRISPR Ucp1 mice revealed that only 36.1% of all genomic sequences had mutations at the sgRNA cut site. To explain this phenomenon, we postulate the following: i.) high incidence of nonsense mutations and rapid degradation of mRNA, ii.) large scale deletions of genomic DNA, or iii.) blocking of transcription. It is possible that one or a combination of these contribute to an inability to detect mRNA and thus warrant future study.

Double-stranded breaks repaired by NHEJ result in indels of unpredictable length that can alter the coding frame and result in nonsense mutations which lead to truncated proteins (45,46). Typically, the cell employs nonsense-mediated decay to degrade mutant mRNA or nonsense-associated alternative splicing to remove the premature termination codon from the transcript (47,48). Given that all sgRNAs used in this study target the early coding region of each gene (exon 2 or exon 3) and given that frameshift mutations

predominated the observed mutation pool, it is therefore possible that BAd-CRISPR caused premature termination codons in the early coding region which led to nonsense-mediated decay of mutant mRNA and thus prevented our ability to probe for gene expression using qPCR. It is also possible that a proportion of these frameshift mutations were repaired via nonsense-associated alternative splicing, as CRISPR/Cas9 genome editing has been shown to induce exon skipping (49). These mutations may also affect codon optimality, which has been shown to impact transcript stability (50,51). This might explain why we do not detect protein expression for each target gene, as unstable mRNA transcripts are rapidly degraded before being translated. Thus, nonsense mutations and rapid mRNA degradation may partially account for our inability to detect mRNA.

A second explanation could be large scale deletions in genomic DNA. Several studies have reported on the rare incidence of indels spanning several hundred base pairs following CRISPR/Cas9 mutagenesis (52,53). Others have reported on the generation of inversions, endogenous and exogenous DNA insertions, and large deletions (54-56). Recently, Kosicki et al. showed that DNA breaks introduced by a sgRNA frequently resulted in deletions spanning many kilobases and argued that most studies miss these large scale deletions because they fail to amplify regions > 1 kilobase pairs around the target site (57). In another study, Cullot and colleagues demonstrated the rare incidence of megabase-scale chromosomal translocations from one double-strand break (58). Indeed, we did not directly assess for the presence of large-scale deletions as sequencing amplicons were typically <500 base pairs in length. Although we performed whole genome sequencing on BAd-CRISPR Ucp1 mice, detection of large indels is challenging because of the short read lengths (~150 base pairs) generated by paired-end sequencing (59). Moreover, paired-end read mapping is insensitive to both small and large indel events because of the difficulty in separating small perturbations in read-pair distance from the normal background variability (59). Therefore, we cannot rule out the possibility of large-scale deletions in genomic DNA that arise from the BAd-CRISPR method. Future work should employ single molecule, real-time sequencing to enable accurate long sequence reads.

Lastly, a possible–albeit unlikely– explanation for an inability to detect mRNA is that the ribonucleoprotein complex binds to the genomic target, blocks the activity of RNA

polymerase II, and prevents transcription. Recently, Clarke et al. demonstrated that Cas9 remains stably bound to DNA even after forming a double-stranded break and blocks access of NHEJ repair machinery, thereby reducing genome editing efficiency (60). Cas9 can be dislodged by RNA polymerase II but only if it is annealed to the template DNA strand used by RNA polymerase II (60). Interestingly, the sgRNAs designed in this study bind to the non-template DNA strand. Thus, there is a possibility that Cas9 becomes bound and prevents the accumulation of indels, which may explain why we do not see more pronounced mutations in whole genome sequencing data of BAd-CRISPR Ucp1 mice. While this phenomenon has not been reported *in vivo* and persistence of Cas9 binding to template DNA in mammalian cells is debated, it is prudent to consider allele suppression as a potential mechanism by which BAd-CRISPR functions (61).

Can BAd-CRISPR be used for more advanced CRISPR applications, such as base editing, CRISPRa, or CRISPRi?

CRISPR affords the ability to do much more than cause indels and ablate gene expression. In fact, modifications to the CRISPR system have opened a wide array of tools for precision editing of the genome that can correct point mutations or overexpress/repress gene expression. It is our goal to implement these CRISPR systems to the BAd-CRISPR method to create a more robust technology with broad applications in adipose tissue research.

To correct point mutations, programmable base editors have been developed using catalytically inactive Cas9 (dCas9) or Cas9 nickase fused to diverse functional domains (40). Unlike the traditional CRISPR/Cas9 system, base editors allow for site-specific DNA base modification without generating double-strand breaks (62). Currently, there are two types of base editors: cytosine deaminase and adenine deaminase DNA base editors (63-66). As the name implies, cytosine deaminases catalyze the conversion of cytosine to thymine. First, dCas9 deaminates cytosine to uracil which results in a U-G mismatch that is then resolved by repair mechanisms to form a U-A base pair followed by a T-A base pair (62-64). This ultimately results in a C→T point mutation (62). By contrast, adenine deaminase base editors deaminate adenosine to yield inosine, which base pairs with cytosine and is corrected to guanine, to convert A→G or A-T into G-C (62,65,66).

Collectively, cytosine and adenine deaminase base editors enable C→T, T→C, A→G, and G→A transition mutations (67). Recently, prime-editing, a process by which reverse transcriptase is fused to Cas9 nickase, can generate any base transition (68). These technologies thus open the possibility of more precisely modeling disease *in vivo*. For example, several studies have applied AAVs to administer base editors to correct point mutations in Duchene muscular dystrophy and phenylketonuria and have also been optimized to achieve base editing in brain, liver, retina, heart, and skeletal muscles (67,69-71). Base editors are thus well suited for application in adipose tissue, as they can be packaged into AAVs and used to more closely model disease. Additionally, base editors have high efficiency and are better suited for adipocytes than homology directed repair (HDR), which is limited to the S/G2 phase of the cell cycle and therefore applicable to highly proliferating cell types only (40,72). Thus, mining genome-wide association studies from obese patients can identify single nucleotide polymorphisms which can then be modeled in mice by using base editors (73).

Beyond permanently altering the genome through indels or base editing, CRISPR can also be used to manipulate gene expression without modifying the genetic code. In fact, dCas9 has been exploited to both overexpress or repress gene expression by fusing it to specific motifs (74). For overexpression, dCas9 has been fused to strong transcriptional activators such as VP64, VPR, SAM, or SunTag to induce gene expression, a process termed CRISPR activation (CRISPRa) (75-77). CRISPRa has recently been used to overexpress genes in preadipocytes and adipocytes *in vitro* (11,15). Lundh et al. stably expressed dCas9-VP64 in cultured preadipocytes and demonstrated significant upregulation of peroxisome proliferator-activated receptor-γ2 that promoted adipogenesis (11). Additionally, CRISPRa was used to upregulate *Ucp1* expression in mature adipocytes in culture to mimic beiging. Wang et al. also applied CRISPRa to engineer human brown-like cells from white preadipocytes by upregulating *Ucp1* expression (15). Impressively, transplantation of CRISPRa-engineered human brown-like cells to obese mice improved glucose homeostasis and increased activation of endogenous BAT. While CRISPRa has nonetheless proved useful in cultured adipocytes, it has not been delivered to adipose tissues *in vivo*. Thus, future work incorporating CRISPRa to AAV8 can enable its use in a modified BAd-CRISPR method.

dCas9 can also be used to repress gene expression by binding to the DNA target sequence and preventing the activity of RNA polymerase II (74). To enhance repression, dCas9 has been fused to the Krüppel-associated Box protein and is referred to as CRISPR interference (CRISPRi) (78). Currently, CRISPRi gene repression in adipose tissue has only been reported by one study (79). Chung et al. utilized an oligopeptide complex to administer CRISPRi to repress *Fabp4* expression and ameliorate obesity in mice. Surprisingly, knockdown of *Fabp4* in the eWAT led to a 20% decrease in body weight, reduction in inflammation, reversal of hepatic steatosis, and improved insulin sensitivity in obese mice. As highlighted in Chapter I, these data should be interpreted with caution, as the authors fail to adequately explain the mechanism by which the oligopeptide complex is taken up by adipocytes and how suppression of *Fabp4* in one adipose tissue contributes to such a marked change in whole body metabolism (17).

Concluding remarks

My doctoral work has demonstrated for the first time that the powerful gene editing tool CRISPR/Cas9 can be adapted to function in BAT of adult mice. The BAd-CRISPR method integrates well-established AAV gene transfer and Cre-Lox mouse models to facilitate targeted inducible gene knockout in BAT. Importantly, BAd-CRISPR is scalable, can be adapted to target virtually any gene, and does not lead to substantial off-target mutations. Indeed, continued research is still required to optimize delivery vectors and routes of administration for CRISPR/Cas9 inducible knockout in white or marrow adipose tissues and particular focus should be paid to how BAd-CRISPR suppresses mRNA expression. Ultimately, I hope this method advances the field of adipose tissue research and inspires the use of CRISPR/Cas9 inducible gene knockout in other tissues.

REFERENCES

1. Platt, R. J., Chen, S., Zhou, Y., Yim, M. J., Swiech, L., Kempton, H. R., Dahlman, J. E., Parnas, O., Eisenhaure, T. M., Jovanovic, M., Graham, D. B., Jhunjhunwala, S., Heidenreich, M., Xavier, R. J., Langer, R., Anderson, D. G., Hacohen, N., Regev, A., Feng, G., Sharp, P. A., and Zhang, F. (2014) CRISPR-Cas9 knockin mice for genome editing and cancer modeling. *Cell* **159**, 440-455
2. Sanchez-Rivera, F. J., Papagiannakopoulos, T., Romero, R., Tammela, T., Bauer, M. R., Bhutkar, A., Joshi, N. S., Subbaraj, L., Bronson, R. T., Xue, W., and Jacks, T. (2014) Rapid modelling of cooperating genetic events in cancer through somatic genome editing. *Nature* **516**, 428-431
3. Cheng, R., Peng, J., Yan, Y., Cao, P., Wang, J., Qiu, C., Tang, L., Liu, D., Tang, L., Jin, J., Huang, X., He, F., and Zhang, P. (2014) Efficient gene editing in adult mouse livers via adenoviral delivery of CRISPR/Cas9. *FEBS Lett* **588**, 3954-3958
4. Dow, L. E. (2015) Modeling Disease In Vivo With CRISPR/Cas9. *Trends Mol Med* **21**, 609-621
5. Dow, L. E., Fisher, J., O'Rourke, K. P., Muley, A., Kastenhuber, E. R., Livshits, G., Tschaharganeh, D. F., Socci, N. D., and Lowe, S. W. (2015) Inducible in vivo genome editing with CRISPR-Cas9. *Nat Biotechnol* **33**, 390-394
6. Swiech, L., Heidenreich, M., Banerjee, A., Habib, N., Li, Y., Trombetta, J., Sur, M., and Zhang, F. (2015) In vivo interrogation of gene function in the mammalian brain using CRISPR-Cas9. *Nat Biotechnol* **33**, 102-106
7. Zafra, M. P., and Dow, L. E. (2016) Somatic Genome Editing Goes Viral. *Trends Mol Med* **22**, 831-833
8. Yin, H., Song, C. Q., Dorkin, J. R., Zhu, L. J., Li, Y., Wu, Q., Park, A., Yang, J., Suresh, S., Bizhanova, A., Gupta, A., Bolukbasi, M. F., Walsh, S., Bogorad, R. L., Gao, G., Weng, Z., Dong, Y., Koteliansky, V., Wolfe, S. A., Langer, R., Xue, W., and Anderson, D. G. (2016) Therapeutic genome editing by combined viral and non-viral delivery of CRISPR system components in vivo. *Nat Biotechnol* **34**, 328-333
9. VanDusen, N. J., Guo, Y., Gu, W., and Pu, W. T. (2017) CASAAV: A CRISPR-Based Platform for Rapid Dissection of Gene Function In Vivo. *Curr Protoc Mol Biol* **120**, 31.11.31-31.11.14
10. Guo, Y., VanDusen, N. J., Zhang, L., Gu, W., Sethi, I., Guatimosim, S., Ma, Q., Jardin, B. D., Ai, Y., Zhang, D., Chen, B., Guo, A., Yuan, G. C., Song, L. S., and Pu, W. T. (2017) Analysis of Cardiac Myocyte Maturation Using CASAAV, a Platform for Rapid Dissection of Cardiac Myocyte Gene Function In Vivo. *Circ Res* **120**, 1874-1888
11. Lundh, M., Pluciñska, K., Isidor, M. S., Petersen, P. S. S., and Emanuelli, B. (2017) Bidirectional manipulation of gene expression in adipocytes using CRISPRa and siRNA. *Mol Metab* **6**, 1313-1320
12. Shen, Y., Cohen, J. L., Nicoloro, S. M., Kelly, M., Yenilmez, B., Henriques, F., Tsagkaraki, E., Edwards, Y. J. K., Hu, X., Friedline, R. H., Kim, J. K., and Czech, M. P. (2018) CRISPR-delivery particles targeting nuclear receptor-interacting protein 1 (Nrip1) in adipose cells to enhance energy expenditure. *J Biol Chem* **293**, 17291-17305

13. Chung, J. Y., Ain, Q. U., Song, Y., Yong, S. B., and Kim, Y. H. (2019) Targeted delivery of CRISPR interference system against Fabp4 to white adipocytes ameliorates obesity, inflammation, hepatic steatosis, and insulin resistance. *Genome Res* **29**, 1442-1452
14. Kamble, P. G., Hetty, S., Vranic, M., Almby, K., Castillejo-Lopez, C., Abalo, X. M., Pereira, M. J., and Eriksson, J. W. (2020) Proof-of-concept for CRISPR/Cas9 gene editing in human preadipocytes: Deletion of FKBP5 and PPARG and effects on adipocyte differentiation and metabolism. *Sci Rep* **10**, 10565
15. Wang, C. H., Lundh, M., Fu, A., Kriszt, R., Huang, T. L., Lynes, M. D., Leiria, L. O., Shamsi, F., Darcy, J., Greenwood, B. P., Narain, N. R., Tolstikov, V., Smith, K. L., Emanuelli, B., Chang, Y. T., Hagen, S., Danial, N. N., Kiebish, M. A., and Tseng, Y. H. (2020) CRISPR-engineered human brown-like adipocytes prevent diet-induced obesity and ameliorate metabolic syndrome in mice. *Sci Transl Med* **12**
16. Gomez-Banoy, N., and Lo, J. C. (2017) Genetic Manipulation with Viral Vectors to Assess Metabolism and Adipose Tissue Function. *Methods Mol Biol* **1566**, 109-124
17. Romanelli, S. M., and MacDougald, O. A. (2020) Viral and Nonviral Transfer of Genetic Materials to Adipose Tissues: Toward a Gold Standard Approach. *Diabetes* **69**, 2581-2588
18. Bates, R., Huang, W., and Cao, L. (2020) Adipose Tissue: An Emerging Target for Adeno-associated Viral Vectors. *Mol Ther Methods Clin Dev* **19**, 236-249
19. Maurer, S. F., Fromme, T., Mocek, S., Zimmermann, A., and Klingenspor, M. (2020) Uncoupling protein 1 and the capacity for nonshivering thermogenesis are components of the glucose homeostatic system. *Am J Physiol Endocrinol Metab* **318**, E198-E215
20. Lodhi, I. J., and Semenkovich, C. F. (2014) Peroxisomes: a nexus for lipid metabolism and cellular signaling. *Cell Metab* **19**, 380-392
21. Singh, I., Moser, A. E., Goldfischer, S., and Moser, H. W. (1984) Lignoceric acid is oxidized in the peroxisome: implications for the Zellweger cerebro-hepato-renal syndrome and adrenoleukodystrophy. *Proc Natl Acad Sci U S A* **81**, 4203-4207
22. Schrader, M., and Fahimi, H. D. (2006) Peroxisomes and oxidative stress. *Biochim Biophys Acta* **1763**, 1755-1766
23. Livneh, I., Cohen-Kaplan, V., Cohen-Rosenzweig, C., Avni, N., and Ciechanover, A. (2016) The life cycle of the 26S proteasome: from birth, through regulation and function, and onto its death. *Cell Res* **26**, 869-885
24. Bartelt, A., Widenmaier, S. B., Schlein, C., Johann, K., Goncalves, R. L. S., Eguchi, K., Fischer, A. W., Parlakgul, G., Snyder, N. A., Nguyen, T. B., Bruns, O. T., Franke, D., Bawendi, M. G., Lynes, M. D., Leiria, L. O., Tseng, Y. H., Inouye, K. E., Arruda, A. P., and Hotamisligil, G. S. (2018) Brown adipose tissue thermogenic adaptation requires Nrf1-mediated proteasomal activity. *Nat Med* **24**, 292-303
25. Divakaruni, A. S., Rogers, G. W., and Murphy, A. N. (2014) Measuring Mitochondrial Function in Permeabilized Cells Using the Seahorse XF Analyzer or a Clark-Type Oxygen Electrode. *Curr Protoc Toxicol* **60**, 25.22.21-16

26. Jimenez, V., Munoz, S., Casana, E., Mallol, C., Elias, I., Jambrina, C., Ribera, A., Ferre, T., Franckhauser, S., and Bosch, F. (2013) In vivo adeno-associated viral vector-mediated genetic engineering of white and brown adipose tissue in adult mice. *Diabetes* **62**, 4012-4022
27. Büning, H., Huber, A., Zhang, L., Meumann, N., and Hacker, U. (2015) Engineering the AAV capsid to optimize vector-host-interactions. *Curr Opin Pharmacol* **24**, 94-104
28. Büning, H., and Srivastava, A. (2019) Capsid Modifications for Targeting and Improving the Efficacy of AAV Vectors. *Mol Ther Methods Clin Dev* **12**, 248-265
29. Ogden, P. J., Kelsic, E. D., Sinai, S., and Church, G. M. (2019) Comprehensive AAV capsid fitness landscape reveals a viral gene and enables machine-guided design. *Science* **366**, 1139-1143
30. Davidsson, M., Wang, G., Aldrin-Kirk, P., Cardoso, T., Nolbrant, S., Hartnor, M., Mudannayake, J., Parmar, M., and Björklund, T. (2019) A systematic capsid evolution approach performed in vivo for the design of AAV vectors with tailored properties and tropism. *Proc Natl Acad Sci U S A*
31. Charbel Issa, P., De Silva, S. R., Lipinski, D. M., Singh, M. S., Mouravlev, A., You, Q., Barnard, A. R., Hankins, M. W., During, M. J., and Maclaren, R. E. (2013) Assessment of tropism and effectiveness of new primate-derived hybrid recombinant AAV serotypes in the mouse and primate retina. *PLoS One* **8**, e60361
32. Liu, X., Magee, D., Wang, C., McMurphy, T., Slater, A., During, M., and Cao, L. (2014) Adipose tissue insulin receptor knockdown via a new primate-derived hybrid recombinant AAV serotype. *Mol Ther Methods Clin Dev* **1**
33. Huang, W., McMurphy, T., Liu, X., Wang, C., and Cao, L. (2016) Genetic Manipulation of Brown Fat Via Oral Administration of an Engineered Recombinant Adeno-associated Viral Serotype Vector. *Mol Ther* **24**, 1062-1069
34. Huang, W., Liu, X., Queen, N. J., and Cao, L. (2017) Targeting Visceral Fat by Intraperitoneal Delivery of Novel AAV Serotype Vector Restricting Off-Target Transduction in Liver. *Mol Ther Methods Clin Dev* **6**, 68-78
35. Huang, W., Queen, N. J., and Cao, L. (2019) rAAV-Mediated Gene Delivery to Adipose Tissue. *Methods Mol Biol* **1950**, 389-405
36. Mizukami, H., Mimuro, J., Ogura, T., Okada, T., Urabe, M., Kume, A., Sakata, Y., and Ozawa, K. (2006) Adipose tissue as a novel target for in vivo gene transfer by adeno-associated viral vectors. *Hum Gene Ther* **17**, 921-928
37. Kabanov, A., Zhu, J., and Alakhov, V. (2005) Pluronic block copolymers for gene delivery. *Adv Genet* **53**, 231-261
38. Anzalone, A. V., Koblan, L. W., and Liu, D. R. (2020) Genome editing with CRISPR-Cas nucleases, base editors, transposases and prime editors. *Nat Biotechnol* **38**, 824-844
39. Hille, F., Richter, H., Wong, S. P., Bratovic, M., Ressel, S., and Charpentier, E. (2018) The Biology of CRISPR-Cas: Backward and Forward. *Cell* **172**, 1239-1259
40. Moon, S. B., Kim, D. Y., Ko, J. H., and Kim, Y. S. (2019) Recent advances in the CRISPR genome editing tool set. *Exp Mol Med* **51**, 1-11

41. Jiang, F., and Doudna, J. A. (2017) CRISPR-Cas9 Structures and Mechanisms. *Annu Rev Biophys* **46**, 505-529
42. Sternberg, S. H., Redding, S., Jinek, M., Greene, E. C., and Doudna, J. A. (2014) DNA interrogation by the CRISPR RNA-guided endonuclease Cas9. *Nature* **507**, 62-67
43. Jiang, F., Taylor, D. W., Chen, J. S., Kornfeld, J. E., Zhou, K., Thompson, A. J., Nogales, E., and Doudna, J. A. (2016) Structures of a CRISPR-Cas9 R-loop complex primed for DNA cleavage. *Science* **351**, 867-871
44. Jinek, M., Chylinski, K., Fonfara, I., Hauer, M., Doudna, J. A., and Charpentier, E. (2012) A programmable dual-RNA-guided DNA endonuclease in adaptive bacterial immunity. *Science* **337**, 816-821
45. Tuladhar, R., Yeu, Y., Tyler Piazza, J., Tan, Z., Rene Clemenceau, J., Wu, X., Barrett, Q., Herbert, J., Mathews, D. H., Kim, J., Hyun Hwang, T., and Lum, L. (2019) CRISPR-Cas9-based mutagenesis frequently provokes on-target mRNA misregulation. *Nat Commun* **10**, 4056
46. Sui, T., Song, Y., Liu, Z., Chen, M., Deng, J., Xu, Y., Lai, L., and Li, Z. (2018) CRISPR-induced exon skipping is dependent on premature termination codon mutations. *Genome Biol* **19**, 164
47. Hentze, M. W., and Kulozik, A. E. (1999) A perfect message: RNA surveillance and nonsense-mediated decay. *Cell* **96**, 307-310
48. Liu, H. X., Cartegni, L., Zhang, M. Q., and Krainer, A. R. (2001) A mechanism for exon skipping caused by nonsense or missense mutations in BRCA1 and other genes. *Nat Genet* **27**, 55-58
49. Mou, H., Smith, J. L., Peng, L., Yin, H., Moore, J., Zhang, X. O., Song, C. Q., Sheel, A., Wu, Q., Ozata, D. M., Li, Y., Anderson, D. G., Emerson, C. P., Sontheimer, E. J., Moore, M. J., Weng, Z., and Xue, W. (2017) CRISPR/Cas9-mediated genome editing induces exon skipping by alternative splicing or exon deletion. *Genome Biol* **18**, 108
50. Medina-Muñoz, S. G., Kushawah, G., Castellano, L. A., Diez, M., DeVore, M. L., Salazar, M. J. B., and Bazzini, A. A. (2021) Crosstalk between codon optimality and cis-regulatory elements dictates mRNA stability. *Genome Biol* **22**, 14
51. Forrest, M. E., Pinkard, O., Martin, S., Sweet, T. J., Hanson, G., and Coller, J. (2020) Codon and amino acid content are associated with mRNA stability in mammalian cells. *PLoS One* **15**, e0228730
52. Ghezraoui, H., Piganeau, M., Renouf, B., Renaud, J. B., Sallmyr, A., Ruis, B., Oh, S., Tomkinson, A. E., Hendrickson, E. A., Giovannangeli, C., Jasin, M., and Brunet, E. (2014) Chromosomal translocations in human cells are generated by canonical nonhomologous end-joining. *Mol Cell* **55**, 829-842
53. Hendel, A., Bak, R. O., Clark, J. T., Kennedy, A. B., Ryan, D. E., Roy, S., Steinfeld, I., Lunstad, B. D., Kaiser, R. J., Wilkens, A. B., Bacchetta, R., Tsalenko, A., Dellinger, D., Bruhn, L., and Porteus, M. H. (2015) Chemically modified guide RNAs enhance CRISPR-Cas genome editing in human primary cells. *Nat Biotechnol* **33**, 985-989
54. Boroviak, K., Doe, B., Banerjee, R., Yang, F., and Bradley, A. (2016) Chromosome engineering in zygotes with CRISPR/Cas9. *Genesis* **54**, 78-85

55. Canver, M. C., Bauer, D. E., Dass, A., Yien, Y. Y., Chung, J., Masuda, T., Maeda, T., Paw, B. H., and Orkin, S. H. (2017) Characterization of genomic deletion efficiency mediated by clustered regularly interspaced short palindromic repeats (CRISPR)/Cas9 nuclease system in mammalian cells. *J Biol Chem* **292**, 2556
56. Kraft, K., Geuer, S., Will, A. J., Chan, W. L., Paliou, C., Borschiwer, M., Harabula, I., Wittler, L., Franke, M., Ibrahim, D. M., Kragesteen, B. K., Spielmann, M., Mundlos, S., Lupianez, D. G., and Andrey, G. (2015) Deletions, Inversions, Duplications: Engineering of Structural Variants using CRISPR/Cas in Mice. *Cell Rep* **10**, 833-839
57. Kosicki, M., Tomberg, K., and Bradley, A. (2018) Repair of double-strand breaks induced by CRISPR-Cas9 leads to large deletions and complex rearrangements. *Nat Biotechnol* **36**, 765-771
58. Cullot, G., Boutin, J., Toutain, J., Prat, F., Pennamen, P., Rooryck, C., Teichmann, M., Rousseau, E., Lamrissi-Garcia, I., Guyonnet-Duperat, V., Bibeyran, A., Lalanne, M., Prouzet-Mauleon, V., Turcq, B., Ged, C., Blouin, J. M., Richard, E., Dabernat, S., Moreau-Gaudry, F., and Bedel, A. (2019) CRISPR-Cas9 genome editing induces megabase-scale chromosomal truncations. *Nat Commun* **10**, 1136
59. Abel, H. J., and Duncavage, E. J. (2013) Detection of structural DNA variation from next generation sequencing data: a review of informatic approaches. *Cancer Genet* **206**, 432-440
60. Clarke, R., Heler, R., MacDougall, M. S., Yeo, N. C., Chavez, A., Regan, M., Hanakahi, L., Church, G. M., Marraffini, L. A., and Merrill, B. J. (2018) Enhanced Bacterial Immunity and Mammalian Genome Editing via RNA-Polymerase-Mediated Dislodging of Cas9 from Double-Strand DNA Breaks. *Mol Cell* **71**, 42-55.e48
61. Knight, S. C., Xie, L., Deng, W., Guglielmi, B., Witkowsky, L. B., Bosanac, L., Zhang, E. T., El Beheiry, M., Masson, J. B., Dahan, M., Liu, Z., Doudna, J. A., and Tjian, R. (2015) Dynamics of CRISPR-Cas9 genome interrogation in living cells. *Science* **350**, 823-826
62. Eid, A., Alshareef, S., and Mahfouz, M. M. (2018) CRISPR base editors: genome editing without double-stranded breaks. *Biochem J* **475**, 1955-1964
63. Komor, A. C., Kim, Y. B., Packer, M. S., Zuris, J. A., and Liu, D. R. (2016) Programmable editing of a target base in genomic DNA without double-stranded DNA cleavage. *Nature* **533**, 420-424
64. Shimatani, Z., Kashojiya, S., Takayama, M., Terada, R., Arazoe, T., Ishii, H., Teramura, H., Yamamoto, T., Komatsu, H., Miura, K., Ezura, H., Nishida, K., Ariizumi, T., and Kondo, A. (2017) Targeted base editing in rice and tomato using a CRISPR-Cas9 cytidine deaminase fusion. *Nat Biotechnol* **35**, 441-443
65. Gaudelli, N. M., Komor, A. C., Rees, H. A., Packer, M. S., Badran, A. H., Bryson, D. I., and Liu, D. R. (2017) Programmable base editing of A•T to G•C in genomic DNA without DNA cleavage. *Nature* **551**, 464-471
66. Komor, A. C., Badran, A. H., and Liu, D. R. (2018) Editing the Genome Without Double-Stranded DNA Breaks. *ACS Chem Biol* **13**, 383-388

67. Kantor, A., McClements, M. E., and MacLaren, R. E. (2020) CRISPR-Cas9 DNA Base-Editing and Prime-Editing. *Int J Mol Sci* **21**
68. Anzalone, A. V., Randolph, P. B., Davis, J. R., Sousa, A. A., Koblan, L. W., Levy, J. M., Chen, P. J., Wilson, C., Newby, G. A., Raguram, A., and Liu, D. R. (2019) Search-and-replace genome editing without double-strand breaks or donor DNA. *Nature* **576**, 149-157
69. Ryu, S. M., Koo, T., Kim, K., Lim, K., Baek, G., Kim, S. T., Kim, H. S., Kim, D. E., Lee, H., Chung, E., and Kim, J. S. (2018) Adenine base editing in mouse embryos and an adult mouse model of Duchenne muscular dystrophy. *Nat Biotechnol* **36**, 536-539
70. Villiger, L., Grisch-Chan, H. M., Lindsay, H., Ringnalda, F., Pogliano, C. B., Allegri, G., Fingerhut, R., Häberle, J., Matos, J., Robinson, M. D., Thöny, B., and Schwank, G. (2018) Treatment of a metabolic liver disease by in vivo genome base editing in adult mice. *Nat Med* **24**, 1519-1525
71. Levy, J. M., Yeh, W. H., Pendse, N., Davis, J. R., Hennessey, E., Butcher, R., Koblan, L. W., Comander, J., Liu, Q., and Liu, D. R. (2020) Cytosine and adenine base editing of the brain, liver, retina, heart and skeletal muscle of mice via adeno-associated viruses. *Nat Biomed Eng* **4**, 97-110
72. Musunuru, K. (2017) The Hope and Hype of CRISPR-Cas9 Genome Editing: A Review. *JAMA Cardiol* **2**, 914-919
73. Goodarzi, M. O. (2018) Genetics of obesity: what genetic association studies have taught us about the biology of obesity and its complications. *Lancet Diabetes Endocrinol* **6**, 223-236
74. Adli, M. (2018) The CRISPR tool kit for genome editing and beyond. *Nat Commun* **9**, 1911
75. Maeder, M. L., Linder, S. J., Cascio, V. M., Fu, Y., Ho, Q. H., and Joung, J. K. (2013) CRISPR RNA-guided activation of endogenous human genes. *Nat Methods* **10**, 977-979
76. Perez-Pinera, P., Kocak, D. D., Vockley, C. M., Adler, A. F., Kabadi, A. M., Polstein, L. R., Thakore, P. I., Glass, K. A., Ousterout, D. G., Leong, K. W., Guilak, F., Crawford, G. E., Reddy, T. E., and Gersbach, C. A. (2013) RNA-guided gene activation by CRISPR-Cas9-based transcription factors. *Nat Methods* **10**, 973-976
77. Chavez, A., Tuttle, M., Pruitt, B. W., Ewen-Campen, B., Chari, R., Ter-Ovanesyan, D., Haque, S. J., Cecchi, R. J., Kowal, E. J. K., Buchthal, J., Housden, B. E., Perrimon, N., Collins, J. J., and Church, G. (2016) Comparison of Cas9 activators in multiple species. *Nat Methods* **13**, 563-567
78. Gilbert, L. A., Larson, M. H., Morsut, L., Liu, Z., Brar, G. A., Torres, S. E., Stern-Ginossar, N., Brandman, O., Whitehead, E. H., Doudna, J. A., Lim, W. A., Weissman, J. S., and Qi, L. S. (2013) CRISPR-mediated modular RNA-guided regulation of transcription in eukaryotes. *Cell* **154**, 442-451
79. Chung, J. Y., Ain, Q. U., Song, Y., Yong, S. B., and Kim, Y. H. (2019) Targeted delivery of CRISPR interference system against. *Genome Res* **29**, 1442-1452